

**Theory of Adsorption, Diffusion,
and Growth
of Cobalt on Cu(001)**

Im Fachbereich Physik
der Freien Universität Berlin
eingereichte Dissertation

von
Rossitza Pentcheva

Mai 2000

dissertation.de

Verlag im Internet

Sonderausgabe des Werkes mit der ISBN-Nummer: 3-89825-184-5

Die vorliegende Arbeit wurde in der Zeit von Januar 1997 bis Mai 2000 am Fritz-Haber-Institut der Max-Planck Gesellschaft unter der Leitung von Prof. Dr. Matthias Scheffler angefertigt.

1. Gutachter:

Prof. Dr. K.-H. Bennemann

2. Gutachter:

Prof. Dr. M. Scheffler

Tag der mündlichen Prüfung:

11.07.2000

dissertation.de

Verlag im Internet

Fritschestr. 68

10 585 Berlin

E-Mail:

dissertation.de@snafu.de

URL:

<http://www.dissertation.de>

Contents

1	Introduction	5
1.1	Models for the description of growth	6
1.2	Goal and outline of the thesis	9
2	Theoretical foundations of the FP-LAPW method	13
2.1	Density-Functional Theory	14
2.2	The FP-LAPW method	16
2.2.1	Basis functions: APW and LAPW method	17
2.2.2	Representation of the potential: FP-LAPW	18
2.2.3	Description of surfaces: The super-cell approach	19
2.2.4	The WIEN97 code	20
3	Stable and metastable structures of Cobalt on Cu(001)	25
3.1	Introduction	25
3.2	Computational details	27
3.3	Formation energy and stability	30
3.4	Structural properties	35
3.5	Magnetic properties	38
3.6	Electronic properties	40
3.7	Comparison of Co/Cu(001) and Co/Cu(111)	41
3.8	Summary	43
3.9	Appendix	44
4	Initial Adsorption of Cobalt on Cu(001)	47
4.1	Introduction	47
4.2	Computational details	48
4.3	On-surface versus substitutional site	50
4.4	Dependence of E^{ad} on coverage	55
4.5	Influence of magnetism on the adsorption energy	58
4.6	Nucleation potential of substituted Co atoms	62

4.7	Summary	69
4.8	Appendix	69
5	Adatom diffusion on the flat Cu(001)-surface	71
5.1	Introduction	71
5.2	Numerical details	73
5.3	Selfdiffusion on the Cu(001)-surface	73
5.3.1	Diffusion barriers	73
5.3.2	Structure and bond lengths in the transition state	76
5.4	Co adatom diffusion on the Cu(001)-surface	80
5.4.1	Diffusion barriers	81
5.4.2	Structural and electronic effects	81
5.5	Comparison of Co and Cu adatom diffusion	86
5.6	Influence of magnetism on the barrier height of Co	87
6	Stepped surfaces: formation energies, adsorption and diffusion at steps	89
6.1	Introduction	89
6.2	Formation energy of the close packed step	91
6.3	Adsorption of Co and Cu adatoms at steps	93
6.3.1	Adsorption energies	93
6.3.2	Structural properties	95
6.4	Diffusion of Co and Cu adatoms along steps	97
6.4.1	Diffusion barriers	97
6.4.2	Structural properties	99
6.5	Onset temperature for diffusion	100
7	Kinetic Monte Carlo simulations of growth	103
7.1	General remarks on growth simulations	103
7.1.1	Comparison between MD, rate equations, and MC	103
7.1.2	Geometric and dynamic assumptions of the MC method	105
7.1.3	Thermodynamic versus kinetic Monte Carlo	106
7.1.4	Implementation - the N -fold method	107
7.2	Homoepitaxy: Cu on Cu(001)	109
7.2.1	Island morphology	109
7.2.2	Adatom and island density, scaling properties	110
7.2.3	Other models for adatom-adatom interaction	112
7.3	Heteroepitaxy: Co on Cu(001)	114
7.3.1	Island morphologies in the homo- and heteroepitaxial case	116
7.3.2	Island Densities in the homo- and heteroepitaxial case	119

7.4 Summary 120

8 Summary and Outlook **123**

Chapter 1

Introduction

Growth of thin magnetic films on a nonmagnetic substrate provides the possibility to design materials that do not exist in the bulk phase and exhibit novel physical properties. For example Co, which crystallizes at room temperature in the hcp phase, grows pseudomorphic on Cu(001) up to 20 monolayers in a fcc structure [1]. Multilayers of Co separated by Cu can couple either ferro- or antiferromagnetically and this behavior oscillates with the thickness of the nonmagnetic spacer, a phenomenon that is referred to as *interlayer exchange coupling* (IEC) [2–4]. Almost simultaneously it was found that the resistance of a probe where the ferromagnetic layers are coupled parallel is lower than when they couple antiparallel independent of the orientation of the current. This effect was called *giant magnetoresistance* (GMR) [5, 6]. “Giant” refers to the size of the change in magnetoresistance which can reach up to 65% for Co/Cu or Fe/Cr multilayers.

The discovery of magnetic phenomena like GMR and IEC in layered materials initiated rigorous activities both in research and industry. Currently, main application areas are magnetic sensors and magnetic storage of data. Read heads based on GMR made it possible to increase areal densities of magnetic hard disk drives to several Gbits/in² nowadays and this trend continues with an annual growth of areal density of 60% [7]. The second application based on GMR, magnetic RAM (random access memory), has a clear advantage compared to traditional semiconductor memory: it is nonvolatile, *i.e.* information is not lost after power is turned off from the computer. First GMR-based RAMs were presented by the Honeywell Corporation already in 1997 [8]. Promising to revolutionize memory technology in the near future is the magnetoresistive RAM test chip recently presented by Motorola Inc. [9] which is characterized by a fast read and write speed and competitive low cost. A new kind of electronics, *magnetoelectronics* or *spintronics*, based on the ability to detect and control the spins of electrons

in magnetic materials, is currently being developed [10].

The materials used for these applications consist of ferromagnetic layers with a thickness of several nanometers separated by a nonmagnetic spacer. A typical example are multilayers of Co and Cu. The magnetic behavior of such nanostructures depends sensitively on the surface and interface morphology. Thus, in order to design materials with particular magnetic properties it is crucial to understand and control growth on an atomic scale. Despite the enormous progress in fabrication and characterization of structures on the nanometer scale [11] a fundamental understanding of heteroepitaxial growth is not achieved yet.

The initial growth of Co on Cu(001) has been subject of controversial debate in the literature and some surprising findings still lack explanation. Experimental results report substantial deviations from the layer-by-layer growth mode for the first two monolayers: second layer islands start to nucleate before the first layer is completed [12, 13]. The amount of material in the second layer depends strongly on growth conditions [13, 14]. After annealing substrate material segregates on the surface [12, 15]. For monolayer coverages STM and RHEED studies [14, 16] found regions on the surface where an ordered $c(2 \times 2)$ -surface alloy was formed.

Typically, for technological applications a sharp interface between deposit and substrate is desirable. However, experimental results indicate surface intermixing for submonolayer coverages deposited on Cu(001) [13, 14, 16, 17]. Moreover, island densities and island size distributions vary substantially from the ones known from the homoepitaxial case [17], implying that intermixing should have significant consequences for island nucleation and surface morphology.

1.1 Models for the description of growth

The first concepts to describe growth were based on thermodynamic considerations [18]: In thermal equilibrium structures are determined by the minimum of the free energy. Depending on the balance between the surface energies of the substrate material, $\gamma_{\text{substrate}}$, the overlayer, $\gamma_{\text{overlayer}}$, and the interface energy, $\gamma_{\text{interface}}$, three different growth modes are distinguished.

$$\Delta\gamma = \gamma_{\text{substrate}} - \gamma_{\text{overlayer}} - \gamma_{\text{interface}}. \quad (1.1)$$

If $\Delta\gamma > 0$, wetting of the substrate by the deposited material is expected, the so called Franck van der Merwe or layer-by-layer growth mode. In this case, provided the system is always close to thermodynamic equilibrium, a new layer starts to grow only after the previous one is completed. In the opposite case, $\Delta\gamma < 0$, the formation of three dimensional islands is likely to occur (Volmer-Weber growth mode). An intermediate situation appears if $\gamma_{\text{substrate}} > \gamma_{\text{overlayer}}$ but

the overlayer is additionally subject to strain due to lattice mismatch. In this case the effective interface energy increases with thickness and after a number of layers the thermodynamic condition of layer-by-layer growth, $\Delta\gamma > 0$, is violated. This growth mode is referred to as Stranski-Krastanov and is characterized by the initial formation of a wetting layer, followed by the growth of three dimensional islands.

Although useful, this classification has its limitations, *e.g.* it does not consider the case of surface alloying; in the homoepitaxial case, *i.e.* when substrate and adlayer are of the same material it predicts a layer-by-layer growth. However, in reality different growth modes are observed for homoepitaxial systems, *e.g.* Ag forms three dimensional islands on Ag(111) [19, 20]. Transition metals in the middle of the series (*e.g.* Co, Fe) have a higher surface energy than the noble metal substrate (*e.g.* Cu, Ag). Therefore, three dimensional growth is expected from a thermodynamic point of view. However, it is found that Co deposited on Cu(001) grows up to twenty monolayers (ML) in a layer-by-layer mode [12].

These are just a few examples that show that structures obtained from growth experiments do not always fit in the thermodynamic picture. The reason is that under typical growth conditions thermodynamic equilibrium can only rarely be achieved. In general, growth of thin epitaxial films is a non-equilibrium kinetic process in which one or more steps are rate limiting. Thus, by tuning growth parameters like temperature and deposition rate thin film epitaxy provides a possibility to control the morphology and consequently the properties of materials.

In an *atomistic* approach growth structures can be described as a result of a number of microscopic processes like deposition, adsorption, diffusion and desorption of adatoms. Diffusion of atoms can take place on flat regions of the substrate, along or across step edges or around island corners. Therefore, besides adatom diffusion also the adatom-adatom and adatom-step interaction determine island nucleation and growth. In the framework of transition state theory (TST) [21], surface diffusion is described by diffusion rates Γ which are determined by diffusion barriers, E_d , and prefactors, Γ_0 .

$$\Gamma = \Gamma_0 e^{-\frac{E_d}{k_B T}}. \quad (1.2)$$

The diffusion barrier reflects the interaction between adsorbate and substrate. The energy of the systems for different lateral positions of the adsorbate provides the so called potential-energy surface (PES) which consists of minima, maxima and saddle points. The minima correspond to adsorption sites and the saddle points to transition states on the diffusion path. Thus, the diffusion barriers are given as the difference between the energy in the transition state and the adsorption site.

Concerning homoepitaxial growth of metals, considerable information on diffusion barriers has been gained in the last years using experimental techniques like field ion microscopy (FIM) [22–25] and scanning tunneling microscopy (STM) [26]. Theoretically, microscopic processes have been studied by semiempirical methods as the embedded atom method (EAM) [27, 28] and have only recently become accessible to *first principles* calculations [29–32]. However, the quantitative estimation of diffusion parameters in the heteroepitaxial case faces several problems: Experimentally it is difficult to distinguish between the atomic species, especially for systems where intermixing takes place. And on the theory side, semiempirical approaches, although quite successful in treating *sp*-bonded systems (*e.g.* aluminum and noble metals), have considerable difficulties in constructing potentials for elements where *d*-electrons participate in the chemical bond. For such materials *ab initio* total energy calculations can provide reliable information on the atomistic processes.

Time scales relevant for growth experiments are of the order of seconds and the length scales of kinetically controlled structures and islands are of the order of 10 nm and involve a large number of atoms ($> 10^5$). These time and length scales are not (yet) directly accessible to density-functional theory (DFT) calculations which provide a detailed quantum mechanical description of atomistic processes but are restricted to small system sizes up to 100 atoms and 1000 electrons and time scales of *picoseconds* (*e.g.* in *ab initio* molecular dynamics). On the other hand, a phenomenological or statistical approach to growth is offered by nucleation theory [33] or by kinetic Monte Carlo simulations. However, these methods are often based on empirical or semiempirical parameters and their predictive power is therefore limited.

In order to bridge the gap between the microscopic scale accessible to DFT-calculations and the mesoscopic scale of growth experiments we choose here a different strategy to describe the heteroepitaxial growth of Co on Cu(001). We use DFT-calculations to:

- identify adsorption sites;
- determine adsorption energies;
- identify relevant diffusion processes;
- calculate their rates.

Once the rates of microscopic processes are known the growth process can be modeled by a kinetic Monte-Carlo simulation. By construction, such a KMC-simulation provides a *statistical* description of growth on realistic length and time scales and at the same time contains the correct information of the microscopic

processes. As a result the surface morphology is obtained as a function of growth conditions, *e.g.* temperature and deposition rate, and provides the possibility to analyze quantities like island density, island shapes and island size distributions. A similar approach has been up to now used only in the homoepitaxial case to study island shapes in the selfdiffusion of Al(111) [34–36], influence of long-range interactions on the island nucleation of Ag(111) [37], and recently for compound semiconductors (GaAs(001)) [38].

The description of heteroepitaxial growth of metals is a challenging and complex task especially if intermixing plays a role as indicated for several *3d* elements on Cu(001): Fe on Cu(001) [39], Co on Cu(001) [13, 14, 16, 17] and Ni on Cu(001) [41]. In this case two different chemical species, namely, both adatoms of the substrate and the deposited material are involved in growth. Thus, the number of processes that influence morphology is much larger.

1.2 Goal and outline of the thesis

The goal of this thesis is to gain understanding of the heteroepitaxial growth of Co on Cu(001) and provide a theoretical explanation of experimental findings. This comprises a systematic theoretical investigation of the microscopic mechanisms relevant for surface diffusion and growth of mesoscopic islands and thin films of Co on Cu(001). A full description of thin film growth is too complex and would go beyond the scope of this work due to the multitude of atomistic processes and the high numerical cost connected with it. For this reason we focus here on the initial stages of heteroepitaxial growth.

Knowledge of growth in the submonolayer regime is important not only from a technological but also from a fundamental point of view because it provides information on the scaling properties of island density, on the basic mechanisms of island nucleation, and is also relevant for studying multilayer growth.

An important contribution to the understanding of the physical properties of crystals and surfaces has been achieved in the last decades by density-functional theory (DFT). The results in this work are obtained with the *full-potential augmented plane waves method* (FP-LAPW). Due to the special choice of a mixed basis set, *i.e.* atom-centered basis functions with a well-defined angular momentum around the atomic positions and plane waves in the interstitial part, this method is particularly suitable for the treatment of transition metals with their localized *d*-electrons. Further, it contains no approximation on the shape of the potential which makes it applicable to open structures and surfaces. The calculation of the forces on the atoms [78] enables a structural optimization of the investigated

systems. Recent optimizations and implementation of iterative diagonalization schemes [76] increased substantially the efficiency of the code and thus made the treatment of system sizes relevant for growth phenomena feasible. The main features of the method are presented in **Chapter 2**.

A prerequisite to study the kinetic effects is a good knowledge of the surface morphology under thermal equilibrium conditions. In the range of 1ML, experimental results indicate the formation of bilayer islands [12, 13] and at higher temperatures of a copper capping layer [12, 15]. Therefore, in **Chapter 3** we focus on different stable and metastable configurations of Co on Cu(001) up to a coverage of 2ML, *e.g.* single adlayers, bilayers and sandwich structures, and determine the *equilibrium* structure with respect to the surface/formation energy. The observed trends are explained in the light of the structural, magnetic and electronic properties of the systems.

A starting point to investigate the initial growth is to determine what are preferential sites for adsorption of Co adatoms for submonolayer coverages. Motivated by recent STM-results [13, 17], we studied in **Chapter 4** besides the fourfold on-surface adsorption site also a *substitutional* site where the adatom exchanges a substrate atom and is incorporated in the surface. The stability of these adsorbate configurations as a function of coverage and against phase separation in compact islands is investigated. The consequences of substitutional adsorption on the initial growth are quantitatively analyzed, *i.e.* the role of substitutional Co atoms as preferential sites for island nucleation. We note that due to substitutional adsorption of Co besides the on-surface Co also on-surface Cu is generated.

In **Chapter 5** the diffusion barriers for Co and Cu adatoms on flat regions of the Cu(001) surface are determined. In particular we study two mechanisms, *hopping* between adjacent sites over a bridge site and an *exchange* process where the adatom is incorporated in the substrate layer and a substrate atom is ejected on the surface. The results for Cu are compared with experimental and other theoretical values. However for Co the results are to our best knowledge the first in the literature. The different behavior of Co and Cu adatoms is discussed with respect to the chemical bonding and the influence of magnetism.

Another parameter which is decisive for the roughness of steps and thus determines island shape is diffusion along steps. Hopping of Co and Cu adatoms along the $\langle 110 \rangle$ -step on the Cu(001) surface is studied in **Chapter 6**. A qualitative picture of the expected growth mode with respect to the activation temperature of the different diffusion processes is presented.

Chapter 6 focuses on the implementation of the *ab initio* kinetic Monte-Carlo code. Here, kinetic Monte Carlo means that we use a statistical approach to describe growth by choosing randomly different microscopic processes. *Ab initio*

refers to the fact that the rates are obtained from DFT-calculations. The initial version is extended to fcc lattices to describe the relevant features of heteroepitaxial growth, *e.g.* exchange processes and pinning at substitutional Co; different models for the adatom-adatom interaction on the surface are tested. Island morphologies obtained for submonolayer coverages of Co on Cu(001) as a function of temperature are compared to corresponding results for the homoepitaxy of Cu on Cu(001) and the effect of the substitutional adsorption of Co on surface morphology is clarified. Deviations from standard nucleation theory [33] with respect to the scaling behavior of the island density are discussed.

Finally, the results are summarized and an outlook is given in **Chapter 8**.

Chapter 2

Theoretical foundations of the FP-LAPW method

The task we are interested in is to study the energetic, electronic, and magnetic properties of Co/Cu heterostructures, the adsorption and diffusion of single adatoms on the surface. Therefore, the method of choice should fulfill several requirements: it should be suitable to describe the properties of transition metal elements, in particular surfaces and adsorbates systems, predict the energies of different configurations with a high precision and allow a structural optimization. Another important issue is the efficiency of the method because of the large system sizes we are interested in. The FP-LAPW method [42] is based on density-functional theory. In Section 2.1 the most important aspects of DFT relevant for the question of interest are sketched, for further details the reader is referred *e.g.* to the monograph of Parr and Yang [45] or the review article of Jones and Gunnarsson [46]. In Section 2.2 the FP-LAPW method is compared to other band-structure methods with respect to its suitability for the material class we focus on. Furthermore, some general aspects of the FP-LAPW method like the choice of the basis set, and the representation of the potential are discussed. Subsequently the implementation of the FP-LAPW method in the WIEN97-code [71] is presented. Besides the approximation made for the exchange-correlation energy the accuracy of total-energy calculations depends on several parameters which control the numerical handling of the calculations. Their meaning will be addressed as well.

2.1 Density-Functional Theory

The description of a solid material represents a many-body problem. However, the mass of the electrons and the atomic nuclei differ by more than three orders of magnitude, therefore the motion of the atomic nuclei is much slower. This fact is exploited within the Born-Oppenheimer approximation where the electronic and ionic degrees of freedom are decoupled by assuming that the electrons adapt to the instantaneous position of the nuclei before the latter have moved significantly. Still, the quantum-mechanical description of a system of N interacting electrons is a complicated task because of the high complexity of the wave function.

The breakthrough in the parameter-free description of complex electronic systems was accomplished by the development of the density-functional theory by Hohenberg and Kohn [43] and Kohn and Sham [44]. The main idea is that physical quantities as expectation values of quantum-mechanical operators are functionals of the electron density. In particular the energy functional of the system is variational and is minimized for the ground state density. [43]

The idea of Kohn and Sham [44] was to map the many-particle problem onto a single-particle problem retaining the exact description of the many body effects. The energy functional¹ is represented as the sum of three terms:

$$E[n(\mathbf{r})] = T_s[n(\mathbf{r})] + U[n(\mathbf{r})] + E_{xc}[n(\mathbf{r})], \quad (2.1)$$

where $T_s[n(\mathbf{r})]$ is the kinetic energy of a system of noninteracting particles, $U[n(\mathbf{r})]$ is the average Coulomb-interaction of the electrons, consisting of the so called Hartree term, and the interaction of the electrons with the external field generated by the atomic nuclei. The last term, $E_{xc}[n(\mathbf{r})]$, contains the exchange and correlation effects as well as a correction to the kinetic energy due to the interaction of the electrons. The exact form of the exchange-correlation functional is not known and is therefore approximated. The most frequently used form, the local-density approximation (LDA), is based on the assumption that the non-local exchange-correlation energy can be locally described by the exchange- and correlation energy density of a homogeneous electron gas,

$$E_{xc}[n(\mathbf{r})] = \int d^3\mathbf{r} n(\mathbf{r}) \epsilon_{xc}(n(\mathbf{r})). \quad (2.2)$$

Different approximations to $\epsilon_{xc}(n(\mathbf{r}))$ have been used in the literature, the most popular being the one by Hedin and Lundqvist [47], von Barth and Hedin [48], Moruzzi, Janak and Williams [49], Vosko, Wilk, Nusair [51], Perdew and

¹Atomic units are used in the following: $\hbar = 1$, $m = \frac{1}{2}$, $e^2 = 2$. Lengths are measured in units of Bohr's radius $a_0 = 1 \text{ a.u.} = 0.529177 \text{ \AA}$. The energy unit is one Rydberg ($1 \text{ Ry} = 13.6058 \text{ eV}$).

Zunger [52], and Perdew and Wang [53]. The latter three are based on fits obtained from quantum Monte Carlo calculations of Ceperley and Alder [50]. The LDA allows a good description of the ground state properties of solids: equilibrium lattice constants are slightly smaller ($\propto 2\%$) compared to experimental values while cohesive energies are generally overestimated by 30%.

An analogous formulation is applied to spin-polarized systems, the so called local spin-density approximation (LSDA), where the energy and in particular its exchange correlation part is a functional of the spin-up and spin-down densities, $n_+(\mathbf{r})$ and $n_-(\mathbf{r})$. The LSDA has been successful in predicting magnetic properties of materials, however in the case of bulk iron a non-magnetic fcc phase is found to be the ground state while the correct ground state is ferromagnetic bcc.

For systems with strongly localized electrons, *e.g.* like atoms and molecules adsorbed on surfaces, where electron density fluctuations are significant, the local approximation with a homogeneous gas reaches its limits. A natural approach to improve the description of inhomogeneous systems is to include information about the gradient of the density which is done in the generalized gradient approximation (GGA):

$$E_{xc}[n(\mathbf{r})] = \int d^3\mathbf{r} n(\mathbf{r}) \epsilon_{xc}(n(\mathbf{r}), \nabla n(\mathbf{r})). \quad (2.3)$$

With GGA the ground state of iron is correctly reproduced, cohesive and surface energies of materials are generally lower than the ones obtained within LDA thus closer to the experimental values, lattice constants are slightly larger than the experimental ones.

The LDA results in this work are obtained with the parameterization of Perdew and Wang [53], while for GGA we use the one by Perdew, Burke and Ernzerhof [54]. The performance of both approximations of the exchange-correlation functional concerning the questions of interest in this work have been explored thoroughly and will be discussed in the next chapters.

The variational property of the energy functional with respect to the single-particle spin-dependent wave function², $\psi_{\mathbf{k}\nu}^\sigma$, under the condition that the particle number is preserved, leads to the *Kohn-Sham* equations:

$$\left(-\nabla^2 + V_{eff}^\sigma(\mathbf{r})\right) \psi_{\mathbf{k}\nu}^\sigma = \epsilon_{\mathbf{k}\nu}^\sigma \psi_{\mathbf{k}\nu}^\sigma. \quad (2.4)$$

The Kohn-Sham equations are a system of single-particle Schrödinger equations. The effective potential $V_{eff}^\sigma(\mathbf{r})$, the quasiparticle is exposed to, contains all interaction effects, *i.e.* the external potential resulting from the interaction of the

²Note that the spin-dependent densities $n_+(\mathbf{r})$ and $n_-(\mathbf{r})$ are defined as $n_\sigma(\mathbf{r}) = \sum_{\mathbf{k}\nu} \mathbf{f}_{\mathbf{k}\nu} |\psi_{\mathbf{k}\nu}^\sigma(\mathbf{r})|^2$.

electrons with the fixed nuclei, the Hartree term and the exchange-correlation potential:

$$V_{eff}^{\sigma}(\mathbf{r}) = V_{ext}(\mathbf{r}) + \int d^3\mathbf{r}' \frac{n(\mathbf{r}')}{|\mathbf{r} - \mathbf{r}'|} + \frac{\delta E_{xc}[n^+(\mathbf{r}), n^-(\mathbf{r})]}{\delta n^{\sigma}(\mathbf{r})}. \quad (2.5)$$

The solution of the Kohn-Sham (KS) equations requires an iterative procedure: From an initial electron density the potential is generated, subsequently the eigenfunctions are obtained as a solution of the KS-equations. These eigenfunctions are used to construct the new density which in combination with the density of the last step serves as an input for the next iteration. This procedure is repeated until *self-consistency* is reached, *i.e.* the difference between the input and output density fulfills a convergence criterion. This scheme is referred to as *self consistent field* (SCF).

2.2 The FP-LAPW method

Various band-structure methods have been developed to solve the KS-equations. These methods differ in the choice of the basis set. The simplest one consists of plane waves as *e.g.* in the pseudopotential plane wave method (PPW). Plane-waves have several advantages: they build a complete set, they possess the translational symmetry of the lattice and fulfill Bloch's theorem and last but not least they are easy to implement. PPW methods are especially suitable for treatment of semiconductors.

However, for transition metals, where the valence electrons are strongly localized, a very large number of plane waves is needed in order to ensure a good description of the oscillatory character of the wave function close to the atomic nucleus. For the description of the electronic and magnetic properties of such materials *all-electron* methods have proven successful. A common feature of these band-structure methods is the concept of the muffin tin, *i.e.* space is divided into spheres (muffin tins) around the atomic positions and an interstitial region. Inside the muffin tins the basis functions have a well defined angular momentum. While in the LAPW method plane waves are chosen in the interstitial, other methods are based on spherical waves as the Linear Muffin Tin Orbital method (LMTO) [55, 56] and the Korringa-Kohn-Rostoker method [57]. An advantage of the LMTO method in the spherical approximation of the potential is the relatively small basis set of Hankel functions which keep the numerical expense lower than in the FP-LAPW method at the cost of a lower numerical precision. Recent developments going beyond the spherical approximation of the potential as well as the implementation of force-calculation are promising for the description of low-coordination structures [58, 59].

2.2.1 Basis functions: APW and LAPW method

In order to describe accurately the strong oscillations of the wave function around the nucleus on one side but also the periodicity of the crystal potential on the other, a “mixed” basis set is used in the *augmented plane wave* (APW) method, the precursor of the LAPW method, proposed by Slater [60–62]. Inside each *muffin tin* (MT) the basis functions are represented as a product of radial functions and spherical harmonics. In the interstitial region (I) a plane wave expansion is used:

$$\varphi_{\mathbf{G}}(\mathbf{k}, \mathbf{r}) = \begin{cases} e^{i(\mathbf{G}+\mathbf{k})\mathbf{r}} & \mathbf{r} \in I \\ \sum_{lm} A_{lm}^{\alpha\mathbf{G}}(\mathbf{k}) u_l^\alpha(r, \epsilon) Y_L(\hat{\mathbf{r}}) & \mathbf{r} \in MT\alpha, \end{cases} \quad (2.6)$$

where \mathbf{k} is the Bloch vector and \mathbf{G} the reciprocal lattice vector. The coefficients $A_{lm}^{\alpha\mathbf{G}}(\mathbf{k})$ are determined from the requirement that the basis function is continuous at the MT-boundary. The radial function $u_l(r, \epsilon)$ is a solution of the radial Schrödinger equation for the spherical potential $V_{00}^\alpha(r)$ of the atom α :

$$\left\{ -\frac{\partial^2}{\partial r^2} + \frac{l(l+1)}{r^2} + V_{00}^\alpha(r) - \epsilon \right\} r u_l^\alpha(r, \epsilon) = 0. \quad (2.7)$$

The explicit dependence of $u_l^\alpha(r, \epsilon)$ on the energy leads however to a non-linear eigenvalue problem that cannot be solved in a single diagonalization step. Also it is difficult to extend the method beyond the spherically-averaged muffin-tin potential approximation.

In the linearized APW method [55, 63, 64] the explicit dependence of the radial function on the single-particle energy is avoided by expanding the radial function $u_l(r, \epsilon)$ in a Taylor-like series around the energy E_l^α up to the linear term.

$$u_l^\alpha(r, \epsilon) = u_l^\alpha(r, E_l^\alpha) + \dot{u}_l(r, E_l^\alpha)(\epsilon - E_l^\alpha) + \mathcal{O}[(\epsilon - E_l^\alpha)^2]. \quad (2.8)$$

Now the basis functions inside the muffin tin are described as a linear combination of the radial function $u_l^\alpha(r)$ and its energy derivative $\dot{u}_l(r) = \left. \frac{\partial u_l(\epsilon, r)}{\partial \epsilon} \right|_{\epsilon=E_l^\alpha}$.

$$\varphi_{\mathbf{G}}(\mathbf{k}, \mathbf{r}) = \begin{cases} e^{i(\mathbf{G}+\mathbf{k})\mathbf{r}} & \mathbf{r} \in I \\ \sum_{lm} [A_{lm}^{\alpha\mathbf{G}}(\mathbf{k}) u_l^\alpha(r) + B_{lm}^{\alpha\mathbf{G}}(\mathbf{k}) \dot{u}_l^\alpha(r)] Y_{lm}(\hat{\mathbf{r}}) & \mathbf{r} \in MT\alpha. \end{cases} \quad (2.9)$$

The coefficients $A_{lm}^{\alpha\mathbf{G}}(\mathbf{k})$ and $B_{lm}^{\alpha\mathbf{G}}(\mathbf{k})$ are determined by matching the value and the slope of the basis functions at the sphere boundary. This is done by expanding the plane waves into Bessel functions and spherical harmonics:

$$e^{i(\mathbf{k}+\mathbf{G})\mathbf{r}} = \sum_{l=0}^{\infty} \sum_{|m| \leq l} 4\pi i^l j_l(|\mathbf{k} + \mathbf{G}||\mathbf{r}|) Y_L^*(\widehat{\mathbf{k} + \mathbf{G}}) Y_{lm}(\hat{\mathbf{r}}). \quad (2.10)$$

In reality this expansion is truncated at l_{max}^{wf} .

The linearization introduces an error in the wave function of $\mathcal{O}[(\epsilon - E_l^\alpha)^2]$ and of a fourth order in the energy. Due to this high order, the new basis set works well for a reasonable choice of the energy parameter E_l (e.g. the middle of the band is a good approximation). However, a problem arises in the presence of high lying core states with the same orbital quantum number as the valence states. These core states are generally not orthogonal to the corresponding valence states (e.g. $3p$ and $4p$). An efficient way to circumvent this problem is to introduce a so called *local orbital*, i.e. an additional radial function $u_l^\alpha(r, E_l^{\alpha,2})$ added to Eq. 2.9 with a coefficient $C_{lm}^{\alpha\mathbf{G}}(\mathbf{k})$ so that the local orbital vanishes at the sphere boundary. Thus, as the name denotes, the local orbitals are completely localized within the muffin tins and do not contribute to the electron density of the interstitial region.

The solutions of the KS-equations are represented in the basis set by $|\psi_{\mathbf{k}\nu}\rangle = \sum_{|\mathbf{G}| < G_{max}^{wf}} c_{\mathbf{k}\nu}^{\mathbf{G}} |\varphi_{\mathbf{G}}\rangle$. Thus the size of the basis set and consequently the quality of the calculation is determined by the cut off parameter G_{max}^{wf} .

2.2.2 Representation of the potential: FP-LAPW

The *full potential* [65, 66] LAPW method contains no shape approximation of the potential, i.e. besides the constant interstitial potential V_I^0 warping terms ($\mathbf{G} \neq 0$) are considered and in the muffin tin spheres non-spherical contributions are added to the spherical potential $V_{00}^\alpha(r)$.

$$V(\mathbf{r}) = \begin{cases} \sum_{\mathbf{G}} V_i^{\mathbf{G}} e^{i\mathbf{G}\mathbf{r}} & \mathbf{r} \in I \\ \sum_{lm} V_{lm}^\alpha Y_{lm}(\hat{\mathbf{r}}) & \mathbf{r} \in MT\alpha. \end{cases} \quad (2.11)$$

An analogous representation is used for the electron density. The accuracy of the full-potential description is controlled by the cut off G_{max}^{pot} which truncates the sum over the reciprocal vectors in the interstitial region and by l_{max}^{pot} which limits how many non-spherical contributions to the potential are considered in the muffin tin. We note that G_{max}^{pot} has to be chosen at least twice as large as G_{max}^{wf} , because the density (and the potential) are quadratic in the wave function. We point out that not all components $V_{\mathbf{G}}$ and $\rho_{\mathbf{G}}$ are calculated and stored. One takes advantage of the space symmetry, i.e. all \mathbf{G} -vectors with the same length which can be transformed in each other through symmetry operations form the so called *stars*. Thus only one representative per star is calculated. Similarly inside the muffin tin spheres the point group symmetry is utilized and e.g. the potential or density are expanded in *lattice harmonics* instead of spherical harmonics.

2.2.3 Description of surfaces: The super-cell approach

The focus of this work is to investigate metal surfaces, thin films on a substrate of a different material, adatoms adsorbed on a surface and diffusion processes. Therefore we need a method that is able to provide a good description of these systems. In bulk materials the three dimensional periodicity is utilized in Bloch's theorem. On a surface the translational symmetry normal to the surface is broken. Surfaces are simulated by a slab of a finite number of layers. On both sides the slab is limited by a vacuum region. The thickness of the slab is determined by the requirement that both surfaces do not interact through the slab.

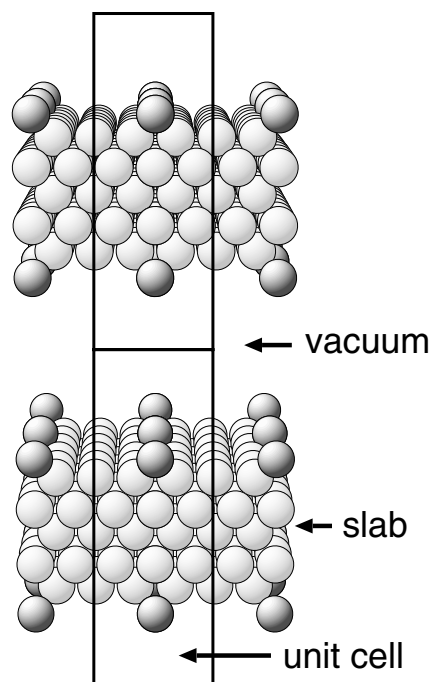


Figure 2.1: Side view of the super-cell geometry of a 5ML thick slab with an adsorbate in a $p(3 \times 3)$ -unit cell. The unit cell is periodically continued in all the three directions

With respect to the description of the vacuum region there are two different versions of the FP-LAPW code. In the so called “*film geometry*” proposed by Krakauer *et al.* [68, 69] the vacuum region is described by an additional basis set consisting of a product of two-dimensional plane waves parallel to the surface and a linear combination of a z -dependent function and its energy derivative. This basis set resembles the construction of the basis functions inside the muffin tin spheres. Similarly, it has to be matched at the vacuum-slab boundary to the plane waves from the interstitial region inside the slab. Although it provides a suitable description of the properties of the wave function outside the

slab the numerical demand is substantially increased because now an additional Schrödinger-like equation has to be solved for the vacuum region.

In the WIEN97-code the so called *super-cell* approach is used. The idea is that the 3-dimensional periodicity is preserved, *i.e.* the slabs are repeated periodically in z direction. The separation between the slabs is chosen large enough to ensure that the electron density fades away towards the center of the vacuum region. With a suitable choice of G_{max}^{pot} the warping terms of the potential and density provide a good description of the corrugation of the potential and density close to the surface. Also in lateral direction one takes advantage of periodicity. In this case the lateral size of the unit cell depends on the system to be studied: *e.g.* for a clean surface a $p(1 \times 1)$ -unit cell is sufficient while in order to simulate isolated adsorbates on the surface the unit cell has to be big enough to avoid interactions between adatoms in neighboring cells. These values vary for the different materials and have to be tested for each case. A schematic representation of the unit cell for a 5ML-thick slab with adatoms adsorbed on both sides in a $p(3 \times 3)$ -unit cell is given in Fig. 2.1.

2.2.4 The WIEN97 code

The structure of the WIEN97 code [71] used in this work will be briefly described in the following. The program package consists of several programs which are controlled by a *shell script*.

The starting density: lstart and dstart

A prerequisite for a quick convergence of the self consistent calculation is a good approximation for the initial electron density. In the WIEN97 code a superposition of atomic densities is generated.

Construction of the effective potential: lcpw0

lcpw0 constructs the effective potential from the electron density. The average Hartree term can be obtained from the charge density via the Poisson equation:

$$\Delta V_H(\mathbf{r}) = 4\pi n(\mathbf{r}). \quad (2.12)$$

The solution of the Poisson equation is particularly simple in reciprocal space:

$$V_H(\mathbf{G}) = \frac{4\pi n(\mathbf{G})}{\mathbf{G}^2}. \quad (2.13)$$

This property has been exploited in the *pseudocharge* method developed by Weinert [70]. The strongly oscillating charge density inside the muffin tins is replaced

by a pseudocharge density \tilde{n} which has a rapidly convergent Fourier expansion inside the MT but the same multipole expansion outside the muffin tin sphere as the true one. This allows to calculate the interstitial potential in reciprocal space. On the other hand the potential inside the muffin tin is determined from a spherically symmetric boundary value problem resulting from matching the potential at the sphere boundary with the interstitial potential.

The exchange-correlation potential is calculated on a mesh in real space. Because the components of the interstitial charge density and potential are stored in reciprocal space, a three dimensional fast Fourier transformation (FFT) and a subsequent backtransformation are needed.

$$n_G \xrightarrow{FFT} n(r_i) \longrightarrow V_{xc}(r_i) \xrightarrow{FFT^{-1}} V_{xc}^G.$$

Inside the muffin tin spheres a least-squares procedure is used to obtain the components of $V_{xc}(r_i, \Omega_i)$ on an angular mesh $\Omega_i = (\theta_i, \phi_i)$ with respect to the basis set of lattice harmonics.

Solution of the Generalized Eigenvalue Problem: lapw1

The calculation of the eigenfunctions from the Kohn-Sham equations in the LAPW-basis set is equivalent to finding the variational coefficients $c_{\mathbf{k}\nu}^{\mathbf{G}}$ from $|\psi_{\mathbf{k}\nu}\rangle = \sum_{\mathbf{G} < \mathbf{G}_{max}^{wf}} c_{\mathbf{k}\nu}^{\mathbf{G}} |\varphi_{\mathbf{G}}\rangle$. The fact that the LAPW-basis functions are not orthogonal leads to a *generalized eigenvalue problem*:

$$\{\mathbf{H} - \epsilon_{\mathbf{k}\nu}\mathbf{S}\} c_{\mathbf{k}\nu} = 0,$$

where \mathbf{H} and \mathbf{S} are the Hamilton and overlap matrix, respectively, which contain a contribution from the muffin tin and the interstitial region. For systems containing inversion symmetry, \mathbf{H} and \mathbf{S} are real thus the storage size and the numerical cost are substantially reduced. In lapw1 the Hamiltonian and the overlap matrix are set up in the LAPW-basis and subsequently the eigenvalue problem is solved. This is the most time-consuming part of the program. However, the recent implementation of iterative diagonalization schemes like Block-Davidson and Lanczos made a substantial speed up possible. [76]

Construction of the new electron density: lapw2

In lapw2 the Fermi energy and the new density of the valence electrons is generated from the eigenvectors. The electron density is given by an integral over the Brillouin zone:

$$n(\mathbf{r}) = \frac{1}{V_{BZ}} \int_{BZ} \sum_{\nu, \epsilon_{\nu}(\mathbf{k}) < E_F} |\psi_{\nu}(\mathbf{k}, \mathbf{r})|^2 d^3k.$$

The integral over the Brillouin zone is substituted by a weighted sum over a discrete number of \mathbf{k} -points, $\int_{\mathbf{k}} f(\mathbf{k}) d^3k \approx \sum_{\mathbf{k}_i=1}^N \omega_{\mathbf{k}_i} f(\mathbf{k}_i)$. For surfaces the Brillouin zone is two-dimensional and correspondingly we have a sampling of \mathbf{k}_{\parallel} -points. Here, the representative \mathbf{k} -points are generated after the scheme of Monkhorst and Pack [92]. The Fermi energy is determined by the requirement that the integral over all occupied states is equal to the total number of electrons. Changes of occupation of the states at the Fermi level can lead to charge sloshing and thus deteriorate convergence. In order to avoid this problem fractional occupation numbers for a Fermi distribution at a non-zero electron temperature are introduced:

$$f_{\mathbf{k}\nu} = \frac{1}{e^{\frac{\epsilon_{\mathbf{k}\nu} - \epsilon_F}{k_B T}} + 1}. \quad (2.14)$$

We note that the energy $k_B T$ does not have the meaning of excitations in the sense of phonons and magnons but of electronic excitations. Introducing the temperature T has the consequence that now the free energy $F = E - TS$ and not E is the variational quantity. Therefore in order to obtain the ground state energy the energy has to be extrapolated to $T \rightarrow 0$ [72–75].

The treatment of the core electrons: lcore

As an *all-electron* method the FP-LAPW method calculates explicitly the core states. The latter are treated self-consistently but separately from the valence states in a basis set in the atomic approximation using the spherical part of the potential.

Generating the input density for the next iteration: mixer

In electronic-structure calculations the energy functional is minimized by calculating the density $n(\mathbf{r})$ self-consistently. After each iteration cycle we obtain a new density $n(\mathbf{r}) = F\{n(\mathbf{r})\}$. Thus finding the ground state density $n_0(\mathbf{r})$ means finding the fix-point of the functional $\mathcal{F}\{n(\mathbf{r})\} = F\{n(\mathbf{r})\} - n(\mathbf{r})$. However, taking the new electron density $n^{m+1}(\mathbf{r}) = F\{n^m(\mathbf{r})\}$ as an input density for the next iteration is in general divergent. Therefore, a procedure is required to generate a new input density $n^{(m+1)}$ from the output $F\{n^m(\mathbf{r})\}$.

In the so called “simple” or Pratt mixing the new input density is determined as a linear combination of $n^{(m)}$ and $F\{n^m\}$:

$$n^{(m+1)} = n^{(m)} + \alpha \mathcal{F}\{n^{(m)}\}. \quad (2.15)$$

For small mixing parameters α this method is very stable but slowly convergent.

In order to improve convergence in the Quasi-Newton methods the information from previous iterations in the form of an approximative Jacobian ($\mathcal{J}\{n(\mathbf{r})\} = \frac{d\mathcal{F}\{n(\mathbf{r})\}}{dn(\mathbf{r})}$) is used:

$$n^{(m+1)} = n^{(m)} - [\mathcal{J}\{n^{(m)}\}]^{-1} \mathcal{F}\{n^{(m)}\}. \quad (2.16)$$

A “mixing” method with good convergence properties is Broyden’s second formula [77], where the inverse of the Jacobian is calculated.

Forces and structural optimization

The WIEN97-code includes also the possibility to calculate the forces on the individual atoms, $\mathbf{F} = -dE_{tot}/d\mathbf{R}$. To the Hellman-Feynman forces which result from the electrostatic interaction of the nucleus with the electrons and the rest of the nuclei the so-called Pulay correction needs to be added due to the fact that the basis set depends on the positions of the atoms and the kinetic energy is discontinuous in the LAPW-basis set. For more detail on the the implementation of the force calculation in the FP-LAPW code, the reader is referred to Ref. [78]. With a damped Newton dynamics it is possible to perform structural optimization using the information from the previous iteration to assure good convergence:

$$R_i^{m+1} = R_i^m + \eta_i (R_i^m - R_i^{m-1}) + \delta_i F_i^m,$$

where R_i^m and F_i^m are the atomic coordinate and the force component at the m -th optimization step, respectively and η_i is the damping factor.

In summary, the WIEN97 FP-LAPW code is a highly accurate method to describe the properties of metals. The choice of the basis set and the super-cell approach makes it also suitable for open structures as surfaces and adsorbate systems. Recent optimizations and implementation of iterative diagonalization techniques [76] achieved a substantial speed up and thus enabled the treatment of larger systems of more than 50 atoms and 1000 electrons. This made the investigation of diffusion phenomena on surfaces feasible. With the help of the force calculation [78] it is possible to optimize the geometry of the studied adsorbate systems. The development of a parallel version of the code, accomplished very recently [79], promises to make even larger system sizes tractable.

Chapter 3

Stable and metastable structures of Cobalt on Cu(001)

3.1 Introduction

Heteroepitaxial structures of Co and Cu exhibit intriguing magnetic properties such as giant magnetoresistance [6], interlayer exchange coupling [80], and surface magnetic anisotropy [81]. Since these properties are closely related to the surface and interface morphology, identification and understanding of the atomic structures and energetics of the adsorption of cobalt on the copper surface are of great interest. Specifically we discuss the [001]-surface orientation. Thin films deposited on a substrate of a different material are generally subject to strain arising from the different lattice parameters of the adsorbate and substrate. Our calculations show that the lattice constant of a ferromagnetic fcc bulk phase of Co is 2.8% smaller than that of a fcc Cu crystal, while the lattice constant of a hypothetical nonmagnetic fcc cobalt crystal is 4.3% smaller than that of the copper crystal. Here we take the fcc structure of cobalt, because it has been shown that a thick epitaxial cobalt film on Cu(001) can be characterized in terms of a tetragonally distorted face centered cubic (fct) phase [82]. The lattice mismatch between cobalt and copper suggests a small tensile strain. However for ultrathin films ($\Theta < 2$ ML) the comparison of the bulk phases of adsorbate and substrate is not necessarily very relevant. For example total-energy calculations [83] show that the equilibrium lattice constant of an unsupported Co monolayer is 14.1% (nonmagnetic case) and 12.2% (ferromagnetic case) smaller than the Cu bulk lattice constant, implying that an ultrathin film might be subject to a much stronger tensile strain than a thick overlayer. The relation between lattice mismatch and relaxation of the interlayer spacing will be discussed in Section 3.4 below.

While experimental studies of coverages above 2ML show that growth proceeds in an almost perfect layer-by-layer mode, for the initial two layers a deviation from the Frank-van der Merwe (FM) growth mode and a strong dependence on the growth conditions was reported [13]. Angle-resolved X-ray photoemission spectroscopy (ARXPS) data [12] indicate that the second layer begins to form before the first layer is completed. Assuming the coexistence of areas of clean Cu(001) surface and of monolayer and bilayer islands, a LEED analysis [84] estimated that for a total coverage of one monolayer and deposition rates ranging between 0.016 and 0.33 ML/s the area covered by bilayer islands at room temperature is 20 – 40%. Fassbender *et al.* [13] performed STM-experiments at room temperature for a total coverage of 1.35 ML and report that the fractional layer filling depends strongly on the deposition rate. For a low (0.003 ML/s) deposition rate they found that the first layer was closed and 0.35ML were in the second layer, while for a high deposition rate (0.3 ML/s) 15% of the surface was still uncovered and about 50% of the surface was already covered by bilayer high islands.

X-ray photoemission scattering (XPS) [12], Auger electron scattering(AES) and STM measurements [15] show an increase of the Cu signal and decrease of the Co signal upon annealing which was interpreted as segregation of substrate material on top of the cobalt layer. Similar results were reported for Fe/Cu(001) [85]. This effect was explained in terms of the lower surface energy of Cu compared to Co. We note that the application of this argument to thin film systems is not trivial because of the energy cost of the additionally created Cu/Co interface. Yet our studies show that in the case of Co on Cu(001) the contribution of the interface energy is very small (see Section 3.3).

The impact of morphological changes on the magnetic properties of Co/Cu(001) was recently investigated with X-ray magnetic circular dichroism (XMCD) and magneto optical Kerr effect (MOKE) [86] experiments. At a cobalt coverage of 1.8 ML a sudden jump of the Curie temperature was measured which changed strongly with time or a subsequent heat treatment. The authors speculated that the critical thickness coincides with the thickness at which bilayer cobalt islands coalesce.

Depending on growth conditions (temperature, deposition rate), significantly different structures are observed experimentally. Although the magnetic properties of Co on Cu(001) have been the subject of many theoretical studies, a systematic theoretical analysis of the different configurations and their relative stability is still lacking. Moreover most of the calculations [88, 89] have used slabs with atomic positions frozen to the bulk coordinates of the substrate, neglecting thus the structural relaxation of the clean Cu(001) surface and of the Co/Cu(001) adsorbate system.

In this Chapter we focus on the behavior of Co on Cu(001) under thermodynamic equilibrium conditions. We performed density-functional theory calculations considering a variety of configurations ($\theta \leq 2$ ML). In particular we discuss two aspects: the formation of multilayer cobalt islands and sandwich structures with a copper capping. For each system we performed a full structure optimization and establish the relation between the energetic trends and the structural, magnetic and electronic properties. The Chapter is organized as follows: The details of the calculations are given in Section 3.2. In Section 3.3 we discuss the stability of the systems against separation in multilayer islands and the influence of the capping layer. The structural (Section 3.4), magnetic (Section 3.5) and electronic (Section 3.6) properties of mono- and bilayer cobalt films on Cu(001), as well as of the corresponding copper capped systems are investigated. Finally in Section 3.7 we address the similarities and differences between Co/Cu(001) and Co/Cu(111) referring to STM and *ab initio* results for the [111]-orientation [90]. The results are summarized in Section 3.8.

3.2 Computational details

Our calculations are performed using density-functional theory (DFT). The exchange-correlation functional is treated within the local-density approximation (LDA) [53] and for the magnetic systems we performed spin-polarized calculations within the local spin-density approximation (LSDA). We also examined the possible importance of non-local exchange correlation effects by employing the generalized-gradient approximation (GGA) in the parameterization of Perdew, Burke, and Ernzerhof [54]. The results show that for the systems studied in this Chapter LDA and GGA give the same structural and energetic trends. More details on this issue will be discussed in the Appendix at the end of this Chapter.

The Kohn-Sham equation was solved applying the full-potential linearized augmented plane wave (FP-LAPW) method [71, 76]. The surface is simulated by repeated slabs separated in z -direction by a vacuum region. Co is adsorbed on both sides of the substrate. The thickness of the vacuum region between the slabs, corresponding to 6 Cu layers (10.65 Å), is found to be sufficient to avoid interactions of the Co atoms. The interlayer distances d_{12} and d_{23} were optimized with a damped Newton dynamics and the relaxations $\Delta d_{12}/d_0$ and $\Delta d_{23}/d_0$ are given with respect to the interlayer spacing of a Cu crystal, d_0 . Referring the Co-Cu and for Co bilayer systems even the Co-Co interlayer distances to the interlayer spacing of Cu is probably not an optimum choice, but it is well defined and has been the common practice for such adsorbate systems. We therefore use

this convention here as well.

The lattice constant for the fcc copper crystal $a_{\text{Cu}} = 3.55 \text{ \AA}$, obtained from a non-relativistic calculation, is 1.6% smaller than the measured one (3.61 \AA), 0.1% of which reflects our neglect of zero point vibrations in the theory. The lateral lattice parameter of the Cu substrate was set to the calculated lattice constant for a fcc copper crystal. We chose a muffin tin (MT) radius of $R_{\text{Cu}}^{\text{MT}} = 2.20 \text{ bohr}$ for the Cu atoms and a slightly smaller radius $R_{\text{Co}}^{\text{MT}} = 2.15 \text{ bohr}$ for the Co atoms to prevent overlap of the MT spheres due to the strong relaxation found for some systems.

The stability of various systems is analyzed with respect to the formation energy. Assuming that the slab is in thermal equilibrium with a Co and a Cu crystal, acting as reservoirs of Co and Cu atoms, the formation energy in eV per (1×1) -unit cell is defined as:

$$E^{\text{f}} = \frac{1}{2A} (E^{\text{slab}} - N_{\text{Cu}} E_{\text{Cu}}^{\text{bulk}} - N_{\text{Co}} E_{\text{Co}}^{\text{bulk}}), \quad (3.1)$$

where A is the area of the surface unit cell of the considered slab [91] and the factor 2 accounts for the presence of two surfaces of the slab. N_{Cu} and N_{Co} are the number of Cu and Co atoms in the slab supercell and $E_{\text{Cu}}^{\text{bulk}}$ and $E_{\text{Co}}^{\text{bulk}}$ are the energies of a Cu or a Co atom in the respective fcc bulk crystals at the theoretical equilibrium lattice constants. Thus for a pure Cu slab ($N_{\text{Co}} = 0$) E^{f} is the Cu surface energy, and for a pure cobalt slab ($N_{\text{Cu}} = 0$) with $a_{\parallel} = a_{\text{Co}}$ it is the surface energy of cobalt.

The LAPW wave functions within the muffin tins (MTs) were expanded in spherical-harmonics with angular momenta up to $l_{\text{max}}^{\text{wf}} = 10$. Non-spherical contributions to the electron density and potential within the MTs were considered up to $l_{\text{max}}^{\text{pot.}} = 4$. The cutoff for the Fourier-series expansion of the interstitial electron density and potential was chosen to be $G_{\text{max}} = 12.0 \text{ bohr}^{-1}$. Extensive convergence tests with respect to \mathbf{k}_{\parallel} -point set and the energy cutoff for the basis set were performed for a 5-layer Co(001) slab at the lattice constant of copper and relaxed interlayer distance. The results are shown in Table 3.1. A numerical accuracy of 6% for the formation energy is achieved with $E_{\text{cut}} = 12.8 \text{ Ry}$, while $E_{\text{cut}} = 15.6 \text{ Ry}$ is needed for an accuracy of 1%. Thus a cutoff parameter of 15.6 Ry was chosen throughout the calculations. The Brillouin-zone integration was performed with a special point set generated after the scheme of Monkhorst and Pack [92]. We obtained an accuracy of the Brillouin-zone integration better than 1% by using 21 \mathbf{k}_{\parallel} -points in the irreducible wedge of the Brillouin-zone (IBZ) (see Table 3.1).

The bulk energies needed as a reference to determine the formation energy (see Eq.(3.1)) were calculated using the same LAPW-parameters as in the slab calculations. For the bulk calculation 104 \mathbf{k} -points in the IBZ were used.

$N_{\mathbf{k}_{\parallel}}$	E_{cut} [Ry]	E^{f} [eV/(1 × 1)-cell]	ϕ [eV]
6	15.6	1.50	5.27
15	15.6	1.51	5.29
21	15.6	1.51	5.29
28	15.6	1.51	5.28
36	15.6	1.51	5.28
45	15.6	1.51	5.28
21	12.8	1.58	5.31
21	13.8	1.53	5.29
21	17.5	1.50	5.27

Table 3.1: Convergence tests performed within LDA for a 5-layer slab of Co(001) strained at the lattice constant of copper and interlayer distance optimized for $N_{\mathbf{k}_{\parallel}} = 28$. The surface energy E^{f} and work function ϕ are given as a function of the plane wave cut-off E_{cut} and the number of \mathbf{k}_{\parallel} -points in the irreducible part of the Brillouin zone $N_{\mathbf{k}_{\parallel}}$.

Prior to investigating the effects of adsorption of cobalt, we checked the required thickness of a copper slab, to ensure a good representation of the properties of the clean Cu(001)-surface. The surface energies, work functions and interlayer relaxations for slabs of 3, 5, 7, and 9 layers of copper are compared in Table 3.2. For a 5-layer slab the relaxation between surface and subsurface layer of -3.01% is close to the experimental value obtained by MEIS [93] (-2.4%) while the LEED-result [94] is smaller ($-1.1 \pm 0.4\%$). The calculated work function $\phi = 4.78$ eV is in good agreement with experiment: 4.59 ± 0.05 eV [95], 4.76 eV [96], and 4.77 ± 0.05 eV [97].

A further requirement of the thickness of the slab is that the interaction of the Co layers on both sides of the slab through the substrate is negligible for the questions of concern. To test the strength of this interaction we studied the

N_{layer}	E^{f} [eV/(1 × 1)-cell]	ϕ [eV]	$\Delta d_{12}/d_0$ [%]
3	0.79	4.91	-2.93
5	0.78	4.78	-3.01
7	0.78	4.83	-3.10
9	0.78	4.82	-3.11

Table 3.2: DFT-LDA results for the surface energy E^{f} , work functions ϕ , and relaxation $\Delta d_{12}/d_0$ of the clean Cu(001)-surface are given as a function of the number of slab layers N_{layer} , $N_{\mathbf{k}} = 21$, $E_{\text{cut}} = 15.0$ [Ry].

N_{layer}	E^{f} [eV/(1×1)-cell]	ϕ [eV]
3	1.767	5.31
5	1.754	5.31
7	1.753	5.30
9	1.759	5.30

Table 3.3: Formation energy and work functions for 1Co/Cu(001) with optimized inter-layer distances as a function of the number of substrate layers N_{layer} .

formation energy and work function for 1ML Co on Cu(001) (1Co/Cu(001)) as a function of the substrate thickness. The results are summarized in Table 3.3. Both the formation energy and work function converge quickly with the substrate thickness. On the basis of these results we conclude that a 5-layer copper slab represents a good approximation of the Cu(001)-surface.

3.3 Formation energy and stability

In order to identify the equilibrium configuration of Co on Cu(001) we investigate in this Section the tendency towards separation in multilayer islands and the influence of a copper capping layer. The studied systems include the clean Cu(001) surface, a monolayer and bilayer thick cobalt film on Cu(001) denoted by 1Co/Cu(001) and 2Co/Cu(001), respectively, as well as the corresponding capped systems, 1Cu/1Co/Cu(001) and 1Cu/2Co/Cu(001). Additionally we investigated a bilayer Co-Cu-c(2×2)-alloy. The calculated formation energies and the work functions are given in Table 3.4. We consider several ways in which a total coverage of 1ML Co can be arranged on a Cu(001) surface. The energy of a system consisting of more than one domain, namely regions of clean copper surface and regions covered by large cobalt islands, is simply given by the weighted sum of the formation energy of the clean Cu(001) surface and those of the Co-island. Under the assumption that the islands are large, the contributions of the step edges and side facets of the islands are negligible and were not taken into account. A schematic presentation of the different structures is given in Fig. 3.1 together with energy changes with respect to the case where the whole surface is covered by a monolayer thick (1×1)-cobalt layer.

Our calculations show that a monolayer film, Fig. 3.1(a), would separate into a clean Cu(001)-surface and a bilayer island, Fig. 3.1(b). For the nonmagnetic case the gain in energy is $\Delta E^{\text{NM}} = 0.59$ eV/(1×1)-cell and for the ferromagnetic case it is $\Delta E^{\text{FM}} = 0.41$ eV/(1×1)-cell. This result can be explained in terms of the higher coordination of the cobalt atoms in the bilayer film and correlates with the

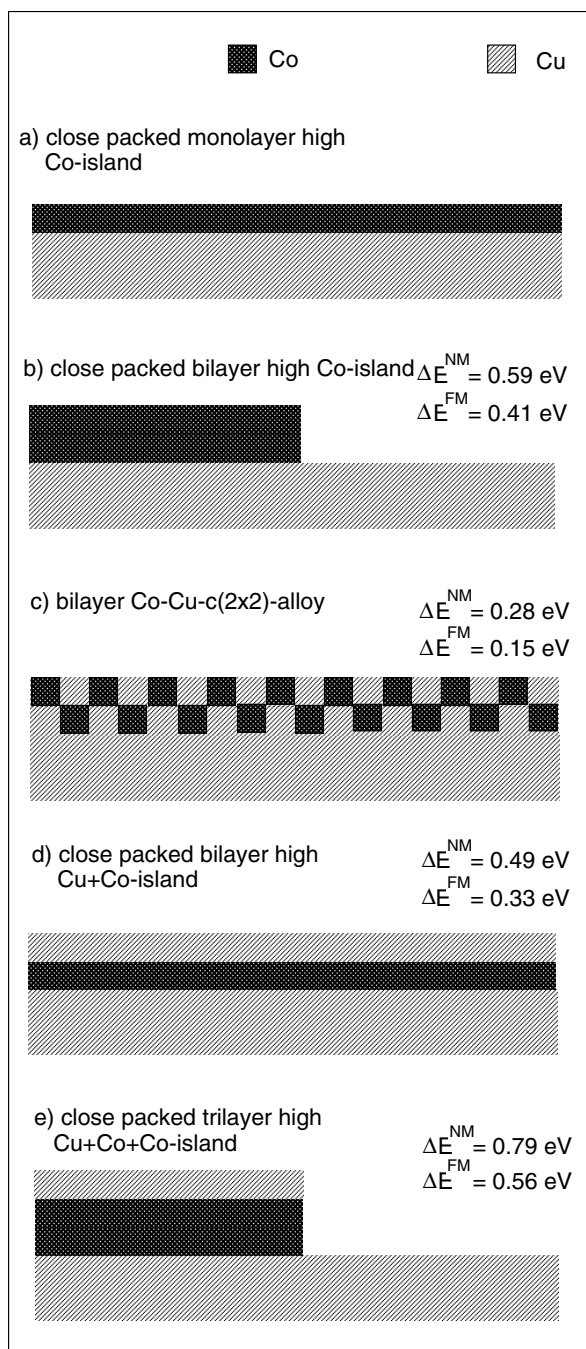


Figure 3.1: Schematic diagram of the different adsorbate configurations for a Co coverage of $\Theta = 1.0 \text{ ML}$. The formation energy changes for configurations b)-e) in the nonmagnetic ΔE^{NM} and ferromagnetic case ΔE^{FM} is given with respect to formation energy of the close packed monolayer high island shown in a).

System	E^f [eV/(1 × 1)-cell]	ϕ [eV]
Cu(001)	0.78	4.78
1Co/Cu(001) NM	1.75	5.31
1Co/Cu(001) FM	1.51	5.16
2Co/Cu(001) NM	1.55	5.38
2Co/Cu(001) FM	1.42	4.88
1Cu/1Co/Cu(001) NM	1.27	4.89
1Cu/1Co/Cu(001) FM	1.18	4.81
1Cu/2Co/Cu(001) NM	1.14	4.74
1Cu/2Co/Cu(001) FM	1.12	4.82
bilayer Co-Cu-c(2 × 2)-alloy NM	1.48	5.18
bilayer Co-Cu-c(2 × 2)-alloy FM	1.36	4.97

Table 3.4: Formation energies E^f and the work functions ϕ for various structures.

substantial broadening of the cobalt d -band and the strong relaxation between Co layers in 2Co/Cu(001) as will be discussed later in this Chapter. Concerning the effect of magnetism, we see that it reduces, but does not change the tendency towards formation of bilayer islands.

Experimental studies [12, 15] show that copper segregates onto the surface after annealing. Therefore we study here the influence of a copper capping layer on stability. Covering 1Co/Cu(001) with a monolayer of copper, Fig. 3.1(d), reduces the energy of the system by $\Delta E^{\text{NM}} = 0.49$ eV/(1 × 1)-cell. Compared to the cobalt terminated systems the copper-capped systems gain less spin-polarization energy because of the hybridization with the capping layer. Consequently the energy gain due to a capping layer for the magnetically ordered system is lower than the one for the nonmagnetic: ($\Delta E^{\text{FM}} = 0.33$ eV/(1 × 1)-cell). The influence of the capping layer on the magnetic properties of the copper covered systems will be discussed in Section 3.5. Saúl and Weissmann [98] recently calculated the surface segregation energy of $3d$ -impurities (Fe, Co, Ni) in Pd, Ag, and Cu. They found, in agreement with our results, that embedding in the bulk of the host material is connected with a substantial gain in energy both for nonmagnetic and magnetic impurities/(layers), the effect being weaker for the latter. We also note that the copper capping layer in the 1Cu/1Co/Cu(001) and 1Cu/2Co/Cu(001) systems has properties similar to the clean Cu(001)-surface; for example we find that the work functions of the systems are $\phi_{\text{Cu}(001)} = 4.78$ eV, $\phi_{1\text{Cu}/1\text{Co}/\text{Cu}(001)} = 4.89$ eV, and $\phi_{1\text{Cu}/2\text{Co}/\text{Cu}(001)} = 4.74$ eV.

Recent combined STM and RHEED experiments [16] detected ordered c(2 × 2) regions when a total coverage of 1ML Co was deposited on Cu(001) at room

System	E_{NM}^{I}	E_{FM}^{I}
... Cu/1Co/Cu...	0.163	0.113
... Cu/2Co/Cu...	0.044	0.066
... Cu/3Co/Cu...	-0.005	0.046

Table 3.5: Interface energies given in [eV/(1 × 1)-cell] for nonmagnetic (E_{NM}^{I}) and ferromagnetic (E_{FM}^{I}) systems as a function of the cobalt interlayer thickness.

temperature and subsequently annealed at 450 K. Motivated by these results, we studied a configuration, where starting from 1Co/Cu(001) every other Co atom is replaced by a Cu atom in the substrate layer underneath. In this way a bilayer $c(2 \times 2)$ -alloy [99], shown schematically in Fig. 3.1(c), is formed. We find that this configuration is by 0.28 eV/(1 × 1)-cell (nonmagnetic) and 0.15 eV/(1 × 1)-cell (ferromagnetic case) more favorable than the (1 × 1)-monolayer in Fig. 3.1(a). However, it is a metastable structure because transition into a cobalt monolayer covered by copper, 1Cu/1Co/Cu(001) in Fig. 3.1(d), leads to an energy gain of 0.22 [eV/(1 × 1)-cell] (nonmagnetic) and 0.18 eV/(1 × 1)-cell (ferromagnetic case). Thus, the bilayer $c(2 \times 2)$ -alloy lies energetically between the 1Co/Cu(001) and 1Cu/1Co/Cu(001) systems and it may be stabilized kinetically. This surface alloy might also represent a favorable configuration with respect to surface strain relief. Indeed a $c(2 \times 2)$ -pattern was observed experimentally preferentially in the middle of large islands [100].

We also studied whether the cobalt (1 × 1)-layer will prefer to be buried deeper in the substrate. Our calculations for the 1Cu/1Co/Cu(001) and 2Cu/1Co/Cu(001) systems show that there is no additional energy gain through covering the system with a thicker copper layer.

The segregation of Cu on the surface is typically explained by the lower surface energy of Cu(001) compared to Co(001). Still this argument is only applicable if the interface energy were small and thus negligible. In order to calculate the energy cost to create an interface we studied three different systems with one, two and three cobalt interlayers in copper bulk, marked as (... Cu/1Co/Cu...), (... Cu/2Co/Cu...) and (... Cu/3Co/Cu...), respectively. Here the lateral parameter is set to the copper bulk value while the interlayer distances are relaxed. The interface energies, E^{I} , are calculated analogously to the formation energies [compare Eq.(3.1)]. In order to subtract the effect of elastic strain due to the lattice mismatch of the two materials we use as a reference energy for cobalt the bulk energy of fct cobalt with $a_{\parallel} = a_{\text{Cu}}$ and relaxed a_z [101] instead of the one of fcc cobalt at the cobalt lattice constant. Table 3.5 lists the results for nonmagnetic and ferromagnetic cobalt interlayers. It shows that the values of

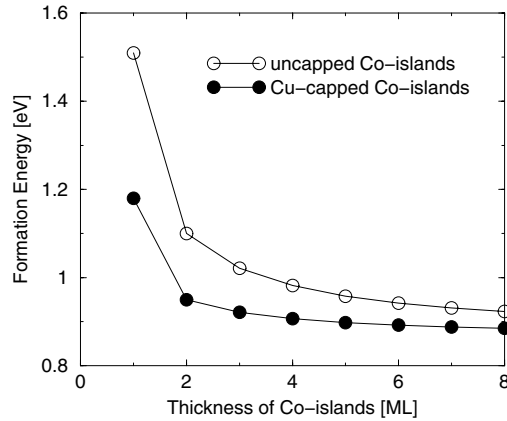


Figure 3.2: Formation energy of different ferromagnetically ordered configurations for a total cobalt coverage of 1 ML as a function of the cobalt island thickness N . The structures consist of clean Cu(001) and a compact island with N Co layers (\circ) or N Co-layers capped by copper. The area covered by the cobalt islands is $\frac{1}{N}$ of the whole surface. Especially for the copper terminated systems the separation in higher than bilayer cobalt islands is unlikely because of a negligible energy gain.

E^I for a cobalt bilayer and trilayer are very close, i.e. the interface energy converges quickly with the thickness of the cobalt layer. The interface energy is indeed significantly smaller than the difference of the surface energies of the clean Cu(001)-surface ($E^f = 0.79$ eV/(1 × 1)-cell) and a thick Co(001) film with a lateral parameter fixed to the lattice constant of copper and relaxed interlayer distances ($E_{\text{NM}}^f = 1.21$ eV/(1 × 1)-cell [102] and $E_{\text{FM}}^f = 1.11$ eV/(1 × 1)-cell [102]). For this reason the common argument that simply the surface energy difference of cobalt and copper explains the segregation of substrate material on the surface works in the case of Co on Cu(001).

In analogy to the Co terminated system, the single Co layer capped by Cu shown in Fig. 3.1(d) will tend to separate into a clean Cu(001) surface and a double Co layer capped by Cu, Fig. 3.1(e). Still the energy gain due to phase separation [$\Delta E^{\text{NM}} = 0.31$ eV/(1 × 1)-cell, $\Delta E^{\text{FM}} = 0.23$ eV/(1 × 1)-cell] is only about half the energy gain for the system with Co on the surface. We can summarize that both the magnetic ordering and the capping layer weaken the tendency towards cobalt clustering but *qualitatively* we observe the same behavior with and without magnetism.

Yet we need to find out whether the bilayer film will be stable or if higher cobalt islands may form. In order to determine the formation energy of a N -layer ($N > 2$) thick cobalt island we assume that each of the *intermediate* cobalt layers

has an energy of a bulk atom in a tetragonal cobalt crystal with $a_{\parallel} = a_{\text{Cu}}$ and fully relaxed a_z [101]. The elastic energy contribution is the difference between the energy of cobalt bulk at the fcc cobalt lattice constant and the energy of fct cobalt as described above and amounts to 0.11 eV (NM) and 0.08 eV (FM) per cobalt atom. Thus the formation energy of a N -layer cobalt film is

$$E_{N\text{Co}/\text{Cu}(001)}^{\text{f}} = E_{2\text{Co}/\text{Cu}(001)}^{\text{f}} + (N - 2)E^{\text{elast.}}. \quad (3.2)$$

For a total coverage of 1ML the formation energy of a configuration consisting of clean Cu(001) surface and a N -layers high cobalt island is given by:

$$E_{N\text{Co-island}}^{\text{f}} = \frac{1}{N}E_{N\text{Co}/\text{Cu}(001)}^{\text{f}} + \frac{N - 1}{N}E_{\text{Cu}(001)}^{\text{f}}. \quad (3.3)$$

An analogous expression for the formation energy holds for the copper capped systems. The formation energy of the ferromagnetically ordered capped and uncapped systems is plotted in Fig. 3.2 as a function of cobalt-island height N . In the following we will concentrate on the Cu-terminated systems because, as can be seen from Fig. 3.2, they are always lower in energy. The substantial energy gain due to separation of a monolayer-thick cobalt film in bilayer islands was already discussed above. Yet further separation in higher cobalt islands brings only a small energy gain, e.g., the gain due to separation from bilayer in trilayer islands for the Cu-terminated islands is about 0.03 eV/(1 × 1)-cell. We note that this energy gain is mainly due to the increase of the clean Cu(001)-surface. Moreover the cost of the island facets, which was not taken into account in the present discussion, grows with island height. Because of the small energy gain, as shown in Fig. 3.2, and the increasing cost of the sidewalls the formation of islands higher than bilayer is unlikely. We conclude that the ferromagnetically ordered configuration in Fig. 3.1(e), which is by 0.56 eV/(1 × 1)-cell more favorable than the one in Fig. 3.1(a), represents the thermodynamic equilibrium structure.

3.4 Structural properties

In the previous Section we identified the bilayer cobalt island covered by a copper capping layer as the thermodynamically stable structure. However, crystal growth represents a situation which is more or less far from thermodynamic equilibrium therefore not only the equilibrium structure but also other, metastable, structures (e.g. those shown in Fig. 3.1) may occur. In this Section we present the results of a geometry optimization for monolayer and bilayer (1 × 1)- as well as copper-capped systems. The Co films are assumed to grow pseudomorphically on the Cu(001)-surface, adopting the lateral spacing of the Cu crystal. The calculated relaxation of the interlayer spacing for the nonmagnetic and ferromagnetic

Method	$\Delta d_{12}/d_0$ [%]	$\Delta d_{23}/d_0$ [%]
1ML Co/Cu(001)		
FP-LAPW NM	-4.7%	-0.3%
FP-LAPW FM	-3.0%	0.0%
LEED [1]	-6.0%	-6.0%
LEED [84]	-2.5%	-1.4%
2ML Co/Cu(001)		
FP-LAPW NM	-17.0%	0.0%
FP-LAPW FM	-13.4%	-0.8%
LEED [84]	-2.0%	-4.2%
1ML Cu/1ML Co/Cu(001)		
FP-LAPW NM	-7.0%	-3.0%
FP-LAPW FM	-5.6%	-2.0%
1ML Cu/2ML Co/Cu(001)		
FP-LAPW NM	-5.0%	-14.8%
FP-LAPW FM	-4.6%	-12.5%

Table 3.6: Relaxation $\Delta d_{12}/d_0$ and $\Delta d_{23}/d_0$ of the interlayer spacing in % for the first two layers compared to the lattice parameter of Cu bulk, d_0 .

systems is given in Table 3.6. We remind the reader that all relaxations are given with respect to the interlayer spacing in copper bulk.

The first interlayer spacing in the monolayer film, $d_{\text{Co-Cu}}$, shows an inward relaxation of 4.7% for the nonmagnetic case, which reduces to 3.0% for the ferromagnetic film. At the same time the interlayer spacing between the first and second substrate layer, which is contracted by 3.0% for the clean Cu(001) surface, expands back to the bulk value -0.3% (0.0%) for the nonmagnetic (ferromagnetic) system. This result can be explained in terms of the bond-cutting model. Due to the missing bonds of the surface atoms the strength of the remaining bonds to the subsurface layer is enhanced, giving rise to an inward relaxation [108]. The bond strength is also related to the d -band occupation [108], thus Co-Cu bonds are stronger than Cu-Cu bonds and consequently upon cobalt adsorption we observe a stronger relaxation of the Co-Cu-interlayer distance, while the Cu-Cu distance expands. Previous *ab initio* results [87] found a relaxation of the first interlayer distance of the ferromagnetic 1Co/Cu(001) surface of -10.4%. The reason for the discrepancy with our result (which is -3.0%) is in the choice of the lateral lattice parameter. While we use a non-relativistic treatment of the valence

electrons and the corresponding theoretical equilibrium lattice constant of Cu (3.55 Å), Wu and Freeman [87] used a semi-relativistic treatment which gives a noticeably smaller lattice constant (3.52 Å). Nevertheless, in their adsorbate study Wu and Freeman [87] set the lateral lattice parameter to the substantially larger experimental value (3.61 Å). As a consequence, the strong interlayer relaxation found by Wu and Freeman [87] just reflects that their copper surface is under tensile strain. We tested this and indeed could reproduce the effect: When we use a semi-relativistic treatment of the valence electrons and still force the Cu substrate to assume the experimental lattice constant we obtain $\Delta d_{12}/d_0 = -7.9\%$ and $\Delta d_{23}/d_0 = -2.3\%$.

For the bilayer Co film we obtain a surprisingly strong contraction of the interlayer distance of $d_{\text{Co-Co}}$ of -17% in the nonmagnetic case. For the ferromagnetically ordered system the contraction is somewhat smaller, -13.4% , due to the magnetovolume effect. These results can hardly be explained by comparing the lattice constant of the fcc bulk phase of Co with that of bulk Cu. Such comparison would give a lattice mismatch of -4.3% in the nonmagnetic and -2.8% in the ferromagnetic case. Thus, in such description one would say that the Co film is strained, but that the effect is not very large. However, it is questionable whether the comparison of the bulk lattice parameters of the two materials, is a good approach for understanding ultrathin films with $\Theta \leq 2$ ML. For example, total-energy calculations based on the FP-LAPW method [83] show that the difference between the equilibrium lattice constant of a *free standing* cobalt monolayer and that of the Cu substrate is -14.1% for a nonmagnetic and -12.2% for a ferromagnetic monolayer [104]. Therefore, if we refer the strain in the Co adlayers to the lattice parameter of the free-standing Co layer, the strain is significant, and the above noted interlayer relaxation then simply reflects the reaction of the Co film to this big strain. Indeed, we think that this description is appropriate (in a qualitative sense) because for a very thin cobalt film ($\Theta \leq 2$ ML) the bonding to the noble metal substrate can only partially replace the bonds to missing cobalt neighbors. Thus, the adsorbed film will still bear some resemblance to the free-standing one. The above result also indicates that the weaker binding to the substrate is balanced by forming a strong bond between the two cobalt layers.

The competition between Co-Co and Co-Cu-bonding is also a driving force for the structural changes in the capped systems. The hybridization with the copper capping layer has the general effect of weakening the existing Co-Cu and Co-Co bonds in the 1Co/Cu(001) and the 2Co/Cu(001) system, respectively. Consequently, the interlayer distance between the cobalt and copper layer increases from -4.7% (NM) and -3.0% (FM) in 1Co/Cu(001) to -3.0% (NM) and -2.0% (FM) in 1Cu/1Co/Cu(001). Similarly the strong relaxation between the two cobalt

layers decreases from -17.0% (NM) and -13.4% (FM) in $2\text{Co}/\text{Cu}(001)$ to -14.8% (NM) and -12.5% (FM) in $1\text{Cu}/2\text{Co}/\text{Cu}(001)$. On the other hand the stronger Co-Co bond induces a weaker binding with the capping layer which is reflected in the smaller inward relaxation of the distance between the capping layer and the cobalt film of -5.0% for the $1\text{Cu}/2\text{Co}/\text{Cu}(001)$ system compared to -7.0% for the $1\text{Cu}/1\text{Co}/\text{Cu}(001)$ system.

Table 3.6 also contains structural data determined with LEED. We note, however, that such structural analysis is complicated and not unambiguous, because, as discussed above, in the $\text{Co}/\text{Cu}(001)$ system several domains and/or metastable structures may coexist. In the absence of knowledge about these various structures and their energies, it appeared to be a reasonable choice for Clarke *et al.* [1] to assume that Co on $\text{Cu}(001)$ will form a full Co monolayer. And based on this assumption they determined an inward relaxation of -6% for both $d_{\text{Co}-\text{Cu}}$ and $d_{\text{Cu}-\text{Cu}}$. Our work, however, shows that the $1\text{Co}/\text{Cu}(001)$ system is unstable with respect to the formation of bilayer islands and capped bilayers structures. In a more recent LEED study Cerda *et al.* [84] assumed the coexistence of regions of clean $\text{Cu}(001)$, Co monolayer and Co bilayer islands, but Co layers with a Cu capping layer, which we find to have the lowest total energy, were not considered. Thus, in both experimental analyses the model assumptions did not include all relevant systems.

3.5 Magnetic properties

The layer-resolved magnetic moments in the four systems studied, $1\text{Co}/\text{Cu}(001)$, $2\text{Co}/\text{Cu}(001)$, $1\text{Cu}/1\text{Co}/\text{Cu}(001)$ and $1\text{Cu}/2\text{Co}/\text{Cu}(001)$ are given in Table 3.7. To be precise, these are the contributions from the muffin tin region only. The top layer in $1\text{Co}/\text{Cu}(001)$ exhibits an enhanced magnetic moment ($M_{\text{Co}(S)} = 1.71 \mu_B$) compared to the bulk value of $1.52 \mu_B$, calculated at the equilibrium lattice constant of cobalt. This is due to the larger lateral constant of the epitaxial cobalt adlayer and to the reduced coordination on the surface. Further we find that the surface layer of the $2\text{Co}/\text{Cu}(001)$ system exhibits the same magnetic moment ($1.71 \mu_B$) as the $1\text{Co}/\text{Cu}(001)$ system. In fact, a thick fcc cobalt film at the lattice constant of copper also has a similar moment, namely $1.78 \mu_B$. However, the magnetic moment of the subsurface Co layer, which binds to the Cu substrate, is reduced to $1.47 \mu_B$. The corresponding magnetic moment of subsurface cobalt in a thick fcc cobalt film at the lattice constant of copper is $1.62 \mu_B$. The lower magnetic moment of subsurface cobalt is a consequence of the higher coordination and the strong contraction of the interlayer spacing $d_{\text{Co}-\text{Co}}$.

The hybridization with the copper capping layer reduces the magnetic moment of the first Co layer both in the 1Cu/1Co/Cu(001) and 1Cu/2Co/Cu(001) systems by about $0.3 \mu_B$ compared to the 1Co/Cu(001) and 2Co/Cu(001) systems. It is interesting to note that both Co layers in 1Cu/2Co/Cu(001) have the same magnetic moment ($1.38 \mu_B$) which can be explained by the fact that Co(S-1) and Co(S-2) have the same coordination of Co and Cu atoms.

To our knowledge magnetic moments for 1Co/Cu(001) have not yet been measured due to the already discussed difficulties in the preparation of a single cobalt

System	layer	$M [\mu_B]$
1Co/Cu(001)	Cu(C)	-0.004
	Cu(S-2)	-0.014
	Cu(S-1)	0.024
	Co(S)	1.711
2Co/Cu(001)	Cu(C)	-0.002
	Cu(S-3)	-0.009
	Cu(S-2)	0.016
	Co(S-1)	1.472
	Co(S)	1.706
Co(001) at a_{Cu}	Co(C)	1.648
	Co(S-1)	1.615
	Co(S)	1.783
1Cu/1Co/Cu(001)	Cu(C)	-0.001
	Cu(S-3)	-0.008
	Cu(S-2)	0.027
	Co(S-1)	1.445
	Cu(S)	0.040
1Cu/2Co/Cu(001)	Cu(C)	-0.001
	Cu(S-4)	-0.007
	Cu(S-3)	0.022
	Co(S-2)	1.383
	Co(S-1)	1.374
	Cu(S)	0.035

Table 3.7: Layer resolved local magnetic moments in the ferromagnetic systems in $[\mu_B]$ as obtained from the slab calculation. S, S-1, S-2, etc. denote the position of the corresponding layer with respect to the surface, S being the surface layer and C being the central layer of the slab.

monolayer on Cu(001). Our calculated value of the surface magnetic moment of 1Co/Cu(001), $1.71 \mu_B$, is slightly lower than that obtained in previous calculations, e.g. $1.78 \mu_B$ [87] and $1.76 \mu_B$ [88] from FP-LAPW and $1.85 \mu_B$ [89] from FP-LMTO (full-potential linearized muffin tin orbitals) calculations. The differences are attributed mainly to the use of the experimental lattice constant of copper (3.61 \AA) and/or the lack of considering the interlayer relaxation in Refs. [87–89] (see also Section 3.4).

The magnetic moments of 1.9 ML and 2.1 ML of Co deposited on Cu(001) measured with x-ray magnetic circular dichroism (XMCD) are $1.71 \pm 0.1 \mu_B$ [105] and $1.77 \pm 0.1 \mu_B$ [106], respectively. The XMCD-spectra were recorded at 40 K, but information about the preparation conditions, which could tell whether the Co layers were capped by Cu, is not available. Yet, the magnetic moment compares well with our calculated magnetic moment for 2Co/Cu(001). With respect to other theoretical work, we note that the same trend of an enhanced magnetic moment in the surface layer ($1.85 \mu_B$) and a reduced magnetic moment in the subsurface layer ($1.60 \mu_B$) was found in a previous FP-LAPW calculation for 2Co/Cu(001) [107]. In this study the lateral parameter was fixed to the experimental lattice constant of copper and relaxation of the interlayer spacing was not taken into account. However, the strong relaxation of the interlayer spacing in 2Co/Cu(001) discussed in Section 3.4 has a noticeable influence on the magnetic moments and cannot be neglected.

Our results reveal also that the adsorbed cobalt film induces a small polarization in the substrate. The magnetic moment of the copper layer at the interface is positive, e.g. in 1Co/Cu(001) it is $0.024 \mu_B$. Then, in the next layer it switches to a negative value ($-0.014 \mu_B$). Also the central layer of our 5-layer Cu slab has a very small negative moment, $-0.004 \mu_B$. The oscillation of the magnetic moment perpendicular to the surface indicates the formation of a spin-density wave. This striking effect is observed for all four studied systems. However, we note that for a detailed investigation of this effect, a thicker substrate slab has to be considered. The magnetic moment induced in the capping layer is somewhat larger than the one induced in the substrate layer: $0.040 \mu_B$ in 1Cu/1Co/Cu(001) and $0.035 \mu_B$ in 1Cu/2Co/Cu(001).

3.6 Electronic properties

The calculated electronic properties are consistent with the above discussed structural and energetic trends. The left column of Fig. 3.3 shows the local density of states (LDOS) of the d -bands of the adsorbate and substrate layers obtained

from a nonmagnetic calculation. For 1Co/Cu(001) the Co d -band is rather narrow, the LDOS at the Fermi level is very high and the overlap with the copper d -band is small, which reflects that the interaction between Co and Cu is not very strong. For the 2Co/Cu(001) system the d -states of the surface and subsurface Co layers overlap and their d -bands receive a substantial broadening. At the same time the LDOS at the Fermi level is lowered. The broadening of the cobalt d -bands in 2Co/Cu(001) is an indication for the strong interaction between the two cobalt layers. The same effect of broadening of the d -band of Co is observed for 1Cu/2Co/Cu(001) compared to the Co d -band in 1Cu/1Co/Cu(001).

The layer-resolved LDOS of the d -bands for the ferromagnetic systems is given in the right column of Fig. 3.3. The majority band of Co is completely filled and the minority band is only partially filled, reflecting the fact that Co is a strong ferromagnet. For 1CoFM/Cu(001) and 1Cu/1CoFM/Cu(001) the Fermi level crosses the minority d -band of cobalt almost at its maximum while for 2CoFM/Cu(001) and 1Cu/2CoFM/Cu(001) the Fermi level lies in a dip of the Co d -bands. A “harder” electronic structure, i.e. lower density at the Fermi level is typically considered an indication for a more stable system.

Both majority and minority d -bands of copper are occupied and lie ca. 2 eV below the Fermi level. Still the minority and majority d -band have a very different structure with the majority band being broader in general. Actually the band width correlates with the strength of interaction with the cobalt film: While there is a substantial overlap between the majority d -bands of cobalt and the substrate layer beneath or the capping layer above, the corresponding minority bands have a very small overlap.

3.7 Comparison of Co/Cu(001) and Co/Cu(111)

Prior to our work Pedersen *et al.* [90] studied the growth of Co on the (111) surface of Cu with STM and LMTO-calculations. The STM measurements showed that the islands consist of several cobalt layers with the lowest layer possibly growing subsurface. At elevated temperatures vacancy islands formed in the terraces close to steps and the substrate material etched from these holes covered the cobalt islands.

Comparing the LMTO calculations for nonmagnetic systems with [111]-orientation [90] with our FP-LAPW results for the [001]-orientation we note that the general behavior is similar: The systems are unstable against phase separation and clustering. The energy gain from the separation of a monolayer film in a bilayer island and a clean Cu surface is $\Delta E_{(001)} = 0.59$ eV/(1 × 1)-cell and

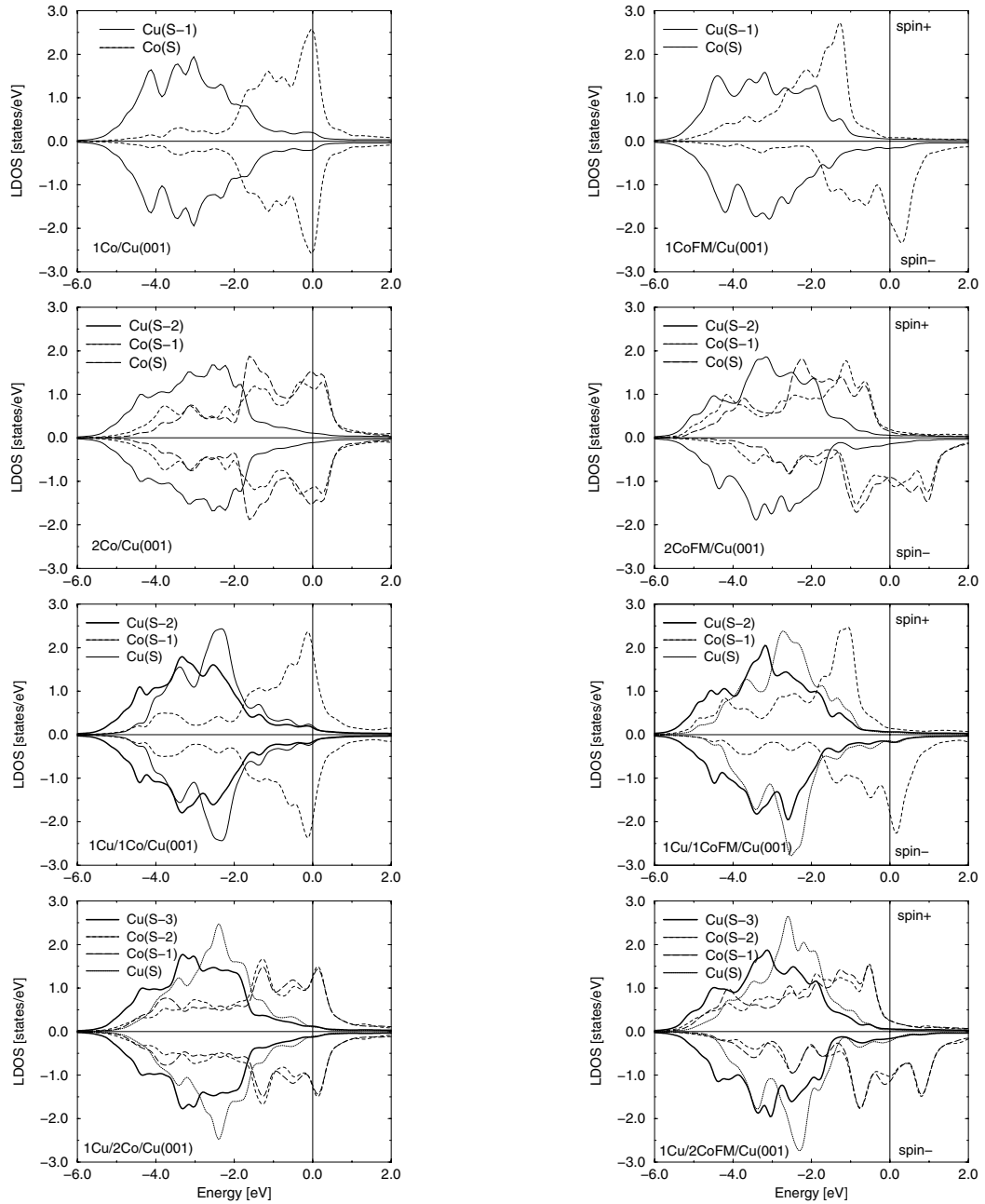


Figure 3.3: LDOS of the d -bands of the different atomic layers in the nonmagnetic (left) and ferromagnetically ordered (right column) systems. S, S-1, S-2, S-3 denote the surface and the subsequent subsurface layers, respectively. The contribution from inside the muffin-tin spheres is displayed. The Co bands are marked with dashed and long-dashed lines, the Cu bands with a solid line. The calculated LDOS was broadened by a Gaussian with a width of $2\sigma = 0.2$ eV.

$\Delta E_{(111)} = 0.39$ eV/(1 × 1)-cell respectively. The corresponding energy gain for the capped systems is $\Delta E_{(100)} = 0.31$ eV/(1 × 1)-cell and $\Delta E_{(111)} = 0.18$ eV/(1 × 1)-cell.

The segregation of Cu onto the surface lowers the energy of the system for both orientations: for monolayer coverages $\Delta E_{(100)} = 0.49$ eV/(1 × 1)-cell and $\Delta E_{(111)} = 0.30$ eV/(1 × 1)-cell; for 2ML of Co $\Delta E_{(100)} = 0.42$ eV/(1 × 1)-cell and $\Delta E_{(111)} = 0.20$ eV/(1 × 1)-cell.

Still in all cases the energy gain is lower for the (111) surface than the (100) surface. This trend reflects the difference in coordination numbers: In a bond cutting model of metallic bonding the energy of an atom roughly scales as the square root of the local coordination [103, 109]. Adsorption of a Co layer or of a Cu capping layer implies a change of coordination of the atoms in the added layer from 4 to 8 for the [100]- and from 6 to 9 for the [111]-orientation. And for the atoms in the layer, which after adsorption becomes the second layer, the coordination changes from 8 to 12 for the [100]- and from 9 to 12 for the [111]-orientation. Thus, the energy gain is smaller for the [111]-orientation than for the [100]-orientation.

3.8 Summary

In summary, we have identified a bilayer cobalt island covered by copper as the lowest energy configuration. However, growth is ruled by kinetics. Therefore, it is expected that under realistic conditions metastable structures may exist at surfaces, and some examples were identified in this Chapter. Total-energy considerations show that the (1 × 1)-film tends to separate into areas of bilayer cobalt islands and clean copper surface, and this is indeed in line with experimental observations of bilayer growth [12, 84, 110]. Our total-energy and electron density of states results show that the stability of the bilayer film is due to the fact that the Co atoms prefer to attain a high coordination of alike atoms. A consequence of this is the very strong contraction of the interlayer distance between the two cobalt layers and the substantial broadening of the cobalt *d*-bands in the adsorbed Co-bilayer as compared to the *d*-band of a single Co adlayer.

The segregation of substrate material onto the Co adlayer results in a substantial energy gain 0.5 eV/(1 × 1)-cell). We also studied a two-layer surface alloy of Co and Cu with a *c*(2 × 2) periodicity. This is found to be energetically less favorable than a separation into Cu-capped Co bilayer-islands, but at strained regions of the surface this surface alloy may be stabilized. Indeed, a *c*(2 × 2) surface structure was observed in recent combined STM and RHEED experiments [16].

Generally, the ferromagnetically ordered systems are lower in energy than the

nonmagnetic, but the relative stability of different configurations remains qualitatively unchanged by magnetism and the structural trends are well described by the nonmagnetic systems.

3.9 Appendix

For several systems we performed calculations with the LDA [53] and with the GGA [54]. The formation energies for 1Co/Cu(001) (NM and FM), 2Co/Cu(001) (NM and FM), 1Cu/1Co/Cu(001), and 1Cu/2Co/Cu(001) are given in Table 3.8. The lateral parameter was set to the lattice constants of copper obtained within the LDA and GGA approach, respectively. The LDA value 3.55 Å is 1.7% smaller than the measured one, 3.61 Å, while with the GGA the lattice parameter (3.65 Å) is 1.1% bigger than the experimental value (zero-point vibrations are neglected in the theory).

The formation energies obtained with the GGA are generally lower than the LDA results and the differences are between 0.2 and 0.3 eV/(1 × 1)-cell. This effect was also observed previously for the clean copper surface [111]. Yet the trends between the different configurations remain unchanged. For example the energy gain from the separation of a monolayer cobalt film in a bilayer cobalt island and clean Cu(001)-surface is 0.60 eV/(1 × 1)-cell (LDA) and 0.53 eV/(1 × 1)-cell (GGA) for the nonmagnetic systems and 0.41 eV/(1 × 1)-cell (LDA) and 0.36 eV/(1 × 1)-cell (GGA) for the ferromagnetically ordered systems. The equilibrium configuration of clean copper surface with bilayer cobalt islands, covered by copper (see Fig. 3.1(f)), is by 0.79 eV/(1 × 1)-cell (LDA) and by 0.74 eV/(1 × 1)-cell (GGA) more favorable than 1Co/Cu(001) in Fig. 3.1(a).

System	$E_{\text{LDA}}^{\text{f}}$	$E_{\text{GGA}}^{\text{f}}$
Cu(001)	0.78	0.61
1Co/Cu(001) NM	1.75	1.47
1Co/Cu(001) FM	1.54	1.22
2Co/Cu(001) NM	1.55	1.27
2Co/Cu(001) FM	1.48	1.11
1Cu/1Co/Cu(001) NM	1.26	0.99
1Cu/2Co/Cu(001) NM	1.13	0.85

Table 3.8: The formation energies $E_{\text{LDA}}^{\text{f}}$ and $E_{\text{GGA}}^{\text{f}}$ of the different configurations calculated within LDA and GGA, respectively, given in [eV/(1 × 1)-cell]. The lateral parameter is set to the corresponding (LDA or GGA) equilibrium lattice constant of copper.

A structural optimization was performed for all systems listed in Table 3.8 using both approaches, LDA and GGA. No noticeable differences were obtained except for the systems, containing a bilayer cobalt film, where the contraction of the distance between the two cobalt layers was slightly stronger with the GGA, e.g. for 2Co/Cu(001) $\Delta d_{\text{Co-Co}}^{\text{LDA}}/d_0^{\text{LDA}} = 17\%$ and $\Delta d_{\text{Co-Co}}^{\text{GGA}}/d_0^{\text{GGA}} = 18.6\%$. However, these minor differences do not alter the discussion in Section 3.4.

The larger lateral parameter in GGA produces a substantial enhancement of the magnetic moments, e.g. the surface magnetic moment of cobalt in 1Co/Cu(001) changes from $1.71 \mu_B$ (LSDA) to $1.86 \mu_B$ (GGA) and in 2Co/Cu(001) from $M_{\text{Co}(S)}^{\text{LSDA}} = 1.71 \mu_B$ and $M_{\text{Co}(S-1)}^{\text{LSDA}} = 1.47 \mu_B$ to $M_{\text{Co}(S)}^{\text{GGA}} = 1.81 \mu_B$ and $M_{\text{Co}(S-1)}^{\text{GGA}} = 1.64 \mu_B$. This result is not surprising and is in line with the changes of the magnetic moment for fcc cobalt bulk from $1.52 \mu_B$ (LSDA) to $1.69 \mu_B$ (GGA).

In conclusion, both approximations of the exchange-correlation potential, LDA and GGA, lead to the same results for the structural, energetic, and magnetic properties of the configurations studied in this work.

Chapter 4

Initial Adsorption of Cobalt on Cu(001)

4.1 Introduction

Experimental techniques like atomic force and scanning tunneling microscopy, and theoretical approaches based on density-functional theory (DFT) represent a powerful tool to study the early stages of growth on an atomic scale. The current understanding of epitaxial growth is that deposited atoms diffuse between high symmetry on-surface sites and typically island nuclei are formed due to binary collisions where often a dimer represents a stable island [34]. However, it is questionable whether this picture applies also in the case of heteroepitaxy. Indeed, it was shown that in this case other scenarios may become relevant [40, 113]: e.g., it is possible that the diffusing adatom exchanges site with a substrate atom and is incorporated in the substrate layer, thus already the monomer constitutes a stable nucleus. Substitutional adsorption and the formation of a surface alloy may occur even for materials that are immiscible in the bulk as recently reported for example for Na on Al(100) and Al(111) [73, 115], Mn on Cu(001) [116], Fe on Cu(001) [39] and Cr on Fe(001) [117, 118].

Co on Cu(001) is another system where surface intermixing plays a role. Despite a low solid miscibility [114] and a small lattice mismatch (the ferromagnetic fcc bulk phase of Co is 2.8% smaller than that of a fcc Cu crystal) Fassbender *et al.* [13] observed Co-rich regions in the substrate and copper-rich regions in the top-layer were identified via a bias dependent contrast reversal in STM-images of 0.12 ML. This result is unexpected, because previous calculations [119] found that at $\Theta = 0.5$ ML an ordered surface alloy is unstable and should tend to separate into Co islands and areas of clean Cu(001)-surface.

Fassbender *et al.* [13] explained the intermixing with the surface energy difference of the two materials. Yet, our calculations [129] show (cf. Chapter 3) that the surface energy difference would rather lead to cobalt clustering and at higher temperatures to copper capping. Bilayer cobalt islands covered by a copper layer were identified as the equilibrium structure. However, in the dilute limit under typical growth conditions the system would be far from thermal equilibrium.

In this Chapter we focus on the adsorption of submonolayer coverages of Co on Cu(001). In particular in Section 4.3 two different adsorption geometries are studied: on-surface where the adatom occupies a fourfold hollow site on the surface and substitutional, where it exchanges a substrate atom and is incorporated in the substrate layer. The energetic trends are explained in the light of the structural and electronic effects that take place upon adsorption. In Section 4.4 we investigate different cobalt coverages to identify the importance of the adatom-adatom and adatom-substrate interaction. We further consider the stability of monolayer thick surface alloys against phase separation in compact Co islands and its dependence on coverage. The influence of magnetism on the energetic trends and the magnetic properties of the adsorbate systems are discussed in Section 4.5.

The atomic exchange processes in conjunction with their coverage dependence lead to three different adatom species on the surface: substitutional Co, on-surface Co, and on-surface Cu. The DFT-calculations confirm that the substitutional Co adatoms act as *nucleation* centers, as suggested previously by Fassbender *et al.* [13], and their attractive potential is investigated quantitatively in Section 4.6. The influence of these pinning centers on the initial growth is observed in island size distributions for different substrate temperatures and deviations from standard nucleation theory [33] are discussed. A *bimodal* growth mode characterized by two different types of islands with respect to size and chemical composition is predicted on the basis of DFT-calculations and indeed identified in a CO-titration experiment. [17]. Finally, the results are summarized in Section 4.7.

4.2 Computational details

The results in this Chapter are obtained within LDA and LSDA for nonmagnetic and spin-polarized systems, respectively. The influence of gradient corrections to the exchange-correlation functional on the adsorption energies for submonolayer coverages is discussed in the Appendix at the end of this Chapter.

As in the previous chapter, the lateral lattice parameter of the Cu substrate

was set to the value calculated for a fcc copper crystal (non-relativistic calculation), $a_{\text{Cu}} = 3.55 \text{ \AA}$. We chose a muffin tin (MT) radius of $R_{\text{Cu}}^{\text{MT}} = 2.20 \text{ bohr}$ for the Cu atoms and a slightly smaller radius $R_{\text{Co}}^{\text{MT}} = 2.15 \text{ bohr}$ for the Co atoms to prevent overlap of the MT spheres upon the strong relaxation found for some systems.

The convergence of the LAPW-calculation with respect to thickness of the substrate and other parameters was tested carefully. For details the reader is referred to Section 3.2. The Cu(001)-surface was modeled by a 5-layer copper slab which ensures that the interaction of the adsorbates through the substrate is negligible for the questions of interest in this work. The thickness of the vacuum between the repeated slabs amounts to 18 \AA . The cut off parameters used in the LAPW calculation are summarized shortly in the following: in the muffin tin spheres the wave functions were expanded in spherical harmonics with an angular momentum up to $l_{\text{max}}^{\text{wf}} = 10$. Non-spherical contributions to the electron density and potential within the MTs were considered up to $l_{\text{max}}^{\text{pot.}} = 4$. The cutoff for the Fourier-series expansion of the interstitial electron density and potential was chosen to be $G_{\text{max}} = 12.0 \text{ bohr}^{-1}$ and the cutoff for the plane wave basis set $E_{\text{cut}} = 15.6 \text{ Ry}$. The Brillouin-zone integration was performed with a special \mathbf{k}_{\parallel} -point set generated after the scheme of Monkhorst and Pack [92]. An accuracy better than 1% is obtained by using 144 \mathbf{k}_{\parallel} -points in the Brillouin-zone (BZ) for a $p(1 \times 1)$ -structure. For the bigger unit cells, $c(2 \times 2)$, $p(2 \times 2)$, and $p(3 \times 3)$, we use a corresponding mesh of 100, 36, and 16 \mathbf{k}_{\parallel} -points in the BZ respectively, so as to obtain the same sampling in the reciprocal space. For energy differences the numerical accuracy is better than 0.02 eV per atom.

The bulk and free atom energies needed as a reference to determine the adsorption energy (see Eq. 4.1) were calculated for the same LAPW parameters as in the slab calculations. For the bulk calculation 104 k-points in the irreducible wedge of the BZ were used. The isolated atom was simulated in a box with next nearest neighbor distance of 15 bohr to avoid interaction between the atoms in neighboring unit cells. The cohesive energies for fcc Cu and Co within LDA (4.50 eV and 6.48 eV, respectively) are in good agreement with previous calculations [120] and by 1.0 eV and 2.09 eV higher than the experimental values cited therein. We note, that the overestimation of the cohesive energy compared to experiment is a well-known effect of LDA.

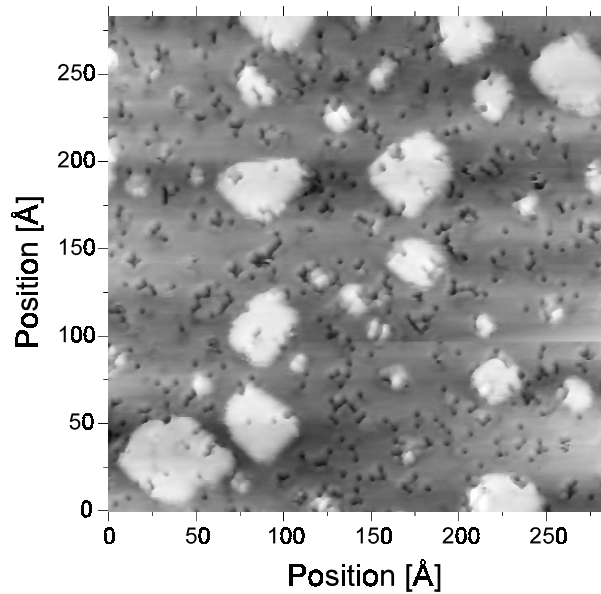


Figure 4.1: STM image ($U_{\text{tip}} = 0.9$ V, $I = 0.4$ nA) of 0.12 ML Co deposited on Cu(001) at room temperature [17]. Small indentations (dark grey) are interpreted as incorporated Co atoms (see text).

4.3 On-surface versus substitutional site: structural, energetic and electronic trends

In a STM-study Fassbender *et al.* [13] observed a bias voltage dependent contrast inversion in STM images for submonolayer coverages which they attributed to surface intermixing. The recent STM investigation of Nouvertné *et al.* [17] found after deposition of 0.12 ML of Co on Cu(001) at room temperature atomically resolved dark indentations in the substrate layer as well as the first layer islands. The corresponding STM image is shown in Fig. 4.1. The light-grey imaged islands of the first layer have an approximately rectangular shape with edges along the $[110]$ - and the $[1\bar{1}0]$ -direction of the substrate. The height of these islands above the substrate is imaged as 1.8 ± 0.2 Å which equals the height of a monoatomic step. A striking feature are the small dark indentations in the uncovered grey substrate region as well as in the islands with an imaged depth of 0.6 ± 0.1 Å with reference to the respective surface. Monoatomic inclusions are clearly visible together with small agglomerates. Even within these agglomerates the atomic arrangement is resolved.

However due to the interplay of electronic and geometric effects the chemical nature of atoms and the composition of islands can typically not be identified unambiguously if only STM-topography data are available. A theoretical investi-

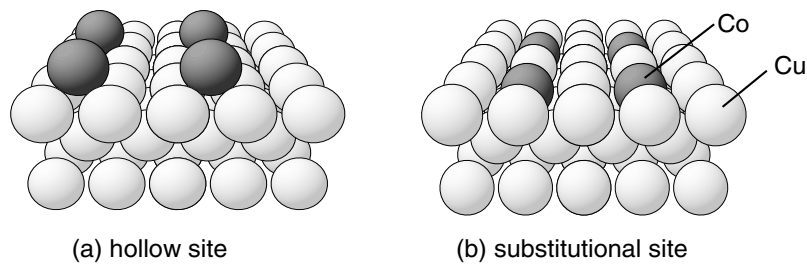


Figure 4.2: Side view of a Cu(001)- $p(2 \times 2)$ -Co structure with Co adatoms at (a) on-surface hollow or (b) substitutional adsorption site.

gation can be helpful to determine the stability of different adsorption geometries and the electronic effects underlying the structural trends. In this Section we study the adsorption of Co atoms on two adsorption sites: on-surface with a Co atom on a fcc hollow site, and substitutional with the Co atom incorporated in the substrate layer. The energetic stability of the different adsorbate configurations is related to the electronic and structural effects accompanying the adsorption process.

The geometries of a $p(2 \times 2)$ -structure with Co atoms on a fcc hollow or substitutional site are shown in Fig. 4.2. For the on-surface adsorption in a $p(2 \times 2)$ -geometry we found a substantial reduction (16%) of the distance between adsorbate and substrate layer with respect to the interlayer spacing of the copper crystal, causing an energy gain of 0.28 eV compared to the unrelaxed structure. This relaxation is connected with a decrease of the next nearest neighbor distance and thus represents an effective increase of the coordination number of the adsorbate. On the other hand for Cu(001)- $p(2 \times 2)$ -Co-sub the adatom relaxes 7% inwards, while the Cu atoms in the surface layer relax by -3% . Thus the relative relaxation of the adatom with respect to the Cu surface layer is -4% and the adatom-adatom interaction is therefore screened. The energy gain due to relaxation is negligible in this case.

Epitaxial growth is a non-equilibrium situation. However, if the deposition rate is not too high, structures in local thermal equilibrium can evolve. For this reason we determine stable and metastable geometries with respect to the adsorption energy per cobalt adatom, e.g. if 0.25 ML of cobalt are adsorbed on the surface the adsorption energy E^{ad} is defined as:

$$E^{\text{ad}} = \frac{1}{2} \left(E^{\text{Cu}(001)} - 2N^{\text{Cu}} E^{\text{Cu-bulk}} + 2N^{\text{Co}} E^{\text{Co-atom}} - E^{\text{Cu}(001)-(2 \times 2)\text{-Co}} \right). \quad (4.1)$$

Here $E^{\text{Cu}(001)}$ and $E^{\text{Cu}(001)-(2 \times 2)\text{-Co}}$ are the total energies of a clean copper surface

and the adsorbate system, respectively, $E^{\text{Cu-bulk}}$ is the fcc bulk energy of Cu, and $E^{\text{Co-atom}}$ is the energy of the free spin-polarized Co atom. The factor $\frac{1}{2}$ in Eq. 4.1 accounts for the presence of two surfaces of the slab. The adsorption energy for the on-surface adsorption ($N^{\text{Cu}} = 0$, $N^{\text{Co}} = 1$) is $E_{\text{on-surf.}}^{\text{ad}} = 3.94$ eV. For substitutional adsorption where the cobalt atom exchanges a copper atom in the substrate layer the expelled Cu adatom is assumed to diffuse to a step and be rebound at a kink site where its energy equals the cohesive energy of copper [121], ($N^{\text{Cu}} = N^{\text{Co}} = 1$). In this case we obtain $E_{\text{sub.}}^{\text{ad}} = 5.26$ eV, i.e. the substitutional adsorption is energetically favored by 1.32 eV over the on-surface adsorption.

The substitutional adsorption as defined in Eq. 4.1 can be considered as a composite process consisting of the removal of a surface Cu atom, the adsorption of the Co adatom into the so formed surface vacancy, and the subsequent adsorption of the Cu atom at a kink site of a copper step or island. This scenario is very likely because the copper adatoms are quite mobile [111] and therefore should be able to reach steps which exist on the surface under normal growth conditions. We also considered an intermediate state of the composite process where the kicked out Cu adatom occupies a fourfold hollow site as a nearest neighbor of the embedded Co atom (see Fig 4.12a). For 0.11 ML of Co in a $p(3 \times 3)$ -geometry the energy difference between the on-surface Co and intermediate state configuration amounts to 0.72 eV compared to 1.36 eV for the final state of the exchange process as defined in Eq. 4.1. Thus, the remaining 0.64 eV is the energy gain of the copper adatom at a kink site compared to Cu as a nearest neighbor of the embedded Co atom. In a recent second moment tight-binding approximation (TB-SMA) study, where N -body potentials were fitted to experimental elastic constants and first-principles values, Levanov *et al.* [122] found the energy gain between the initial (on-surface) and intermediate state (which they called “direct” exchange) to be 0.50 eV, which gives the same qualitative trend as the DFT-LDA result.

In order to understand this result one has to keep in mind that the d -states of cobalt take part in the chemical bonding. Thus, cobalt prefers to occupy a highly coordinated site. In the on-surface adsorption geometry the cobalt adatom has four Cu neighbors whereas in the substitutional adsorption the Co atom has eight nearest neighbors. The electronic effects connected with the adsorption of cobalt are displayed in Figs. 4.3 and 4.4. The solid lines represent the muffin tin contributions to the total density of states (DOS) of the Co adatom and its nearest (NN) and next nearest (NNN) Cu neighbors in the surface and subsurface layer for both adsorption geometries. The position of the Fermi level relative to the peaks in the density of states determines the occupation of the states and the nature of bonding. For a free standing Co- $p(2 \times 2)$ -layer (not shown here) the

Fermi level crosses the narrow atomic-like $3d$ -band close to the peak maximum. In the adsorbate systems the interaction with the substrate leads to a broadening

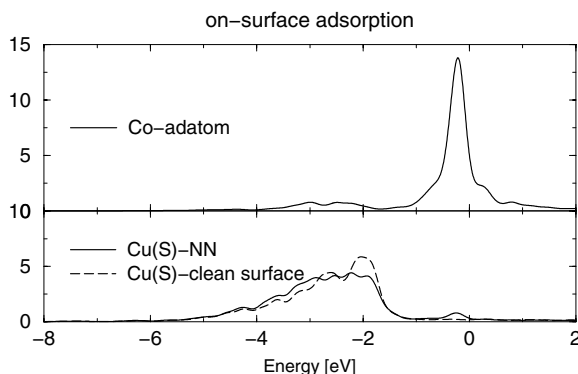


Figure 4.3: The muffin tin contributions to the total density of states of the Co-atom and its Cu nearest neighbor (Cu(S)-NN) in Cu(001)- $p(2 \times 2)$ -Co (solid line) and of the corresponding Cu atom in the clean Cu(001)-surface (dashed line). The calculated DOS were broadened by a Gaussian with a width of $2\sigma = 0.2$ eV.

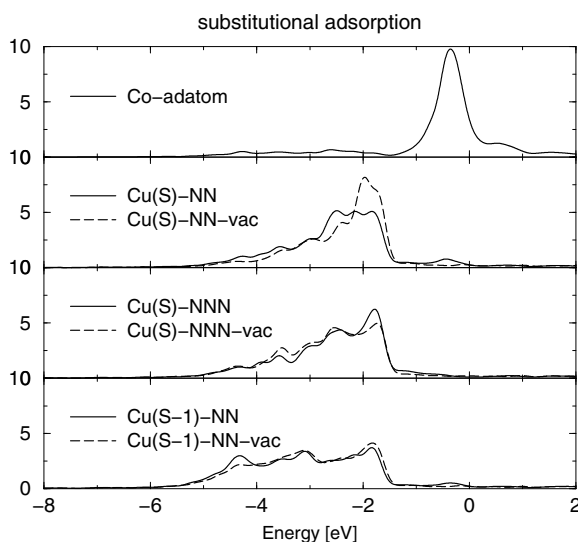


Figure 4.4: The muffin tin contributions to the total density of states of the Co atom and the neighboring Cu-atoms in Cu(001)- $p(2 \times 2)$ -Co-sub (solid line) and of the corresponding Cu atoms in a $p(2 \times 2)$ vacancy structure (dashed line). The nearest and next nearest neighbors of the Co atom in the surface layer are labeled as Cu(S)-NN and Cu(S)-NNN, respectively, while the nearest neighbor from the subsurface layer is Cu(S-1)-NN. The calculated DOS were broadened by a Gaussian with a width of $2\sigma = 0.2$ eV.

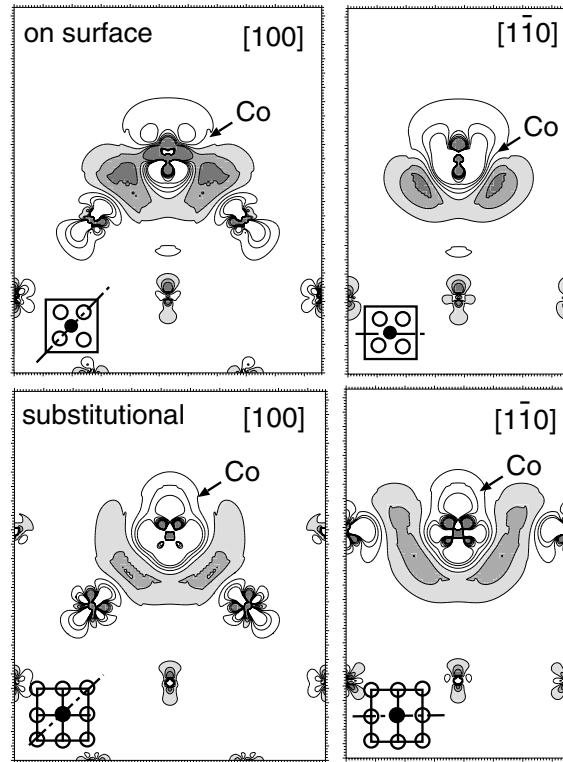


Figure 4.5: Electron density difference, $n(\mathbf{r}) - n^{\text{ref}}(\mathbf{r}) - n^{\text{Co-p}(2 \times 2)}(\mathbf{r})$, of a $p(2 \times 2)$ -structure with Co adatom at on-surface (upper panel) or substitutional (lower panel) adsorption sites. $n(\mathbf{r})$, $n^{\text{ref}}(\mathbf{r})$ and $n^{\text{Co-p}(2 \times 2)}(\mathbf{r})$ are the electron densities of the adsorbate system, the reference system (clean Cu(001) or vacancy structure) and a free Co- (2×2) monolayer. The grey regions correspond to regions of electron-density increase while regions of electron-density depletion are marked only by contour lines. The contour lines start at $\pm 2 \times 10^{-3} \text{ bohr}^{-3}$ and have a separation of $4 \times 10^{-3} \text{ bohr}^{-3}$. The plots show a cross-section along the (100)- and $(1\bar{1}0)$ -plane. The top view of the surface unit cell with the direction of the cut is given schematically in the left corner of each picture.

of the Co d -band and a relative shift towards lower energies and a lower DOS at the Fermi level. This effect is particularly distinct for the substitutional site and can be directly related to the stronger bonding at the substitutional geometry.

The adsorption of cobalt on the surface invokes significant changes in the DOS of the substrate surface. The MT-contributions of the substrate atoms to the total DOS before and after adsorption, are plotted in Fig. 4.3 and Fig. 4.4 with a solid and dashed line, respectively. In the case of on-surface adsorption, Fig. 4.3, the DOS of copper in the substrate surface layer is reduced at the top of the d -band and the d -band is slightly broadened. Additionally we observe an

enhancement at the position of the Co d -band near the Fermi level which indicates the hybridization of the substrate sp -bands with the adsorbate d -band. For the substitutional adsorption, Fig. 4.4, the strongest changes occur for the nearest neighbor in the surface layer (Cu(S)-NN), *i.e.* filling the vacancy with a Co adatom leads to a broadening of the Cu d -band and a substantial reduction of DOS at the top of the d -band resulting in a shift of the d -band center of mass towards lower energies. The adsorption induced changes in the next nearest neighbors in the surface layer (Cu(S)-NNN) and the nearest neighbors in the subsurface layer (Cu(S-1)-NN) are significantly smaller and for Cu(S)-NNN have even the opposite character.

Additional insight into the bonding nature can be gained from Fig. 4.5 showing the change in the electron density upon adsorption. For the on-surface adsorption $\Delta n(\mathbf{r})$ is given with respect to the clean Cu(001)-surface and a free standing Co- $p(2 \times 2)$ -monolayer and for the substitutional adsorption with respect to a vacancy structure and a free standing $p(2 \times 2)$ -Co-monolayer with Co- and Cu atoms at the corresponding positions as in the adsorbate systems. The electron-density plots show that the perturbation caused by the adsorption does not reach very far in the substrate and is essentially restricted to the neighboring Cu atoms. In both cases charge is transferred from the vacuum side of the adsorbate towards the interstitial region with a pronounced accumulation of electron charge between the Co adatom and its Cu neighbors. For the on-surface adsorption the bonds are formed between the adsorbate and the Cu atoms of the top Cu layer while for the substitutional adsorption the bonds are formed both with the Cu atoms of the top Cu layer and the Cu neighbors from the subsurface layer. Due to the electron charge accumulation on the line between the adatom and Cu neighbors the bonding mechanism shows a directional covalent character.

4.4 Dependence of E^{ad} on coverage

The above discussion deals with the adsorption of 0.25 monolayers of Co on Cu(001). We also studied the interplay of the adatom-adatom versus adatom-substrate interaction for different Co coverages. In Fig. 4.6 the adsorption energy E^{ad} is plotted as a function of the adsorbate coverage. For all coverages the adsorption energy for the substitutional site is higher than the one for fcc hollow site and thus the former is always more favorable than the latter.

A further aspect that needs to be considered is whether the surface alloys formed through substitutional adsorption are stable against separation into compact islands. In the limit of 1ML the two adsorbate configurations coincide. The

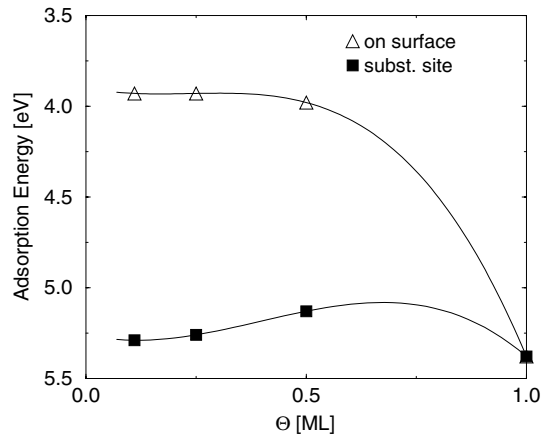


Figure 4.6: The adsorption energy E^{ad} in eV per Co atom as a function of coverage for a nonmagnetic Co adatom on a fcc hollow (triangles up) and a substitutional (filled squares) site. In the limit of $\Theta = 1.0$ ML the adsorption energy of a nonmagnetic Co adlayer on Cu(001) was used.

adsorption energy of a sufficiently large compact island, where the contribution of the side walls is small, can be expressed by the one of the $p(1 \times 1)$ cobalt monolayer on Cu(001), which equals 5.38 eV. Figure 4.6 shows that the substitutional adsorption always competes with the formation of compact islands. However, for $\Theta \leq 0.25$ ML the probability that Co adatoms meet and form islands is low. In this case, single cobalt adatoms prefer to adsorb substitutionally and achieve a higher coordination of Cu atoms (eight compared to four for the on-surface adsorption). However, Co-Co bonds are stronger than Co-Cu bonds. Therefore at higher coverages which corresponds to shorter adsorbate-adsorbate distances the interaction between the localized d -orbitals becomes important and a close packed Co structure will be attained. In agreement with previous theoretical studies [119] a $c(2 \times 2)$ -surface alloy of cobalt on Cu(001) is unstable against phase separation. Fassbender *et al.* [13] and Chambliss *et al.* [39] proposed recently that the surface intermixing of Co or Fe on Cu(001) is a result of the difference of the surface free energies of the contributing materials. However, our calculations show that the difference of surface energies is rather the driving force towards the thermodynamic equilibrium configuration, a compact bilayer thick Co island capped by copper [129]. The substitutional adsorption represents an alternative only for low coverages when the Co adatoms whose mobility is restricted by high diffusion barriers (s. Chapter 5) do not feel the presence of other Co atoms.

The adsorption of alkali-metal atoms (e.g. Na) on Al(001) and Al(111) [73, 115] was the first example of surface alloying of immiscible materials. However, con-

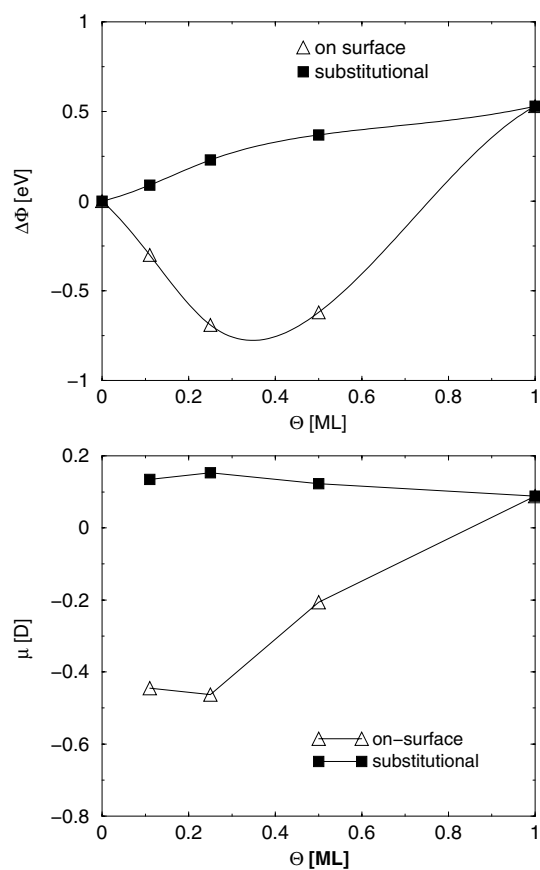


Figure 4.7: The change of work function $\Delta\phi$ in eV compared to the clean Cu(001)-surface and the induced dipole moment μ in Debye as a function of coverage for a Co adatom on a fcc hollow (triangles up) and a substitutional (filled squares) site. In the limit of $\Theta = 1.0$ ML $\Delta\phi$ and μ of a Co adlayer on Cu(001) was used.

cerning the coverage dependence, the situation for Na on Al(001) is the opposite compared to Co on Cu(001): Substitutional adsorption does not occur for single adatoms, but only after the coverage has reached a critical value. In this case intermixing is driven by the strong electrostatic repulsion between the adatoms where the adsorption at substitutional sites enables a better screening and thus reduces the electrostatic repulsion. In the case of Co on Cu(001) the changes of the work function, $\Delta\Phi$, with respect to the work function of the bare surface, $\Phi_{\text{Cu}(001)} = 4.78$ eV, are much lower than for alkali metal adsorbates. Consequently the induced dipole moments, which are given by the Helmholtz equation, $\mu \propto \frac{\Delta\Phi}{\Theta}$, are small and the electrostatic interactions do not play a significant role for the stability of a system.

However, one can observe several interesting trends in Fig. 4.7, where $\Delta\Phi$

and μ are plotted as a function of coverage. For the on-surface adsorption $\Delta\Phi$ is negative, and for the substitutional adsorption $\Delta\Phi$ is positive. Since Co and Cu have almost the same electronegativity (1.88 and 1.90, respectively) the change of the work function is a geometric effect. In the case of on-surface adsorption the result is in line with the observations for homoepitaxial metallic systems where surface roughness leads to a reduction of the work function [108, 123] as a consequence of the so called Smoluchowsky-smoothing. Analogous to findings for Na on Al(001) [124], for the on-surface adsorption $\Delta\Phi$ exhibits a nonmonotonic behavior as a function of coverage. At shorter distances, i.e. at higher coverages (e.g. above 0.5 ML) the effect of *depolarization* is responsible for the decrease of $\Delta\Phi$, namely the repulsive electrostatic interaction is reduced by a decrease of the dipole moment.

In contrast to the on-surface adsorption where the adatom lies above the surface for the substitutional adsorption the adatom relaxes inwards (-4%) with respect to the surface substrate layer and therefore the induced dipole moment has the opposite sign. Due to the better screening of the surrounding substrate atoms, $\Delta\Phi$ and μ show a much weaker dependence on coverage. Note that Fig. 4.7 assumes that the Co coverage is always homogeneously distributed. In reality, in particular for the on-surface adsorption at $\Theta \geq 0.30$ ML we expect a phase transition towards compact Co islands. Thus, the work function will abruptly change to 5.31 eV for a $p(1 \times 1)$ Co structure.

Finally we would like to mention, that intermixing for low coverages goes together with surface strain relief. Pseudomorphic thin films of Co on Cu(001) with a thickness of 1-2 ML are subject to tensile strain due to the lattice mismatch of the two materials (for details see Section 3.1). In the dilute limit the incorporation of single Co atoms in the substrate layer might represent a more effective mechanism with respect to surface strain relief compared to the formation of compact on-surface islands with a reduced in-plane lattice constant [125]. As a consequence the Co adatoms are expected to be homogeneously distributed on the surface and an intermixed surface layer is likely to occur for $\Theta \leq 0.25$ ML.

4.5 Influence of magnetism on the adsorption energy

Since the ground state of cobalt is ferromagnetic, we investigate in this Section the influence of magnetism on the stability of the studied systems. The adsorption energies of nonmagnetic and ferromagnetic adsorbate systems as a function of coverage are plotted in Fig. 4.8. We see that the ferromagnetic solutions are always more favorable than the nonmagnetic. The energy gain due to

spin-polarization is somewhat stronger in the case of on-surface adsorption compared to substitutional adsorption, *e.g.* for $\Theta = 0.25$ ML $\Delta E_{\text{on-surface}}^{\text{sp}} = 0.27$ eV and $\Delta E_{\text{subst.}}^{\text{sp}} = 0.20$ eV. This effect can be explained by the lower coordination of the adsorbate on the surface which results in a stronger localization of the Co $3d$ -states and a larger gain in magnetic energy. However, the energy difference of the two investigated adsorption geometries, on-surface and substitutional, changes by less than 0.1 eV for a $p(2 \times 2)$ -unit cell if spin-polarization is considered: $\Delta E_{\text{NM}}^{\text{ad}} = 1.32$ eV for a nonmagnetic calculation compared to $\Delta E_{\text{FM}}^{\text{ad}} = 1.24$ eV for a ferromagnetic calculation. We note, that in this Chapter we are interested in adsorption energy *changes* and *relative* stability of different adsorbate geometries. While quantitatively the results are affected by magnetism, we find that both the magnetic and nonmagnetic descriptions give the same qualitative trends, namely the substitutional adsorption is lower in energy than the on-surface, but with growing coverage gets less favorable compared to the formation of compact cobalt islands.

Table 4.1 contains the magnetic moments of the cobalt adatom in the two adsorbate geometries for different coverages. For the on-surface adsorption the magnetic moment is $0.24 \mu_{\text{B}}$ higher than for the substitutional geometry. This is a consequence of the well-known effect that a lower coordination leads to narrower d -bands and a higher density of states at the Fermi level which according to the Stoner model enhances the tendency towards magnetism. The same effect was observed from KKR-calculations of the magnetic moments of isolated $3d$ impurities adsorbed on the Cu(001)-surface or in the substrate layer [126]. The

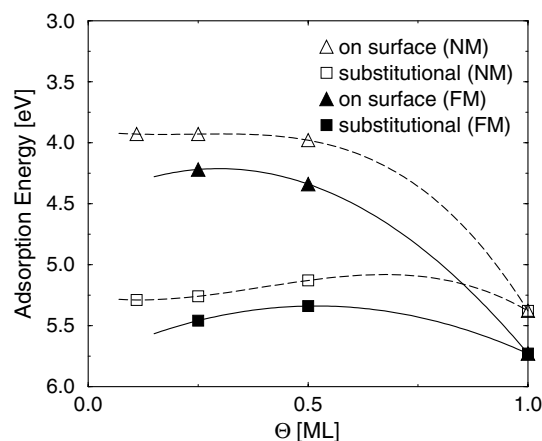


Figure 4.8: The adsorption energy E^{ad} of a Co adatom on a fcc hollow (triangles up) and a substitutional (squares) site as a function of coverage for nonmagnetic (empty symbols) and ferromagnetic (filled symbols) systems. In the limit of $\Theta = 1.0$ ML the adsorption energy of a Co adlayer on Cu(001) was used.

Θ [ML]	M [μ_B]	
	on-surface	substitutional
0.25	1.62	1.38
0.50	1.68	1.44
1.0	1.71	1.71

Table 4.1: Magnetic moments of cobalt in the ferromagnetic systems in [μ_B] for different coverages in the on-surface and substitutional adsorbate geometry. For $\Theta = 1$ ML the magnetic moment of a $p(1 \times 1)$ cobalt monolayer on Cu(001) was considered.

slightly higher magnetic moments in Ref. [126] compared to our study are due to structural differences: *i.e.* Lang *et al.* used the experimental lattice constant of copper (3.61 Å) and neglected relaxations. Our calculations show that changing the lateral parameter from the theoretical LDA-value for bulk Cu (3.55 Å) to the theoretical GGA-value (3.65 Å) leads to an increase of the magnetic moment of $0.2 \mu_B$. The strong relaxation of the Co adatom, adsorbed at a hollow site, towards the substrate layer (-16%) has a noticeable influence on the magnetic moment.

The magnetic moment grows slightly with increasing coverage for both adsorbate geometries which indicates that at shorter distances the magnetic coupling between the Co adatoms gains importance. The increasing magnetic moment comes along with a larger exchange splitting. This is indicated in Fig. 4.9 by the fact that the separation between the centers of mass of the minority and majority

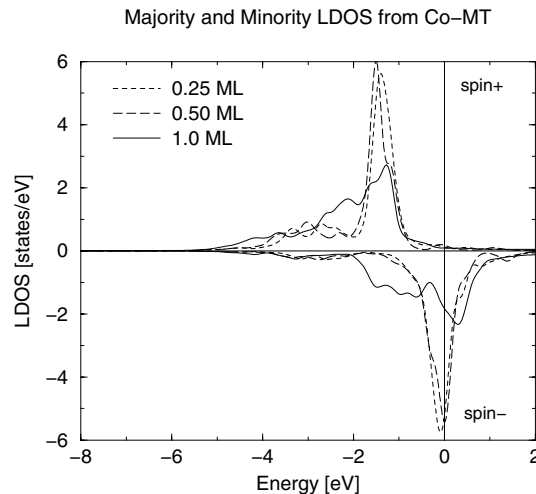


Figure 4.9: s , p , and d contributions to the total density of states from the Co muffin tin for 0.25 ML (dotted), 0.50 ML (dashed), and 1.0 ML (solid line) Co adsorbed on-surface on Cu(001). Positive LDOS indicates the majority states, negative LDOS the minority states.

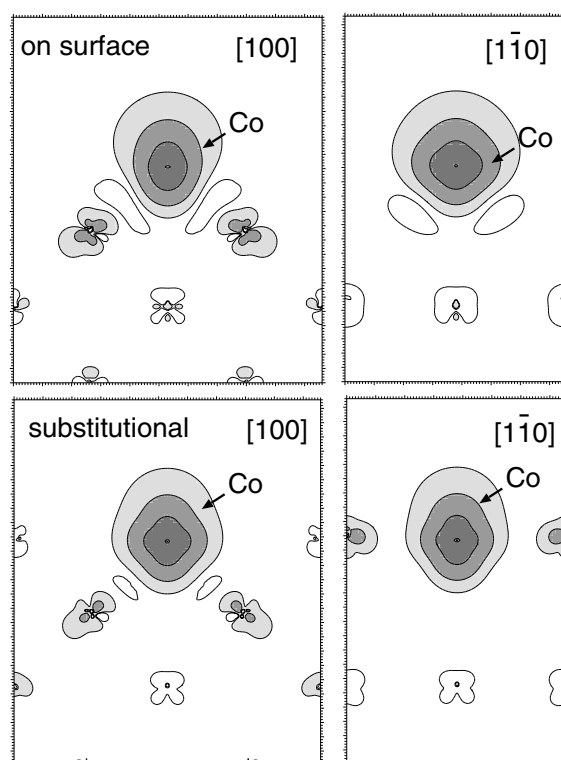


Figure 4.10: Spin-density plots of a $p(2 \times 2)$ -structure with Co adatom at on-surface (upper panel) or substitutional (lower panel) adsorption sites. The grey regions correspond to regions of positive spin-density while regions of negative spin-density are marked only by contour lines. The contour lines start at $\pm 10^{-3} e/\text{bohr}^3$ and have a separation of a factor of 10. The plots show a cross-section along the (100)- and $(1\bar{1}0)$ -plane.

Co bands increases with coverage.

Insight into the spacial distribution of the spin-density in both adsorbate geometries is given in Fig. 4.10 where cross-sections of the spin-density along the (100)- and $(1\bar{1}0)$ -plane for a Co coverage of 0.25 ML are plotted. For the on-surface geometry the spin-density at the Co adatom is more expanded in the vacuum region. The spin-polarization induced in the substrate has a weak oscillatory character, *i.e.* nearest neighbors couple ferromagnetically to the Co adatom, while next nearest neighbors couple antiferromagnetically with an absolute value of the magnetic moment in the MT-sphere of approximately $0.10 \mu_B$. We note that for Cu(001)- $p(2 \times 2)$ -Co-sub the induced polarization is stronger for the nearest neighbor from the surface layer, $0.10 \mu_B$, while the magnetic moment of the nearest neighbor in the subsurface layer is negligible, $0.01 \mu_B$. A negative net polarization of the interstitial region of the order of $0.10 \mu_B$ is found for the substitutional geometries and the $p(1 \times 1)$ -monolayer. This polarization is due mainly to the s

and p states and in the limit of 1ML Co/Cu(001) is in line with a previous DFT-result [87]. On the other hand, for the on-surface adsorption of submonolayer coverages (0.25 and 0.50 ML) the value is positive which can be attributed to the stronger expansion of the spin-density of Co in the vacuum region.

4.6 Nucleation potential of substituted Co atoms

The above results suggest to interpret the indentations in the STM images (see Fig. 4.1) as atomically resolved single Co atoms incorporated in the substrate surface layer. Due to the substitutional adsorption at low coverages we have an unexpected situation on the surface: some cobalt atoms are incorporated in the substrate layer and there are cobalt as well as copper adatoms diffusing on the surface. The consequences of this situation on the growth behavior were studied with STM comparing island size distributions of 0.11 ML Co deposited on the clean Cu(001) substrate at identical rates (0.2 ML/min) for two different temperatures, 295 K and 415 K (Fig. 4.11). According to the traditional view of nucleation as a result of binary collisions [33] a Poisson-like island size distribution with a peak close to the mean island size would be expected. Instead, the size distributions in Fig. 4.11 exhibit a maximum at very small island sizes and a decrease with growing island size. Additionally, at 415 K a second maximum appears at larger sizes. Fassbender *et al.* [13] note a similar observation: a broad island size distribution yet for higher coverages (0.6 ML) at 330 K. The island densities obtained from the two images a) and b) in Fig. 4.11 are $n_x = 1.64 \cdot 10^{-3}$ and $n_x = 2.23 \cdot 10^{-3}$ islands/surface unit cell, respectively. The deposition of Co at 415 K results in a higher island density compared to the deposition at room temperature, which is at variance with the classical scenario where $n_x \propto \left(\frac{F}{D}\right)^p$, F being the deposition rate, $D = D_0 e^{\left(\frac{-E_d}{k_B T}\right)}$ the diffusion constant, and p the critical exponent. Additionally Fassbender *et al.* [13] found that the island density does not saturate before coalescence sets in. The disagreement between experimental findings and predictions from standard nucleation theory implies that substitutional adsorption has a substantial influence on island formation.

Recently, atomic exchange was proposed as a mechanism for creation of pinning sites their influence on island density and island size distributions was studied using mean-field rate equations and Monte-Carlo simulations. [39, 40, 113]. In this Section we investigate quantitatively the role of the incorporated cobalt atoms as nucleation centers.

The systems studied include Co and Cu atoms at hollow sites on the clean Cu(001) and the adsorbate system with (3×3) substitutional Co atoms. The

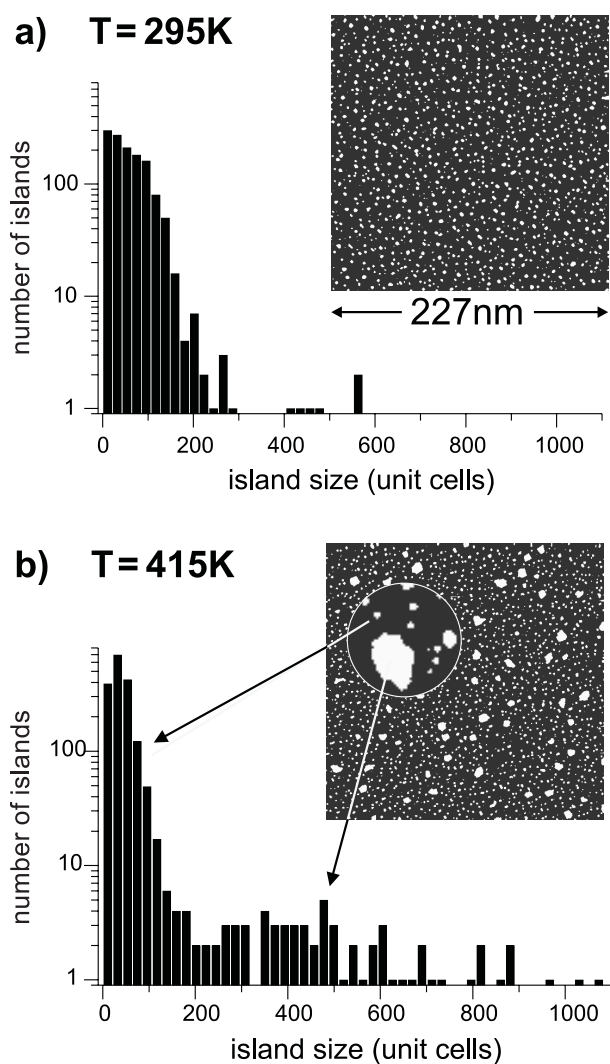


Figure 4.11: STM images and their island size distributions of 0.11 ML Co deposited on Cu(001) with identical deposition rates (0.2ML/min) at a) 295 K and b) 415 K [17]. The *bimodal* growth mode is clearly visible in b). As is indicated by the arrows, large islands correspond to the broad maximum at about 400 surface unit cells, whereas the sizes of the small islands are concentrated at very low values. The circle in the STM image in b) represents a magnification.

isolated adatom on the clean Cu(001)-surface is marked as “far”. Depending on the position with respect to the substituted Co atom there are two different adsorption sites on the Cu(001)-(3 × 3)-Co-sub surface: one where the adatom (Co or Cu) is the nearest neighbor (Fig. 4.12a) and another where it is $1.5 a_{\text{Cu}}^0$ away from the substituted Co atom (Fig. 4.12b).

The height of the adsorbate as well as of the substitutional Co in the different

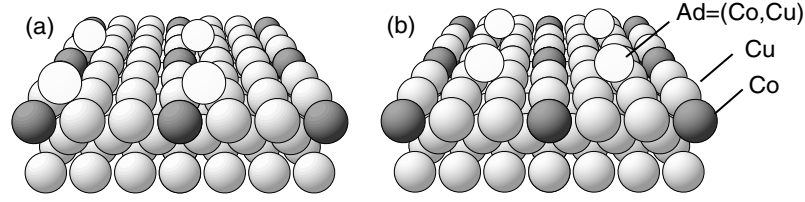


Figure 4.12: Structures of (3×3) substitutional Co on Cu(001) with additional adatoms (Co or Cu) at an on-surface hollow site as (a) nearest neighbor or (b) $1.5 a_{\text{Cu}}^0$ away from the substituted Co atom.

configurations presented in Fig 4.12 was optimized. We find that the Cu adatom relaxes 10% inwards in both configurations, Figs. 4.12a and 4.12b, while Co relaxes by -17% if it is $1.5 a_{\text{Cu}}^0$ away from the substituted Co atom (Fig. 4.12b) and by -19% as a nearest neighbor to it (Fig. 4.12a). The height of the Co atom does not change noticeably except for the system where the Co adatom is a nearest neighbor to the incorporated Co. In this case the substitutional Co relaxes by only 3.6% inwards. Additionally the lateral relaxation for the systems in Fig. 4.12a was calculated. The most distinct feature is the contraction of the distance between the adatom and the substitutional Co, whereby the effect is much stronger in case of a Co adatom, 2.16 Å, than for Cu, 2.38 Å.

The adsorption energy of the systems shown in Fig. 4.12 is calculated analogous to E^{ad} on the clean Cu(001) surface (Eq. 4.1) where instead of $E^{\text{Cu}(001)}$ the total energy of the Co substituted (3×3) -Cu(001) surface is considered. Additionally, we estimated the adsorption energies for Co and Cu adatoms at a kink site of a Cu step or island. For a Cu adatom this energy equals the cohesive energy. The kink-site energy of a Co adatom was obtained by a least squares fit of the energy as a function of the local coordination number. In a bond-cutting model [108, 109] the energy of the system can be expressed as a sum of the contributions of the individual atoms I , $E = \sum_I E_I$, where E_I is described by a square root dependence on the coordination number Z_I of atom I : $E_I = E_I^0 + A_I \sqrt{Z_I} + B_I Z_I$. Here, E_I^0 is the

Adsorption position	$\Delta E_{\text{Cu}}^{\text{ad}}$ [eV]	$\Delta E_{\text{Co}}^{\text{ad}}$ [eV]
$1.5 a_{\text{Cu}}^0$	-0.03	0.02
nearest neighbor	0.22	0.55
kink site at a Cu island	0.82	1.25

Table 4.2: Calculated adsorption energy changes of Co and Cu adatoms at a fcc hollow site on the intermixed Cu(001)- (3×3) -Co-sub surface with respect to E^{ad} for the clean Cu(001) surface.

energy of a free atom with $I = (\text{Cu}, \text{Co})$. The energies of Co and Cu bulk, as well as the clean (001)-surfaces and the adsorbate systems calculated in a (3×3) -unit cell were considered in the fit [128].

The adsorption energies are listed in Tab. 4.2 as energy changes with respect to the ones of the isolated adatoms (“far”) on Cu(001) ($E_{\text{Cu-far}}^{\text{ad}} = 3.68$ eV, $E_{\text{Co-far}}^{\text{ad}} = 3.95$ eV). The first important fact is that the Co adatom is always bound stronger on the surface than the Cu adatom due to a stronger $d-d$ and $d-sp$ hybridization. The higher adsorption energy of Co may be considered as an implication that Co is less mobile than Cu. [127]

In order to establish the relation between energetic trends and the underlying electronic effects we have plotted the adsorption induced changes of the electron density for Cu (Fig. 4.13a-c) and Co (Fig. 4.13d-f) on the clean Cu(001) surface and on the Co substituted $p(3 \times 3)$ -Cu(001) surface. Analogous to the electron density plots in Fig. 4.5, in Figs. 4.13a and d $\Delta n(\mathbf{r})$ is given with respect to the clean Cu(001) surface and a free standing (Cu or Co) $p(3 \times 3)$ -adsorbate layer while in Figs. 4.13b,c,e, and f the reference system is Cu(001)- $p(3 \times 3)$ -Co-sub and a free standing (Cu or Co) $p(3 \times 3)$ -adsorbate layer.

Figure 4.13d and the upper panel in Figure 4.5 show the on-surface adsorption of cobalt on Cu(001) for two different coverages, 0.11 ML and 0.25 ML. The adsorption induced features of $n(\mathbf{r})$ bear a strong resemblance, *i.e.* at distances bigger than $2a_{\text{Cu}}^0$ the interaction between the adsorbates is negligible which is also reflected in the adsorption energies, e.g. $E_{p(3 \times 3)}^{\text{ad}} = 3.95$ eV and $E_{p(2 \times 2)}^{\text{ad}} = 3.94$ eV.

Figures 4.13a and 4.13b and Figures 4.13d and 4.13e which represent the electronic effects for an adatom (Cu or Co) on the clean Cu(001) surface and on the substituted $p(3 \times 3)$ surface $1.5a_{\text{Cu}}^0$ away from the embedded Co atom, respectively, also look very similar. Indeed, the corresponding adsorption energies are close, which confirms the previous statement that the adatoms are practically not sensitive to the environment going beyond second nearest neighbors.

Comparing the two adsorption sites on the substituted surface, *i.e.* adatom as nearest and third neighbor to a substitutional Co, we conclude that the incorporated Co atoms indeed act as pinning centers both for Co and Cu atoms, the effect being stronger for Co (0.53 eV) than for Cu (0.25 eV). An evidence for this is given again in Fig. 4.13. In the case where the adatom adsorbs as a nearest neighbor of the incorporated Co (Figs. 4.13c and f, respectively) the changes of electron density are much more dramatic than when it adsorbs $1.5a_{\text{Cu}}^0$ away from it (Figs. 4.13b and e) and show a substantial asymmetry, *i.e.* a stronger electron charge redistribution takes place on the line connecting the adsorbate with the embedded Co. A depletion of the electron density occurs on the vacuum side of the adsorbate while $\Delta n(\mathbf{r})$ increases substantially between the adsorbate and the

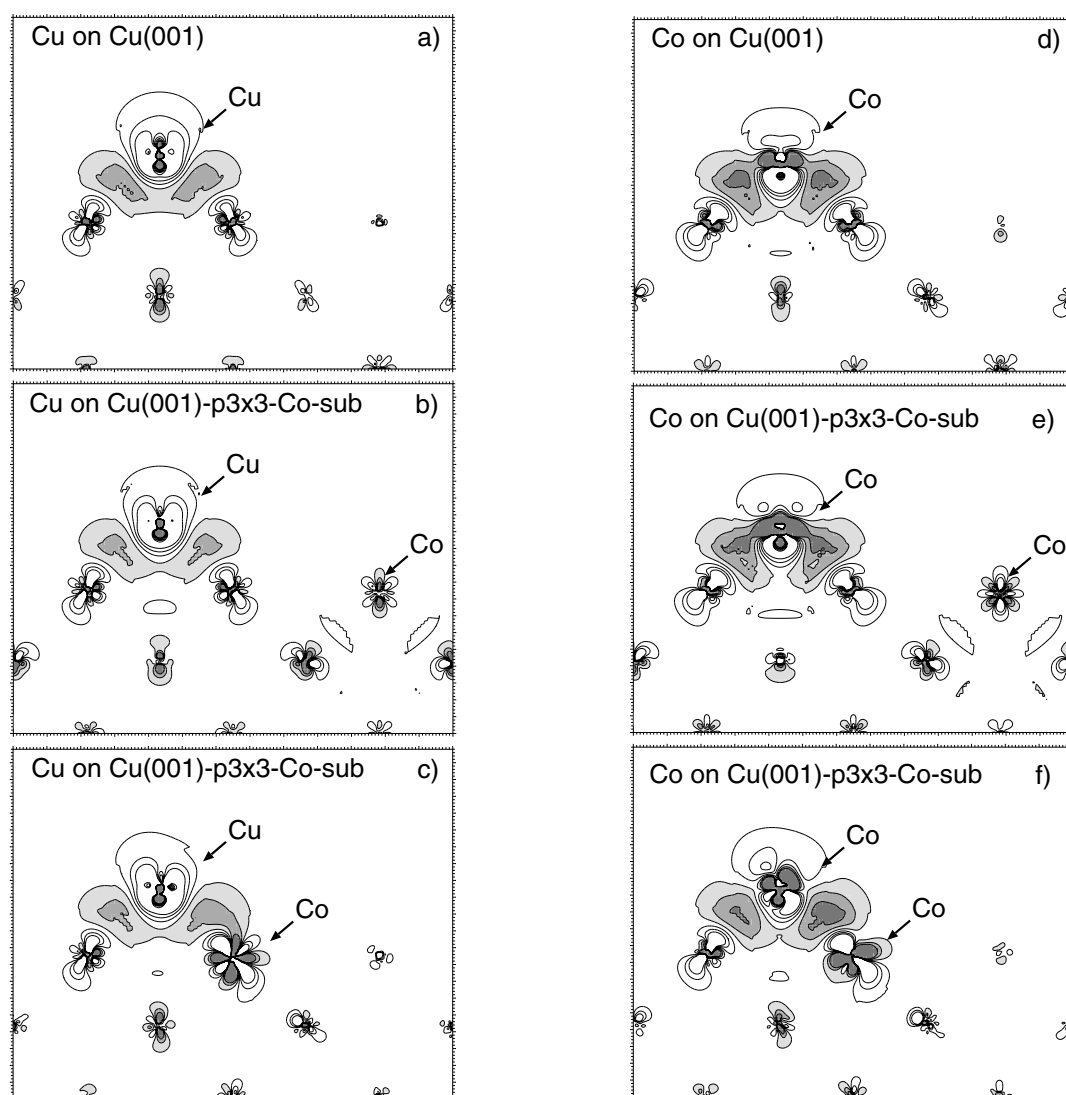


Figure 4.13: Change of electron density upon adsorption of 0.11 ML of Cu or Co on the clean Cu(001) surface (panels a and d, respectively) and the system with $p(3 \times 3)$ substitutional Cu or Co atoms at an on-surface hollow site $1.5a_{\text{Cu}}^0$ away from the substituted Co atom (panels b and e, respectively) and as a nearest neighbor of it (panels c and f, respectively). The adsorbate induced changes are given with respect to the clean Cu(001) surface (a and d) and Cu(0001)- $p(3 \times 3)$ -sub and a free Cu- $p(3 \times 3)$ monolayer (b,c,e and f). The grey regions correspond to regions of electron-density increase while regions of electron-density depletion are marked only by contour lines. The contour lines start at $\pm 2 \times 10^{-3} \text{bohr}^{-3}$ and have a separation of $4 \times 10^{-3} \text{bohr}^{-3}$. The plots show a cross-section along the (100)-plane.

substituted Co atom. We also note that the electronic changes are clearly stronger for the Co adatom than for the Cu adatom which is in line with the higher adsorption energy of the former compared to the latter and also with the stronger reduction of the Co-Co-bond compared to the Cu-Co-bond mentioned above.

The consequences of pinning on surface morphology are discussed in the following. The diffusion barrier of Cu on the clean Cu(001)-surface is approximately 0.5 eV (cf. Ref. [111] and Chapter 5). Assuming that the energy at the transition state (bridge site) remains unchanged, the barrier for hopping diffusion would be enhanced by 0.25 eV in the vicinity of the incorporated Co atom. On the other hand, as will be shown in Chapter 5 the diffusion barrier for hopping and exchange of Co is much higher. Therefore, at temperatures at which exchange of Co is already activated Cu would have enough energy to overcome the attractive potential of the pinning center and diffuse away from the Co atom.

On the other hand, the situation for Co is different. An increase of 0.53 eV of the already high diffusion barrier (cf. Chapter 5) will bind the Co adatom quite strongly next to the substituted Co. Therefore pinning is particularly effective for Co adatoms. Another favorable adsorption site both for Co and Cu adatoms is a kink site at a Cu island.

The arguments presented above suggest strongly that although Co is being deposited, in the very initial stage of growth the first stable islands are formed essentially by Cu adatoms. The Co atoms incorporated in the substrate layer constitute centers for further island nucleation and thus the critical island size is zero, *i.e.* the monomer constitutes a stable nucleus. Additional Co adatoms diffusing on the surface will be pinned at the nucleation centers. Therefore we expect a high island density of Co islands and Co decoration of the Cu islands at elevated temperatures.

These theoretical predictions were indeed confirmed in a CO-titration experiment. AES test measurements of CO-exposed surfaces at $T = 295$ K clearly showed strong CO adsorption on a Co(001) surface [5 ML grown on Cu(001)] and negligible adsorption on the pure Cu(001) surface. It is therefore possible to correlate CO adsorption induced features in the STM images with Co sites at the surface. This direct identification has clear advantages compared to identification via bias voltage dependent contrast inversion used in Ref. [13]. The latter is based on the electronic structure of tip and sample and thus does not permit an unambiguous interpretation. Fig. 4.14 shows an STM image of 0.11 ML Co deposited at $T = 415$ K and subsequently exposed to 20 Langmuir CO at $T = 295$ K. The bright clouds are observed only after the exposure and are attributed to the adsorbed CO molecules. The small islands are nearly completely covered with CO while on the large islands CO is adsorbed only at the edges, proving that the

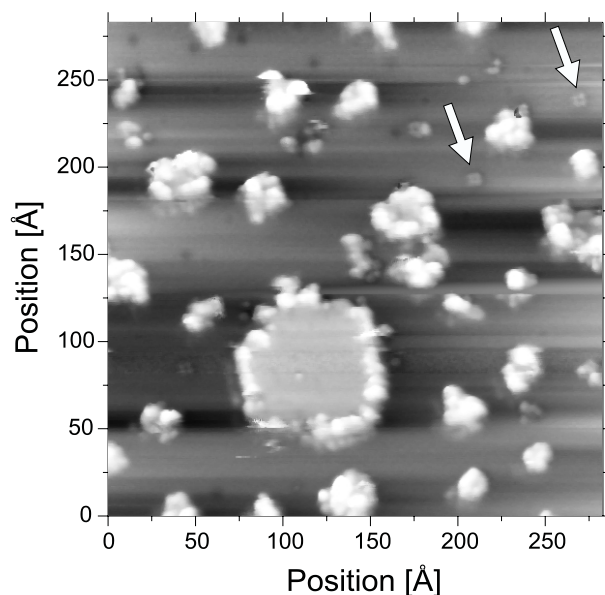


Figure 4.14: STM image ($U_{tip} = 3.5$ V, $I = 0.4$ nA) of 0.11 ML Co/Cu(001), deposited at 415 K and afterwards exposed to about 20 Langmuir CO [17]. Adsorption induced features occur on the small islands, on the edges of the large islands and at atomic-size indentations (white arrows).

small islands consist mainly of Co and the large ones of Cu with Co decoration at the edges.

Indeed, a close inspection of the STM image for 415 K in Fig. 4.11b and the corresponding island size distribution reveals *two* different kinds of islands, which can be identified by their mean sizes. In addition to a large amount of small islands a few much larger islands are represented in the island size distribution by a broad maximum at an island area of about 400 surface unit cells. The significantly larger separation between the large islands compared to the separation between the small ones correlates with the higher mobility of the Cu atoms on the surface – and supports the above quantitative evidence that the large islands consist mainly of Cu. Generally, two microscopic mechanisms initiate the *bimodal* behavior: exchange mediated nucleation (Co pinning centers) and growth of the Cu islands. The features of the bimodal growth mode are particularly distinct at $T=415$ K because the processes leading to it are thermally activated as discussed above.

4.7 Summary

In summary, we performed DFT-calculations for the adsorption of Co on Cu(001) for coverages between 0 and 1 ML. The results show that in the initial stage of growth, while still unaware of the presence of other Co adatoms, Co prefers to assume a high coordination of substrate atoms in a substitutional site as opposed to adsorption on a fourfold hollow site on the surface. However with growing coverage the exchange processes become less likely compared to the formation of compact Co clusters. Although the ferromagnetic solutions are always lower in energy, the energetic trends remain unaffected by magnetism. The polarization induced by the magnetic Co adatom in the substrate has an oscillatory character both in vertical and lateral direction and indicates that the magnetic coupling of the adatoms is mediated by the substrate.

Due to the substitutional adsorption in the initial stages of growth we have an unexpected situation on the surface: Besides the embedded Co atoms, there are Co as well as Cu adatoms diffusing on the surface. The DFT calculations show that the incorporated Co atoms act as *nucleation centers* for Co and Cu adatoms on the surface, the effect being stronger for Co adatoms.

In a recent DFT-study applying the KKR method Nonas *et al.* [118] report of a strong tendency towards substitutional adsorption also for *3d* transition-metal adatoms on Fe(001). However, in contrast to Co on Cu(001), they found that the pair complex (Fig. 4.12a) is unstable and the Fe adatom would prefer to diffuse away from the incorporated *3d* impurity. This is partly due to the magnetic coupling of the *3d*-impurity or Fe adatom to the magnetic substrate, partly, as in the case of a Cu impurity, can be understood in a simple bond-cutting model: Fe-Fe bonds are stronger than Fe-Cu-bonds. Thus the system prefers to maximize the number of Fe-Fe bonds. In the case of Co on Cu(001) the situation is the opposite: Co-Co bonds are stronger than Co-Cu bonds, while the latter are stronger than Cu-Cu bonds. The effect of pinning at incorporated Co atoms is a consequence of this picture. Since this model holds also for other *3d*-elements on Cu(001) (or another noble metal substrate) the results for Co on Cu(001) should apply also for a broader class of transition metal elements on a noble metal substrate. In fact similar behavior was observed recently for Fe/Cu(001) [39], Fe/Au(001) [131] and Ni/Cu(001) [41].

4.8 Appendix

In order to investigate the importance of non-local exchange and correlation effects on the adsorption energies we performed calculations with the LDA [53]

Coverage	System	$E_{\text{LDA}}^{\text{ad}}$	$E_{\text{GGA}}^{\text{ad}}$
$\Theta = 0.25$ ML	Cu(001)- $p(2 \times 2)$ -Co	3.95	2.87
	Cu(001)- $p(2 \times 2)$ -Co-sub	5.26	3.98
$\Theta = 0.50$ ML	Cu(001)- $c(2 \times 2)$ -Co	3.98	2.86
	Cu(001)- $c(2 \times 2)$ -Co-sub	5.13	3.87
$\Theta = 1.00$	Cu(001)- $p(1 \times 1)$ -Co	5.38	4.08

Table 4.3: The adsorption energies $E_{\text{LDA}}^{\text{ad}}$ and $E_{\text{GGA}}^{\text{ad}}$ of the on-surface and substitutional adsorption geometry for different coverages calculated within LDA and GGA, respectively, are given in eV per adsorbate atom. The lateral parameter is set to the corresponding (LDA or GGA) equilibrium lattice constant of copper.

and with the GGA [54] for adsorbate systems with Co adatoms at on-surface and substitutional sites for different coverages. The lateral parameter was set to the lattice constants of copper obtained within the LDA and GGA approach, 3.55 Å and 3.65 Å, respectively. The results are given in Table 4.3.

The difference between $E_{\text{LDA}}^{\text{ad}}$ and $E_{\text{GGA}}^{\text{ad}}$ is of the order of 1 eV. This behavior has been already observed for other adsorbate systems [130]. The main reason is that while LDA overestimates cohesive energies a substantial improvement can be achieved within GGA. Especially in the description of the free Co atom needed as a reference system in Eq. 4.1 non-local exchange and correlation effects become important because the electron density gradient is large. However, E^{ad} is calculated per adsorbate atom thus the effects cancel partially out if we look at adsorption energy differences. For example, for $\Theta = 0.25$ ML the substitutional adsorbate geometry, Cu(001)- $p(2 \times 2)$ -Co-sub, is favored over the on-surface, Cu(001)- $p(2 \times 2)$ -Co, by 1.31 eV within LDA and by 1.11 eV within GGA. Thus, although the absolute values of the adsorption energy change the qualitative trends are the same within LDA and GGA.

Chapter 5

Adatom diffusion on the flat Cu(001)-surface

5.1 Introduction

Growing structures evolve under the influence of kinetics [34]. In order to understand and possibly control growth and the resulting surface morphology a detailed knowledge of the underlying microscopic processes is required. The latter include for example adatom diffusion on the flat surface, along steps, around island corners, and interlayer diffusion. These atomic processes are thermally activated and can be described by rates which depend exponentially on the difference in the Helmholtz free energy between the saddle point (transition state) and the minimum (binding site). Separating the entropy and energy terms the rate Γ is usually given in the form:

$$\Gamma = \Gamma_0 e^{-\frac{E_d}{k_B T}}. \quad (5.1)$$

where the prefactor $\Gamma_0 = \frac{k_B T}{h} e^{\frac{\Delta S_{vib}}{k_B}}$ is the attempt frequency with ΔS_{vib} being the difference in the vibrational entropy between initial and transition state, k_B the Boltzmann constant, h the Planck constant and T the temperature. In the framework of transition state theory (TST) [21] Γ_0 can be evaluated in the classical and harmonic approximation:

$$\Gamma_0 = \frac{\prod_{j=1}^{3N} \nu_j}{\prod_{j=1}^{3N-1} \nu_j^*}. \quad (5.2)$$

where ν_i and ν_i^* are the normal mode frequencies of the system with an adatom at the equilibrium site and at the saddle point, respectively and $3N$ is the number of degrees of freedom. In the denominator the summation goes over $3N - 1$ modes,

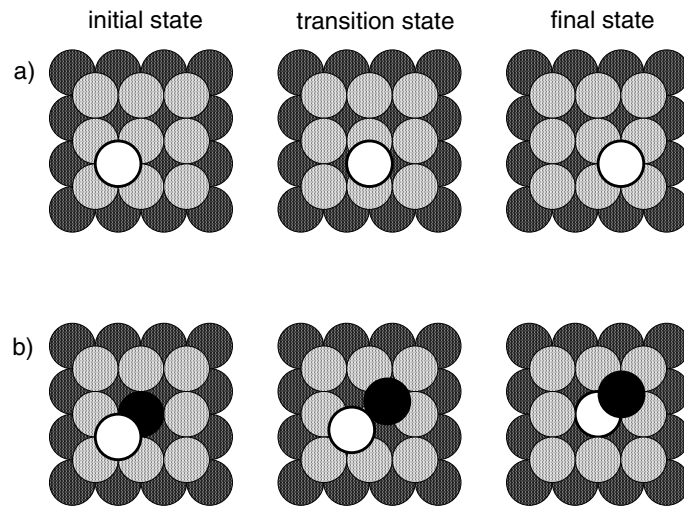


Figure 5.1: Top view of the initial (IS), transition (TS), and final (FS) state for diffusion a) via hopping and b) via exchange on a fcc (100) surface. The white circle corresponds to the adatom, the gray one to the substrate atoms and the substrate atom involved in the exchange diffusion is black.

because at the saddle point one of the modes describes the motion towards the final state and the corresponding ν_i^* is imaginary. Typical values of Γ_0 lie between $10^{12} - 10^{13} \text{ s}^{-1}$ as obtained from molecular dynamics based on semiempirical embedded atom method (MD-EAM) [111] or from DFT-calculations [132].

Besides the prefactor Γ_0 the rate is determined by the diffusion barrier E_d . Ground-state total-energy calculations give the so called *static* barrier which is the energy difference between the transition state and the equilibrium site neglecting the comparably small vibrational energy contributions as well as zero point vibrations. A recent publication on the homoepitaxy of Cu on Cu(001) by Boisvert and Lewis [111] showed that barriers obtained with the embedded atom method (EAM) at $T = 0 \text{ K}$ are a good approximation to the dynamical energy barriers, obtained with MD-EAM in the temperature range of 650 – 900 K. In order to obtain the barrier for a particular process, the transition state (TS) defined as the lowest energy saddle point has to be determined. For an adatom diffusing on the (001) surface via hopping between adsorption sites, the TS is the *bridge* site as shown in Fig. 5.1 a).

However, for concerted processes, where substrate as well as adsorbate atoms are directly involved, finding the transition state is not a trivial task. For example, diffusion may also occur by atomic exchange, shown schematically in Fig. 5.1 b) where the adatom replaces a substrate atom and the latter occupies an on-surface site in the final state. Diffusion via atomic exchange has been predicted

for the homoepitaxial growth of several fcc metals as Al on Al(001) [29] and Au on Au(001) [32] and observed for Pt(001) [133] and Ir(001) [134]. While in the case of homoepitaxy diffusion by atomic exchange implies that only half of the adsorption sites can be visited in a checkerboard $c(2 \times 2)$ -pattern, for heteroepitaxy the situation is much more complex. Namely, due to the exchange process the chemical composition of the substrate and the first layer is altered, there are not only adatoms of the deposited material but also of the substrate that are involved in the growth process. Therefore the number of relevant processes is substantially increased.

In this Chapter the above described diffusion mechanisms, hopping and atomic exchange, are investigated for Cu and Co adatoms on the flat Cu(001) surface. The results for the homoepitaxial case are compared to experimental and other theoretical studies. The diffusion barriers for the heteroepitaxial case of Co on Cu(001) for which to our knowledge there are no previous results in the literature are compared with the ones for Cu on Cu(001). Additionally, results of the structural optimization in the transition state, the bond lengths, and the accompanying electronic effects are presented. The hierarchy of the different diffusion processes is established on the basis of their onset temperature in Section 6.5.

5.2 Numerical details

The calculations of the diffusion barriers of Co and Cu adatoms on the clean Cu(001) surface were performed in a $p(3 \times 3)$ -unit cell with 16 k_{\parallel} -points in the Brillouin zone. A cutoff parameter for the basis set of 13.8 Ry was used for which a numerical accuracy of the formation (surface) energy of a 5 ML fcc Co(001)-slab at the lattice constant of copper better than 1.5 % (cf. Tab. 3.1 in Chapter 3) was obtained. The barriers were calculated both within the LDA and GGA.

5.3 Selfdiffusion on the Cu(001)-surface

5.3.1 Diffusion barriers

The diffusion barrier for hopping obtained within LDA (GGA) is 0.66 eV (0.49 eV) and for exchange diffusion 1.28 eV (1.02 eV). Hence, the diffusion barrier for exchange is about twice as high as the diffusion barrier for hopping on the surface. Therefore for selfdiffusion of Cu the exchange process is insignificant and mass transport proceeds via jumps between adjacent adsorption sites. Atomic exchange as a mechanism for surface diffusion has been discussed for

	method	hopping	exchange
theory			
this work	FP-LAPW-LDA (3 × 3), 5 layers	0.66	1.28
this work	FP-LAPW-GGA (3 × 3), 5 layers	0.49	1.02
Ref. [111]	PPW-LDA (2 × 2), 6 layers	0.65	1.18
Ref. [111]	PPW-LDA (3 × 3), 3 layers	0.75	1.03
Ref. [111]	PPW-GGA (3 × 3), 4 layers	0.52	0.96
Ref. [27]	EAM	0.43	0.22
Ref. [28]	EAM	0.45	
Ref. [135]	EAM	0.49	
Ref. [111]	EAM	0.50	0.73
experiment			
Ref. [137]	TEAS	0.40	
Ref. [138]	He-atom scattering	0.28 ± 0.06	
Ref. [139]	LEIS-TOF	0.39 ± 0.06	
Ref. [140]	HR-LEED	0.36 ± 0.03	

Table 5.1: Theoretical and experimental values for the diffusion barriers for hopping and exchange on the flat Cu(001) surface.

several fcc(001) surfaces. It was experimentally observed for Pt(001) [133] and Ir(001) [134] and predicted for Al on Al(001) by Feibelman [29]. However, while Au(001) is essentially another candidate for which exchange diffusion was predicted to be relevant it turns out this is not the case for the $3d$ and $4d$ fcc(001) metal surfaces [32]. As *ab initio* results show for Cu(001) ([111] and the present work) and Ag(001) [31, 32], hopping represents the dominant diffusion mechanism.

Applying GGA results in a significant reduction of the diffusion barriers, by 0.17 eV for hopping and by 0.26 eV for exchange. This effect is in line with previous *ab initio* results for Cu on Cu(001) [111] with the pseudopotential plane-wave method (PPW) where the GGA-value for hopping was 0.23 eV lower than the LDA-value while the one for exchange dropped by only 0.07 eV compared to the LDA-value (s. Table 5.1). Similar behavior was also observed by Yu and Scheffler [31]

in the case of Ag on Ag(001), where the diffusion barrier for hopping changed by 0.07 eV from 0.52 eV (LDA) to 0.45 eV (GGA) and the one for exchange by 0.20 eV from 0.93 eV (LDA) to 0.73 eV (GGA). While there is a good agreement between the diffusion barriers in the present study for a (3×3) -unit cell and in Ref. [111] for a (2×2) -unit cell, the value Boisvert and Lewis obtained in a (3×3) -unit cell in LDA is slightly higher for hopping diffusion but significantly lower (0.25 eV) for exchange diffusion. A possible reason for the discrepancy between the LDA barriers for exchange diffusion could be the different k_{\parallel} -point sampling: while we used 16 k_{\parallel} -points in the Brillouin zone, Boisvert and Lewis [111] used only four. As Stumpf and Scheffler [30] observed for Al, the k_{\parallel} -point sampling has a noticeable influence on the diffusion barrier, showing an oscillatory character with increasing k_{\parallel} -point set. Another source for the difference in the obtained barriers could be the thickness of the slab: while we used a 5-layer slab with adatoms on both sides of the slab, Boisvert and Lewis [111] used a three-layer slab with a Cu adatom only on one side of the slab. Actually Boisvert and Lewis [111] tested the dependence of the diffusion barrier on the slab thickness for the (2×2) -unit cell and found that while the barrier for hopping is relatively stable with respect to slab thickness, the one for exchange changes from 1.05 eV (four layers) to 1.18 eV (six layers). However, concerning the GGA values Boisvert and Lewis [111] obtained in a (3×3) -unit cell and a four-layer slab, 0.52 eV for hopping and 0.96 eV for exchange, the agreement with our results is quite good.

A large number of experimental and theoretical results for the diffusion barrier of Cu on the flat Cu(001) surface can be found in the literature. Table 5.1 presents some of these results together with the values obtained in this study: In particular we have listed data from *ab initio* calculations, from calculations with the semiempirical embedded atom method (EAM), and from experiment. The diffusion barrier for hopping obtained in different EAM calculations [27, 28, 111, 135, 136] ranges from 0.43 eV to 0.50 eV and is in good agreement with the GGA-value from the *ab initio* calculations. On the other hand, for exchange diffusion the EAM-value obtained by Boisvert and Lewis [111] is lower than the one from *ab initio* calculations but still shows the right tendency that hopping is the favored mechanism for adatom diffusion for Cu on Cu(001). Introducing a covalent correction to the EAM-total energy leads to a two times lower diffusion barrier for exchange (0.23 eV) than the one for hopping (0.43 eV) [27] which, as shown above, is in severe contrast to the predictions from DFT calculations.

The diffusion barriers determined from experiment vary between 0.28 eV and 0.40 eV. In the work of Miguel *et al.* [137] the mean size of the terraces as a function of temperature was measured with thermal-energy atom scattering (TEAS) and the diffusion barrier obtained from fitting to an Arrhenius law is 0.4 eV. One

of the uncertainties of this approach is that both the prefactor Γ_0 and the diffusion barrier E_d from Eq. 5.1 are determined at the same time. Breeman and Boerma [139] used low-energy ion scattering (LEIS) to determine the temperature at which adatom mobility sets in. Assuming a prefactor of 10^{13}s^{-1} the diffusion barrier was determined to be 0.39 ± 0.06 eV. The last two experiments determined the diffusion barrier from the island separation $L \propto \left(\frac{D}{F}\right)^{\frac{1}{i+2}}$ where D is the diffusion constant, F the deposition flux and i the critical nucleus size. Ernst *et al.* [138] investigated the dependence of the average island separation on the deposition rate for a constant temperature $T = 220$ K and obtained a critical exponent of $p = 1/4$ from which they determined a barrier of 0.28 eV. However, a recent reexamination of their data using a critical exponent $p = 1/3$ which corresponds to $i = 1$ yielded a barrier of 0.42 ± 0.09 [26] and is thus in good agreement with the other experimental findings. Dürre *et al.* [140] assumed that all islands smaller than the tetramer are unstable ($i = 3$) and determined a barrier of 0.36 ± 0.03 . We conclude that the experimentally determined barriers are somewhat lower than the GGA value of 0.49 eV. Although small, this difference still leaves some doubt on whether hopping is the predominant diffusion mechanism on Cu(001). Recently, also vacancy diffusion was discussed as a possible mass transport mechanism [141], for which Boisvert and Lewis [111] obtained a barrier of 0.42 eV.

5.3.2 Structure and bond lengths in the transition state

Our total-energy calculations show that hopping is clearly the favored diffusion mechanism for adatom selfdiffusion on Cu(001). In this Section we present the optimized geometry at the transition state for hopping and exchange. We also compare the bond lengths to a previous *ab initio* study for the selfdiffusion on Ag(001) [31] and results obtained with effective medium theory for Cu on Cu(001) [136].

Transition state of hopping diffusion

The relevant bond lengths in the transition state of hopping diffusion and the relative change compared to the bond length in fcc Cu bulk is summarized in Table 5.2. We remind the reader that the bond lengths and lattice constants are generally larger within GGA due to the larger lattice constant. However the relative changes of bond lengths compared to the bond length in bulk are very close for both treatments of the exchange-correlation functional, LDA and GGA. At the bridge site, shown in Fig. 5.2 a), which is the transition state (TS) for hopping

diffusion, the Cu adatom has a twofold coordination. Due to this fact the bonds

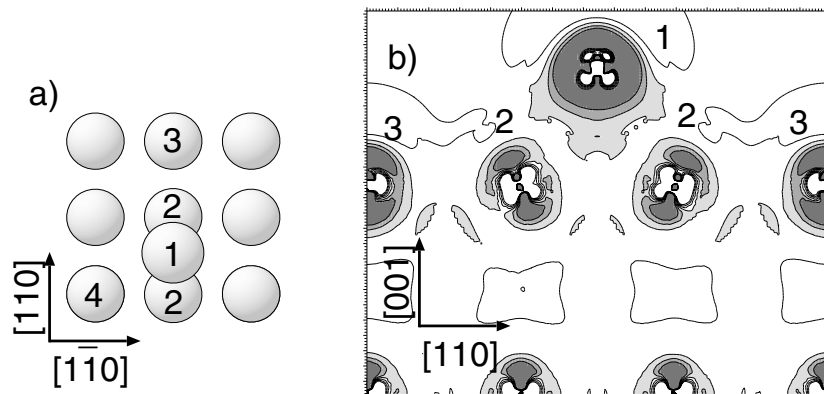
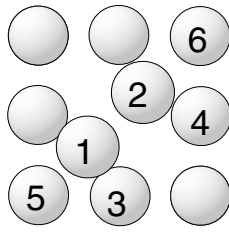


Figure 5.2: Change in electron density with respect to the superposition of atomic densities in the transition state of hopping diffusion of Cu on Cu(001). The top view of the surface geometry is given in a), while b) represents a cross-section along the $[110]$ -direction which contains the atoms 1, 2 and 3. Grey indicates regions of electron-density increase while regions of electron-density depletion are marked only by contour lines. The contour lines start at $\pm 2 \times 10^{-3} \text{bohr}^{-3}$ and have a separation of $4 \times 10^{-3} \text{bohr}^{-3}$.

to its nearest neighbors are noticeably reduced compared to the initial state (IS) where it has 4 nearest neighbors, i.e. from -4.4% (IS) to -7.3% (TS). However, the distance to the next nearest neighbor is 36.0% larger. Similar results were obtained by Perkins and DePristo [136] from the corrected effective medium theory (CEM), namely, $\frac{d_{12}-d_{\text{bulk}}}{d_{\text{bulk}}} = -8\%$ and $\frac{d_{14}-d_{\text{bulk}}}{d_{\text{bulk}}} = 33\%$. Total-energy calculations for the selfdiffusion on the (001)-surface of Ag [31], which is isoelectronic to Cu, give similar structural relaxations for the bridge site: The bond length between the adatom and its nearest neighbor is 3% shorter than in the fourfold hollow site.

	TS hopping diffusion of a Cu adatom			
	LDA		GGA	
	[bohr]	$\frac{d_{ij}-d_{\text{bulk}}}{d_{\text{bulk}}} [\%]$	[bohr]	$\frac{d_{ij}-d_{\text{bulk}}}{d_{\text{bulk}}} [\%]$
d_{12}	4.40	-7.3	4.53	-7.3
d_{14}	6.45	36.0	6.64	36.0

Table 5.2: Bond lengths in the transition state of hopping diffusion (bridge site) of Cu in bohr and relative to the bond length in Cu bulk d_{bulk} . The structure is fully optimized. Exchange-correlation potentials are treated in LDA and GGA ($d_{\text{bulk}}^{\text{LDA}} = 4.74$ bohr and $d_{\text{bulk}}^{\text{GGA}} = 4.88$ bohr). The numbering of the atoms corresponds to that in Fig. 5.2.



	TS exchange process of Cu			
	LDA		GGA	
	[bohr]	$\frac{d_{ij}-d_{\text{bulk}}}{d_{\text{bulk}}}$ [%]	[bohr]	$\frac{d_{ij}-d_{\text{bulk}}}{d_{\text{bulk}}}$ [%]
d_{12}	4.47	-5.7	4.60	-5.7
d_{13}	4.40	-7.3	4.53	-7.2
d_{15}	5.14	8.7	5.28	8.2

Table 5.3: Top view of of the surface atoms in the transition state of exchange diffusion of Cu on Cu(001). The table contains bond lengths d_{ij} and deviations from the bond length in Cu bulk d_{bulk} in % obtained after a structural optimization treating the exchange-correlation potential in LDA and GGA ($d_{\text{bulk}}^{\text{LDA}} = 4.74$ bohr and $d_{\text{bulk}}^{\text{GGA}} = 4.88$ bohr).

Transition state of diffusion by atomic exchange

Diffusion by atomic exchange is a concerted process involving a large number of atoms. Thus finding the transition state is a very complicated issue and choosing the right strategy is decisive to make the task feasible. We selected the

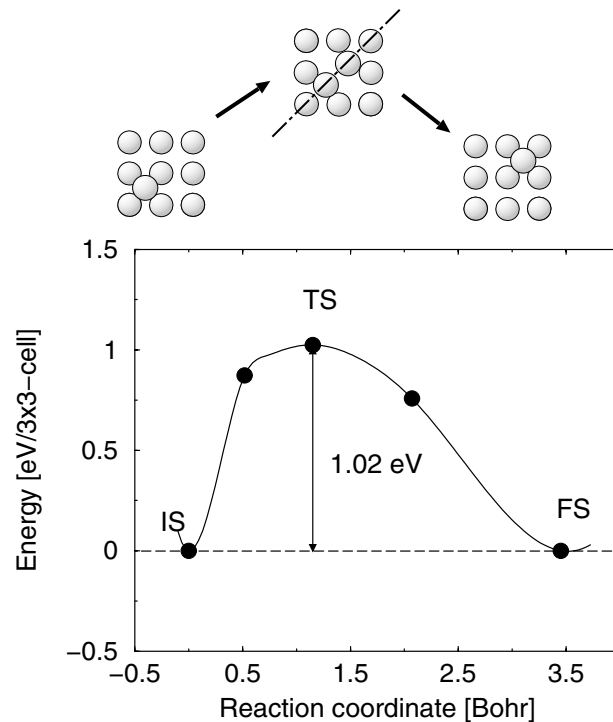


Figure 5.3: Energy in [eV/(3 × 3)-cell] along the reaction path for atomic exchange of Cu on Cu(001). The zero point of the energy is set at the adsorption energy in the initial state (Cu on a fourfold hollow site). The reaction coordinate represents the coordinate of the Cu atom along the [100] direction.

$x = y$ coordinate of the atom Cu1 connecting the initial (Cu1 at fourfold hollow site) with the final state (Cu1 in a substitutional site) as a reaction coordinate. Note that the numbering of the atoms corresponds to the one given in Table 5.3. A top view of the initial, transition and final geometry are given schematically in Fig. 5.3. At each point along the diffusion path the z -coordinate of Cu1 and all coordinates of the remaining surface atoms were relaxed. The adsorption energy along the diffusion path is given in Fig. 5.3 with respect to the energy in the initial state. The maximum along the reaction path corresponds to the transition state.

In the transition state of exchange diffusion shown in Table 5.3 the adatom 1 and the substrate atom 2 are above the surface layer vacancy. The height of the so formed dimer above the surface layer is reduced by 24% (s. Table 5.4). Each of the topmost adatoms can be considered as fourfold coordinated. The distance between atoms 1 and 2 is reduced by 5.7% compared to d_{bulk} , thus about 1% shorter than in the fourfold hollow site in the initial state. The shortest bond length is between atoms 1 and 3 (2 and 4) and is reduced by 7.5% compared to d_{bulk} . At the same time the distance between atom 1 and 5 is enhanced by 8.7%. For the TS of exchange diffusion we observe again similar relaxations for Cu and Ag, the distances d_{12}^{Ag} and d_{13}^{Ag} being reduced by -6% and -7.4% , respectively, while d_{15}^{Ag} is expanded by 5% [31]. Using CEM Perkins and DePristo [136] obtain an even stronger contraction of -12% and -11% of d_{12} and d_{13} , respectively. However, we note this result has to be treated with caution because the corrected effective medium method used in Ref. [136] gives an exchange diffusion barrier similar or even lower than the one for hopping which contradicts the results from density functional theory.

The electron density change with respect to the superposition of atomic densities is shown in Fig. 5.4. Indeed, the strongest electron charge redistribution is observed between atoms Cu1 and Cu2, and Cu1 and Cu3, *i.e.* between the atom pairs with the shortest bonds. The covalent character of the bonds in the TS of the exchange process was argued to be the reason why exchange diffusion is favored on Al(100) [29] or Au(100) [32]. However for Cu(001), as well as for Ag(001) [31], there is no substantial accumulation of electron charge between the atoms 1 and 2 and 1 and 3, thus these bonds do not possess a pronounced covalent character.

	Atom 1	Atom 3	Atom 5
$\frac{z-z_0}{z_0} [\%]$	-23.8	-3.7	-2.6

Table 5.4: Relaxation of the interlayer spacing in the transition state of the exchange process of Cu with respect to the interlayer spacing in Cu bulk z_0 in %. The numbering of the atoms corresponds to the one in Fig. 5.3.

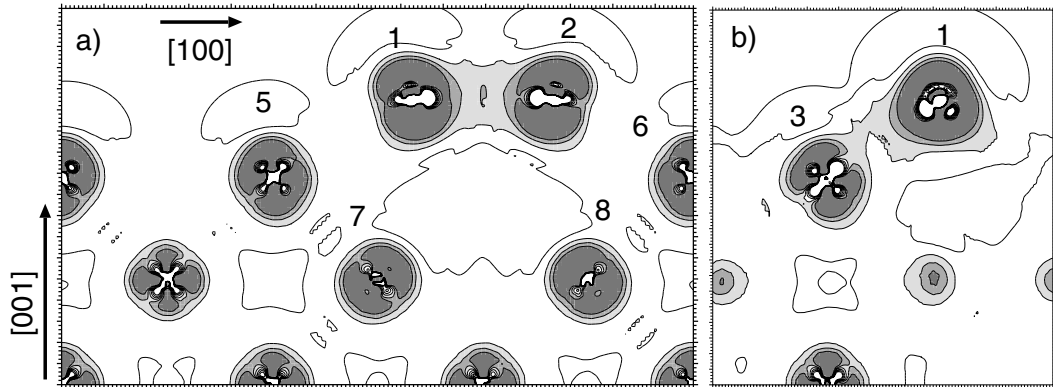


Figure 5.4: Change in electron density with respect to the superposition of atomic densities in the transition state of exchange diffusion of Cu on Cu(001). a) represents a cross-section through the slab in [100]-direction, b) shows a cross-section that contains the atoms 1 and 3. The grey regions correspond to regions of electron-density increase while regions of electron-density depletion are marked only by contour lines. The contour lines start at $\pm 2 \times 10^{-3} \text{bohr}^{-3}$ and have a separation of $4 \times 10^{-3} \text{bohr}^{-3}$. The numbering of the atoms corresponds to the one in Fig. 5.3.

5.4 Co adatom diffusion on the Cu(001)-surface

While there is a great number of theoretical as well as experimental investigations of the diffusion constants for homoepitaxial growth especially of noble elements, this is hardly the case for the heteroepitaxial growth of transition metal elements on a noble metal substrate. To our best knowledge there is no information on energy barriers for diffusion of Co on Cu(001) in the literature. This is due mainly to the fact that the initial growth of this system is not well understood. Experimental indications of surface intermixing imply that the growth of Co on Cu(001) does not fit in the traditional picture of island nucleation as the result of binary collisions of adatoms on the surface. Several studies based on rate equations [39, 113] described heteroepitaxial growth with exchange processes (*e.g.* for Fe/Cu(001)) by assuming monomer stability, $i = 0$. However, in this case island density should be independent of F and D and thus it is not possible to determine the diffusion barrier from an Arrhenius plot.

On the other hand, theoretical approaches can help identify what are the relevant processes in the heteroepitaxial growth and determine the corresponding energy barriers. Thus, an understanding of the origin of differences to the homoepitaxial case can be achieved. However, the application of semiempirical approaches like effective medium theory on elements, where d - d -interactions are important, is problematic. Even in the description of ground state properties of

Co large deviations are found with respect to DFT-LDA results, *e.g.* the cohesive energy is 1-2 eV larger than the one obtained with DFT-LDA [142]. Improvements of the efficiency of all-electron DFT approaches have only recently made it possible to investigate the system sizes relevant for growth phenomena. Here, we study in particular two processes: hopping and atomic exchange of Co on Cu(001). In a first step we will neglect the effects of spin-polarization on the energy barriers. This gives us the opportunity to resolve the effects of chemical bonding and construct a simple picture which explains the different behavior of Co and Cu adatoms on the surface. In a second step we then investigate the influence of spin-polarization on the barrier in Section 5.6.

5.4.1 Diffusion barriers

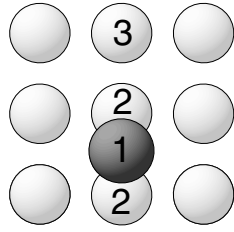
For diffusion via hopping on Cu(001) E_d of a non-magnetic Co adatom amounts to 1.03 eV (LDA) and 0.92 eV (GGA). The barrier for the exchange process obtained in LDA is 1.22 eV and in GGA 1.00 eV. Analogous to the selfdiffusion on Cu(001), the GGA treatment leads to a reduction of the diffusion barrier, namely, by 0.11 eV for hopping and 0.22 eV for exchange. We concentrate in the following on the diffusion barriers obtained within GGA since, as we have seen in the case of copper, the GGA values are closer to the ones determined experimentally. The diffusion barrier for hopping of Cu, 0.49 eV, is much lower than the one for Co, 0.92 eV. However, in contrast to Cu for which the diffusion barrier for exchange is almost twice as large as the one for hopping (1.02 eV compared to 0.49 eV), for a non-magnetic cobalt adatom the barriers for both diffusion processes are very close, the one for exchange being only 0.08 eV higher than that for hopping. This implies, that unlike Cu, for Co on the flat Cu(001) surface both processes should be relevant for the initial growth.

5.4.2 Structural and electronic effects

In this Section the structural and electronic changes in the transition state of hopping and exchange of Co are presented and compared to the ones for Cu selfdiffusion.

Transition state of hopping diffusion

The bond lengths in the transition state of hopping diffusion are listed in Table 5.5 together with a top view of the surface atoms. The bond length between the twofold coordinated Co adatom at the bridge site and its nearest Cu neighbor 2 is contracted by 11%, *i.e.* the Co-Cu bond length is 3% shorter than the one



TS Hopping Diffusion of Co				
LDA			GGA	
	[bohr]	$\frac{d_{ij}-d_{\text{bulk}}}{d_{\text{bulk}}} [\%]$	[bohr]	$\frac{d_{ij}-d_{\text{bulk}}}{d_{\text{bulk}}} [\%]$
d_{12}	4.21	-11.0	4.35	-10.8
d_{23}	4.70	-1.0	4.83	-1.0

Table 5.5: Top view of of the surface atoms in the transition state of hopping diffusion of Co on Cu(001). The dark grey atom is Co and light grey atoms are Cu atoms. The table contains bond lengths d_{ij} and deviations from the bond length in Cu bulk d_{bulk} in % obtained after a structural optimization treating the exchange-correlation potential in LDA and GGA ($d_{\text{bulk}}^{\text{LDA}} = 4.74$ bohr and $d_{\text{bulk}}^{\text{GGA}} = 4.88$ bohr).

in the initial state where Co has four Cu neighbors. d_{12} is 3.7% shorter than the corresponding distance in TS of hopping diffusion for Cu. The Co adatom is located 3.45 bohr above the surface, while the Cu adatom at a bridge site lies 3.67 bohr above the surface.

	Atom 1 (Co)	Atom 2
$\frac{z-z_0}{z_0} [\%]$	2.8	-3.8

Table 5.6: Relaxation of the interlayer spacing in the transition state of hopping diffusion (bridge site) of Co with respect to the interlayer spacing in Cu bulk z_0 in %. The numbering of the atoms is explained in Fig. 5.5.

Transition state of exchange process

Similar to the homoepitaxial case, in order to find the transition state of the exchange process, the Co atom was moved along the [100]-direction connecting the initial (Co at fourfold hollow site) with the final state (Co in a substitutional site). At each point along the diffusion path the z -coordinate of Co adatom and all coordinates of the remaining surface atoms were relaxed. A top view of the initial, transition and final geometry are shown in Fig. 5.5. Additionally, in Fig. 5.5 the adsorption energy along the diffusion path is given with respect to the energy in the initial state. The maximum along the reaction path corresponds to the transition state.

A top view of the surface atoms in the TS of exchange of Co on Cu(001) and the interatomic distances are given in Table 5.7. The Co-Cu dimer above the surface vacancy relaxes strongly towards the substrate layer, the height of the Co atom is reduced by 35.4% with respect to the ideal interlayer spacing of Cu bulk, while the Cu atom relaxes 28% inwards. This relaxation is more pronounced than

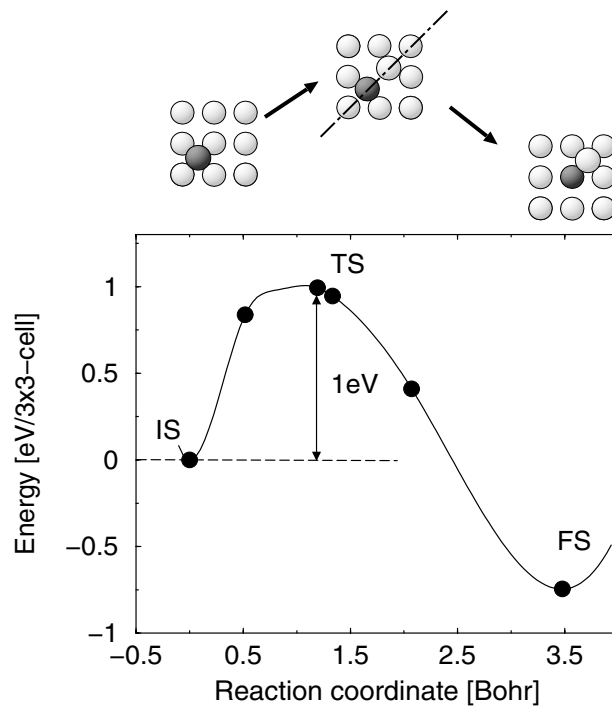


Figure 5.5: Energy in [eV/(3 × 3)-cell] along the reaction path for atomic exchange of Co on Cu(001). The zero point of the energy is set at the adsorption energy in the initial state (Co on a fourfold hollow site). The reaction coordinate represents the coordinate of the Co atom along the [100]-direction.

the one of the Cu dimer in the TS of exchange of Cu, which is -23% . The distance between the topmost atoms, Co1 and Cu2 is similar to the bond length of Co in the fourfold hollow site in IS, the reduction with respect to $d_{\text{bulk}}^{\text{Cu}}$ being 7.3% and 7.9% , respectively. The distance between the Co atom and its nearest Cu neighbors 3 and 5, is reduced by 11% and increased by 4% compared to $d_{\text{bulk}}^{\text{Cu}}$, respectively. The corresponding lengths for the Cu adatom are $\frac{d_{24}-d_{\text{bulk}}}{d_{\text{bulk}}} = -8.5\%$ and $\frac{d_{26}-d_{\text{bulk}}}{d_{\text{bulk}}} = 7\%$.

Generally, the bond lengths of Co to its nearest neighbors are shorter than the ones of the Cu adatom, while the bond lengths of Cu2 resemble the ones of the Cu adatoms in TS of exchange in the the homoepitaxial case (s. Table 5.3). This result is in line with the fact that shorter bond lengths correspond to stronger bonds and can be observed in the change of electron density with respect to the superposition of atomic densities $\Delta n(r)$ plotted in Figs. 5.4 and 5.6. For example Fig. 5.4 a) and Fig. 5.6 a) represent cross-sections in the [100]-direction perpendicular to the slab in the plane containing the atoms 5, 1, 2 and 6 for the TS of the exchange process for Cu and Co, respectively (cf. Table 5.7 for

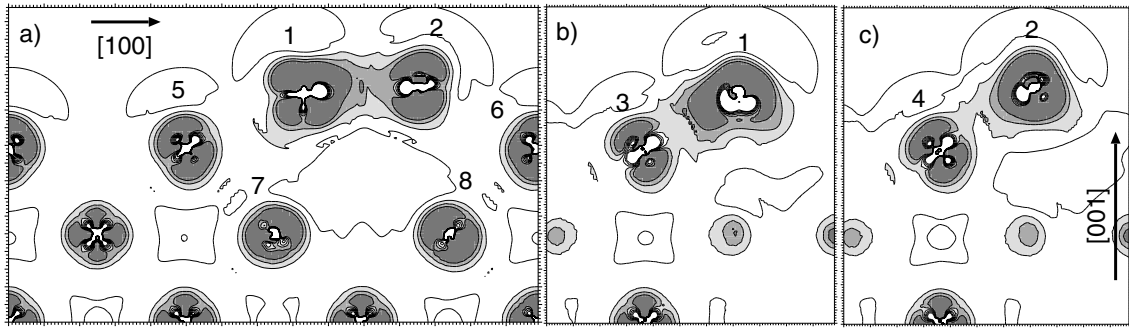
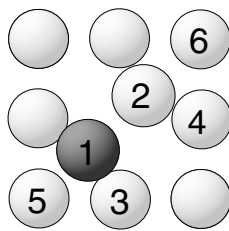


Figure 5.6: Change in electron density with respect to the superposition of atomic densities in the transition state of the exchange process of Co on Cu(001): a) represents a cross-section through the slab in the [100]-direction, b) and c) show cross-sections that contain the atoms 1 and 3 and 2 and 4, respectively (cf. Table 5.7 for the numbering of the atoms). The grey regions correspond to regions of electron-density increase while regions of electron-density depletion are marked only by contour lines. The contour lines start at $\pm 2 \times 10^{-3} \text{ bohr}^{-3}$ and have a separation of $4 \times 10^{-3} \text{ bohr}^{-3}$.

the numbering of the atoms). Both plots reveal that the strongest bond is formed between the atoms 1 and 2 as opposed to the bonds between 1 and 5, and 2 and 6. However, the accumulation of charge is much more distinct between the Co and Cu adatom in Fig. 5.6 a), than between the Cu adatoms of the dimer, Fig. 5.4 a). A more pronounced charge redistribution takes place also between the atoms 1 and



	TS exchange process of Co			
	LDA		GGA	
	[bohr]	$\frac{d_{ij}-d_{\text{bulk}}}{d_{\text{bulk}}} [\%]$	[bohr]	$\frac{d_{ij}-d_{\text{bulk}}}{d_{\text{bulk}}} [\%]$
d_{12}	4.40	-7.3	4.52	-7.4
d_{13}	4.24	-10.8	4.35	-10.8
d_{24}	4.35	-8.5	4.47	-8.4
d_{15}	4.94	4.1	5.07	3.9
d_{26}	5.07	6.9	5.22	7.0
d_{17}	5.48	15.4	5.64	15.6
d_{28}	5.77	21.6	5.94	21.7

Table 5.7: Top view of the surface atoms in the transition state of Co exchange on Cu(001). The dark grey atom is Co and light grey atoms are Cu atoms. The table contains bond lengths d_{ij} and deviations from the bond length in Cu bulk d_{bulk} in % obtained after a structural optimization treating the exchange-correlation potential in LDA and GGA ($d_{\text{bulk}}^{\text{LDA}} = 4.74 \text{ bohr}$ and $d_{\text{bulk}}^{\text{GGA}} = 4.88 \text{ bohr}$).

	Atom 1 (Co)	Atom 2	Atom 3	Atom 4	Atom 5	Atom 6	Atom 7
$\frac{z-z_0}{z_0}$ [%]	-35.4	-28.1	-3.8	-3.7	-1.3	-2.3	1.3

Table 5.8: Relaxation of the interlayer spacing in the transition state of atomic exchange of Co with respect to the interlayer spacing in Cu bulk z_0 in %. The numbering of the atoms corresponds to the one in Fig. 5.7.

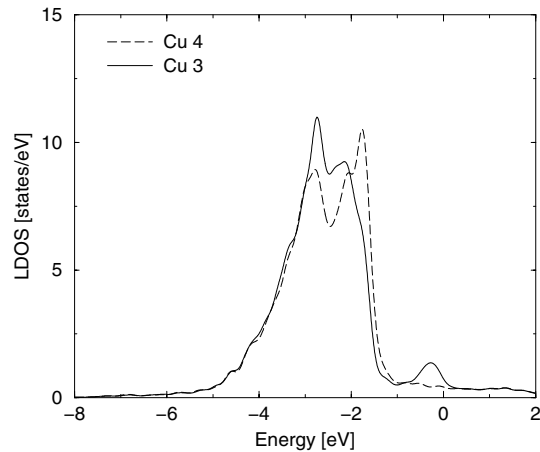


Figure 5.7: The local density of states in the muffin tin of the nearest substrate neighbors to the Co-Cu dimer, atoms 3 and 4, in the transition state of atomic exchange of Co on Cu(001). The numbering of the atoms corresponds to the one used in Fig. 5.7.

3 in Fig. 5.6 b) than between 2 and 4 in Fig. 5.6 c).¹ Additionally the local density of states (LDOS) from the muffin tin of atoms Cu3 and Cu4 is plotted in Fig. 5.7. A relative shift of the d -band of atom 3 towards lower energies compared to the one of atom 4 indicates the stronger covalency of the bond between atoms Cu3 and Co1 compared to atoms Cu4 and Cu2. Actually, the local environment of atoms Cu4 and Cu6 is similar to the homoepitaxial case therefore the electronic effects taking place between the atom Cu2 and its neighbors Cu4 and Cu6 resemble a lot the ones in the homoepitaxial case as a comparison of Fig. 5.6 c) and Fig. 5.4 b) yields. Thus, analyzing the bonds between atom 4 and 2 in the TS of Co exchange process one can get an idea of the situation in the homoepitaxial case.

¹Note that due to the different height of atoms Co1 and Cu2 over the surface layer, atoms 1, 2, 3 and 4 do not lie in the same plane as is the case for the selfdiffusion of Cu(001) where the TS is symmetrical.

5.5 Comparison of Co and Cu adatom diffusion on the flat Cu(001)-surface

There are several findings we would like to discuss in this Section: The barrier for exchange for Cu is twice as high as the one for hopping while for a non-magnetic Co atom both processes have similar barriers, 0.92 eV and 1.00 eV, respectively. The exchange barriers for Co (1.00 eV) and Cu (1.02 eV) are very similar. We try to explain these facts using a bond-cutting argument: find how many and what bonds are broken in the corresponding transition state compared to the initial state and relate this information to the height of the barrier.

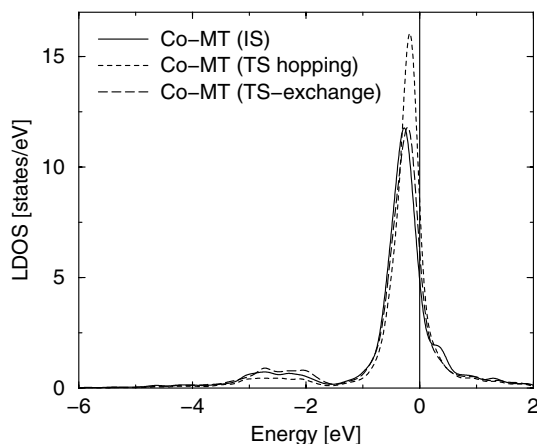


Figure 5.8: The local density of states in the muffin tin of the Co adatom in the initial state (solid line), transition state of hopping (dotted line) and exchange (dashed line).

In the TS of hopping diffusion the adatom (Co or Cu) is twofold coordinated, *i.e.* there are two Ad -Cu-bonds ($Ad = \{Co, Cu\}$) missing compared to the initial state. On the other hand, in the transition state of exchange the adatom is fourfold coordinated, *i.e.* it has the same coordination as in the initial state. For example for a Co adatom the effect of the coordination is reflected in the local density of states in the muffin tin of Co shown in Fig. 5.8. While the d -band of the fourfold coordinated Co atom in the transition state of exchange almost coincides with the one in the initial state, the d -band of the Co adatom in the bridge site is noticeably narrower and shifted to higher energies which indicates a weaker binding to the substrate.

In the transition state of exchange the Cu atom that is being “kicked out” is now fourfold coordinated while it was ninefold coordinated in the initial state. Thus, during the exchange process of both Co and Cu the same type of bonds, namely Cu-Cu-bonds, are broken and consequently the height of the barrier is

similar.

For hopping, however, the situation is different. In case of a Co adatom there are two Co-Cu bonds that are broken, while in case of a Cu adatom, Cu-Cu bonds are broken in the transition state. Since Co-Cu bonds are stronger than Cu-Cu bonds, the diffusion barrier for Co is much higher (0.92 eV) than the one for Cu (0.49 eV).

For the homoepitaxial case, the number of broken Cu-Cu bonds in the TS of exchange, five, as opposed to two in the TS of hopping explains why the barrier for exchange is approximately two times higher than for hopping.

5.6 Influence of magnetism on the barrier height of Co

The simple bond-breaking picture used in the previous Section gives already an idea about the influence of spin-polarization on the different configurations. As we have seen, the coordination of Co in the transition state of exchange is the same as in the initial state, therefore we expect the same energy gain due to spin-polarization for both configurations. Consequently, the barrier height should not be affected strongly. Indeed, our results show no substantial change of the barrier for exchange of a spin-polarized Co adatom. The magnetic moment of the Co atom is in line with this result, *i.e.* it is $1.81\mu_B$ and $1.77\mu_B$ for the initial state and transition state, respectively.

On the other hand, for hopping the coordination of the Co atom changes from four in the initial state to two in the transition state (bridge site). The lower coordination in the transition state implies a larger energy gain due to spin-polarization. Thus a substantial reduction of the diffusion barrier is expected. Actually, the barrier for hopping drops from 0.92 eV for a nonmagnetic Co adatom to 0.61 eV for a spin-polarized. The spin moment of the Co adatom at the bridge site is also noticeably larger, $1.94\mu_B$ than in the initial state, $1.81\mu_B$.

Chapter 6

Stepped surfaces: formation energies, adsorption and diffusion at steps

6.1 Introduction

Two different kinds of steps on the (001)-surface are expected to have a potentially low formation energy [31]: a close packed in $[110]$ -direction with a $\{111\}$ -microfacet and an open step along the $[100]$ -direction with a $\{110\}$ -microfacet edge. Both types are shown schematically in Fig. 6.1. Generally, for fcc(001)-metal surfaces the $\{111\}$ -faceted steps are more stable and therefore islands obtain preferentially a square form with edges along the $[110]$ - and $[1\bar{1}0]$ -directions. This was also observed for homoepitaxy of Cu(001) from a 2-dimensional diffraction pattern obtained with high resolution LEED [140]. In a recent *ab initio* study Yu and Scheffler [31] determined the formation energy of the $\{111\}$ - and $\{110\}$ -faceted step on Ag(001) to be 0.130 eV/per step atom and 0.156 eV/per step atom, respectively. This result is interpreted as a consequence of the coordination of the step edge atoms which is seven for the $\{111\}$ -faceted step and six for the $\{110\}$ -faceted step. Applying the Wulff construction Yu and Scheffler [31] found that the equilibrium island shape should be octagonal with an edge length ratio of the $\{111\}$ - to $\{110\}$ -faceted steps of 10 : 3. For Cu(001) a similar nearly square island shape is expected and indeed observed experimentally as mentioned above. Therefore, in this Chapter the $\{111\}$ -faceted steps are studied. In Section 6.2 the formation energy of $[110]/\{111\}$ -step is calculated and compared to semiempirical values for Cu(001) [28, 135] and *ab initio* values for Ag(001) [31]. In addition, the optimized structure of the stepped surface is presented.

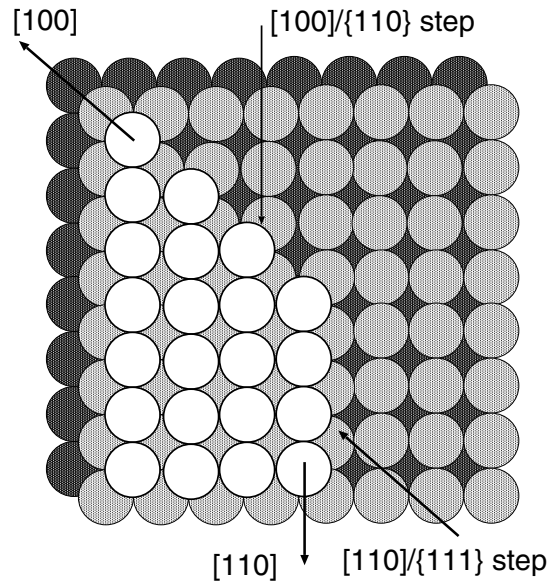


Figure 6.1: Top view of monoatomic steps on the fcc(100)-surface: close packed with a $\{111\}$ -microfacet along the $[110]$ -direction and an open one with a $\{110\}$ -microfacet along the $[100]$ -direction.

In Section 6.3 we study the adsorption of Co and Cu adatoms at steps, where they are fivefold coordinated. Summarizing all the calculated adsorption energies of Co and Cu adatoms as a function of coordination number, we verify whether E_{ad} can be described with a square root dependence on the coordination number. The relaxations and bond lengths of both adsorbate systems are presented.

While the barrier on the flat terrace determines the island density, the diffusion barrier along a step is responsible for the island shape. A high diffusion barrier leads to rough island and step edges while a low diffusion barrier means that the equilibrium island shape can be reached, provided that the adatoms can diffuse also around island corners. As known from a previous *ab initio* study on the homoepitaxy of Ag(001) [31], an element which is isoelectronic to Cu and therefore has similar properties, diffusion along the close packed $[110]/\{111\}$ -step proceeds via hopping. Therefore this mechanism is investigated for adatoms diffusing along the step ledge in Section 6.4. STM experiments and *ab initio* calculations (cf. Chapter 4) suggest that also for Co on Cu(001) at elevated temperatures the first islands consist mainly of Cu atoms. Thus the diffusion barrier of both Co and Cu adatoms along the $[110]/\{111\}$ step is an important parameter to understand island shapes also in the case of heteroepitaxy.

In Section 6.5 the activation temperature for the microscopic processes studied with DFT-GGA is calculated. A qualitative picture of the growth mode in the

homo- and heteroepitaxial case with respect to the temperature scale on which the different processes take place is established .

6.2 Formation energy of the close packed step

The formation energy of the step is the difference between the surface energies of the stepped surface and the flat (001) surface. The stepped surface was modeled in a (4×1) -unit cell with a ledge separation of 2 nearest neighbor distances. The top and side view of the grooved surface is shown in Fig. 6.2. The thickness of the slab in the grooves is 3 atomic layers. In order to minimize the numerical error, the reference systems, a 5 and 3 ML thick Cu(001) slab, needed to calculate the formation energy of the step, were calculated also in a (4×1) -unit cell. All the calculations were performed within GGA. The cut off parameter of the plane wave basis set is equal to the one used for the diffusion barriers on the flat Cu(001) surface, 13.8 Ry. The Brillouin-zone integration was performed with 10 k_{\parallel} -points which corresponds to 40 k_{\parallel} -points in a $p(1 \times 1)$ -unit cell. Actually, the surface energy of a Cu(001) slab is already well converged for 36 k_{\parallel} points in the BZ (or 6 k_{\parallel} in the irreducible BZ) (cf. Table 3.1). The surface energy of Cu(001) obtained for a (4×1) -cell, 0.61 eV, is in very good agreement with the one for a (1×1) -unit cell, 0.60 eV.

The formation energy of the $[110]/\{111\}$ step on the Cu(001) surface is 0.137 eV/step-edge atom (GGA). This value is close to the one obtained with

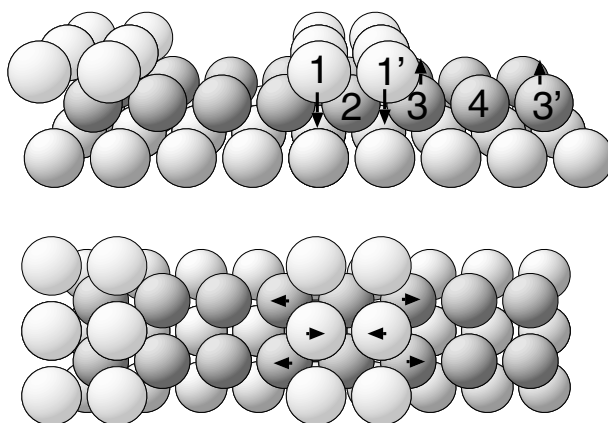


Figure 6.2: Side and top view of a stepped fcc(100)-surface with close packed steps with a $\{111\}$ - microfacet along the $[110]$ -direction. The arrows indicate the displacements of the atoms with respect to the unrelaxed geometry. The exact values of the displacements are given in Table 6.1.

	Δx [bohr]	Δy [bohr]	$\frac{\Delta z}{z_0}$ [%]
Atom 1	0.023	0.0	-3.3
Atom 2	0.0	0.0	0.0
Atom 3	0.031	0.0	1.3
Atom 4	0 0	0.0	0.0

Table 6.1: Lateral relaxations Δx and Δy in bohr and relaxation of the interlayer spacing with respect to the interlayer spacing in Cu bulk z_0 in % in a close packed step along the [110]-direction. The numbering of the atoms corresponds to the one in Fig. 6.2.

the plane-wave pseudopotential method for Ag(001) in a 4 layer slab with a ledge separation of 3 nearest neighbor distances, 0.130 eV/step-edge atom (LDA) [31]. In an EAM study, Tian and Rahman [135] determined the isolated ledge energy per ledge atom to be 0.157 eV. The agreement to previous *ab initio* results for Ag(001) and to semiempirical calculations for vicinal Cu surfaces shows that the grooved surface modeled in a (4×1) unit cell with a ledge separation of 2 nearest neighbor distances gives a good description of the properties of a [110]/{111} step.

Fig. 6.2 also contains the direction of the displacement of the surface atoms obtained after a structural optimization. The values of the displacements are displayed in Table 6.1 and the corresponding bond lengths in Table 6.2. The relaxation of the surface atoms 1 and 1' of -3.3% with respect to the interlayer distance in fcc copper bulk towards the subsurface layer is similar to the one of the surface atoms on the flat Cu(001) surface which is -3.0% . On the other hand, the step bottom atom 3 and 3' relax outwards by 1.3% . The lateral relaxation takes place in x -direction, perpendicular to the ledge: the surface atoms 1 and 1' relax towards each other by 0.023 bohr each while the step bottom atoms 3 and 3' relax away from the step edge by 0.031 bohr each. The distance between the surface atom 1 and the step bottom atom 3 is reduced by 1.8% with respect

	[bohr]	$\frac{d_{ij}-d_{\text{bulk}}}{d_{\text{bulk}}}$ [%]
d_{12}	4.79	-1.8
d_{13}	4.79	-1.8
d_{23}	4.91	0.6
d_{34}	4.84	-0.8

Table 6.2: Bond lengths and deviations from the bond length in Cu bulk d_{bulk} in % in the relaxed geometry of a close packed step along the [110]-direction. The numbering of the atoms corresponds to the one in Fig. 6.2.

to the bulk bond length which is close to the bond length between the surface and subsurface atom in Cu(001), -1.5% . We note that the atomic displacements obtained for a $[110]/\{111\}$ step on the Cu(001) and Ag(001) [31] surface have the same direction.

6.3 Adsorption of Co and Cu adatoms at steps

The calculations for adsorption of Cu and Co adatoms at a $[110]/\{111\}$ -step were performed in a (4×2) -unit cell. The distance between the adsorbates along the step corresponds to 2 nearest neighbor distances. This choice is justified because as we know from the adsorption energies of Co on the flat Cu(001) surface the interaction between the adatoms is negligible at such distances: *e.g.* the DFT-LDA adsorption energies calculated in a $p(2 \times 2)$ and $p(3 \times 3)$ unit cell are practically the same: 3.94 eV and 3.95 eV, respectively.

The calculations were performed with the same cutoff parameters as the ones for diffusion barriers on the flat Cu(001) surface, *e.g.* the cut off parameter for the plane-wave basis set is 13.8 Ry. 10 k_{\parallel} -points in the (4×2) -unit cell were used for the Brillouin-zone integration. This corresponds to 80 k_{\parallel} -points in the (1×1) -unit cell. An increase of the k_{\parallel} -point set to 21 resulted in a slight decrease of the total-energy of the system by 0.07 eV. However, the same change was obtained for all systems, therefore the height of the diffusion barriers as a difference between the energy at the saddle point and the adsorption site is not affected by the k_{\parallel} -point sampling.

6.3.1 Adsorption energies

An adatom adsorbed at the $[110]/\{111\}$ -step has five nearest neighbors. In order to get a better idea how the adsorption energy changes with coordination the adsorption energy of Cu and Co adatoms obtained within GGA at different adsorption sites is displayed in Table 6.3. It includes the twofold coordinated bridge site, the fourfold coordinated on-surface site, the adatom at a step, and for Cu the adsorption energy at a kink site, which equals the cohesive energy of Cu, 3.50 eV (GGA). Additionally the adsorption energy of a Co or Cu adatom at a substitutional site with $N = 8$ is given. In contrast to the way E_{ad} at a substitutional site was defined in Eq. 4.1, Chapter 4, here we are interested in the energy gain due to adsorption in a surface vacancy thus the formation energy of the vacancy was not taken into account. *i.e.* to obtain E_{ad} the energy of a surface vacancy and a free Co or Cu atom was subtracted from the energy of the adsorbate system.

The adsorption energy of a Co adatom shows a much stronger dependence

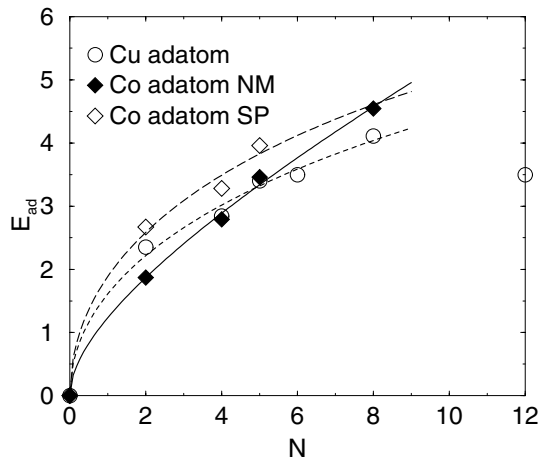
Adatom at:	N	$E_{\text{ad}}^{\text{Cu}}$ [eV]	$E_{\text{ad}}^{\text{CoNM}}$ [eV]	$E_{\text{ad}}^{\text{CoSP}}$ [eV]
bridge site on Cu(001)	2	2.35	1.87	2.67
fourfold hollow site	4	2.84	2.79	3.28
[110]/{111} step	5	3.40	3.46	3.96
kink site at a [110]/{111} step	6	3.50		
substitutional site on Cu(001)	8	4.11	4.54	

Table 6.3: DFT-GGA adsorption energy of Cu ($E_{\text{ad}}^{\text{Cu}}$) and Co adatoms (nonmagnetic $E_{\text{ad}}^{\text{CoNM}}$ and spin-polarized $E_{\text{ad}}^{\text{CoSP}}$) at different adsorption sites on the clean and stepped Cu(001)-surface where N is the adatom's coordination number.

on N , i.e. breaking Co-Cu bonds costs much more energy than breaking Cu-Cu bonds. However, it is at first sight surprising that the adsorption energy for a nonmagnetic Co adatom $E_{\text{ad}}^{\text{CoNM}}$ is slightly lower than $E_{\text{ad}}^{\text{Cu}}$ at the fourfold hollow site on the flat Cu(001) surface. This would apparently contradict the trend that cobalt builds stronger bonds compared to copper. However, the reason is that for Co we use the energy of the spin-polarized atom as a reference energy to calculate the adsorption energy of a nonmagnetic system. The corresponding energies for the spin-polarized systems are indeed higher than $E_{\text{ad}}^{\text{Cu}}$. The energy gain due to spin-polarization decreases with increasing N : *e.g.* it is 0.80 eV for Co at the bridge site, 0.50 for the fourfold hollow site, and 0.40 eV for an adatom at a Cu step.

In a bond-cutting model [108, 109, 144] the total energy of the system can be described as a sum of the contributions of the individual atoms $E = \sum_I E^I$, with $E^I = E_0^I + A^I \sqrt{N^I} + B^I N^I$, where N^I and E_0^I are the coordination number and the energy of the free atom I . In fact the bond-cutting model can be regarded as a simplified version of the effective medium theory or embedded atom method. Here we would like to test whether the adsorption energy can be described with an even simpler model, where we consider only the contribution of the adatom to the adsorption energy and neglect the contribution of the substrate atoms. The adsorption energy is the difference between the total energies of the adsorbate and the reference system (*e.g.* flat Cu(001) surface) and the free atom. Thus the main contribution to E_{ad} comes indeed from the bonds the adsorbate builds with the substrate while the contribution of the substrate atoms, whose coordination number is already high (*e.g.* eight for a surface atom on the flat Cu(001) surface) and changes only by one, is comparatively small. Therefore, we would like to check the possibilities and limitations of such a model.

A least squares fit to the DFT-GGA values of the adsorption energies of Cu, nonmagnetic and spin-polarized Co with a functional form $E_{\text{ad}}^I = C^I + A^I \sqrt{N} + B^I N$



	$E_{\text{ad}}^I = C^I + A^I\sqrt{N} + B^I N$		
I	A^I	B^I	C^I
Cu	1.684	-0.093	0.020
Co-NM	1.030	0.208	-0.003
Co-SP	2.018	-0.139	0.009

Figure 6.3: Adsorption energy in eV of Cu and Co adatoms (non-magnetic and spin-polarized) on different adsorption sites on the clean and stepped Cu(001) surface as a function of the coordination number N . The results of a least squares fit to a function of the form $E_{\text{ad}}^I = C^I + A^I\sqrt{N} + B^I N$ is represented by a dashed line for Cu, solid line for Co (nonmagnetic), and long dashed line for Co (spin-polarized) and the parameters A^I , B^I , and C^I are given in the table to the right.

was performed, with $I = \{\text{Co}, \text{Cu}\}$ and N being the coordination number of the corresponding adatom. The adsorption energies from Table 6.3 as a function of N and the fitted curves are plotted in Fig. 6.3 and the parameters from the fit A^I , B^I , and C^I are given in the table in Fig 6.3. Indeed, the dependence of E_{ad} on N can be well described by a square root function. This explains to a certain extent why there is a very good agreement between DFT-GGA adsorption energies for Cu and results from EAM calculations: Liu [28] obtained 2.39 eV and 2.85 eV for the adsorption at a bridge and fourfold site on the flat Cu(001) surface, respectively, 3.23 eV at the $[110]/\{111\}$ step and 3.54 eV at a kink site. However, our model bears certain limitations, *e.g.* the adsorption energy for Cu at a kink site ($N = 6$) and in bulk ($N = 12$) both equal the cohesive energy, thus the latter point does not lie on the fitted curve. We conclude, that such a model can be useful especially for smaller N ($N \leq 8$), however for larger N the error introduced by neglecting the contributions of the substrate atoms becomes significant.

6.3.2 Structural properties

The relaxations of the atoms in the systems with a Cu or Co adsorbed at a $[110]/\{111\}$ step are given in Table 6.4. A side and top view of the adsorbate systems is shown in Fig. 6.4 together with the atom displacements indicated by arrows. While the vertical relaxation of the surface atoms (2, 3, 8, and 9) of -3%

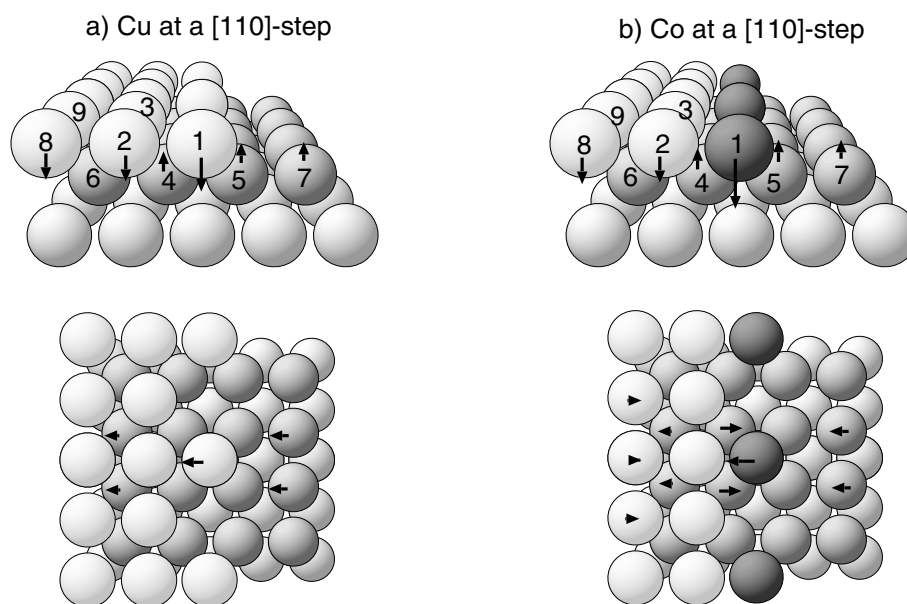


Figure 6.4: Side and top view of a Cu (a) and Co (b) adatom adsorbed at a $[110]$ -step. The arrows indicate the displacements of the atoms with respect to the unrelaxed geometry. The exact values of the displacements are given in Table 6.4.

does not change due to the adsorption of the adatom, the adatom relaxes stronger towards the surface, -4.5% for Cu and -11.7% for Co. The value for Co is more than twice as high than for Cu, reflecting the stronger tendency of Co to enhance its effective coordination at lower coordinated adsorption sites. The substrate atoms from the lower terrace relax slightly outwards similar to the ones in the clean $[110]/\{111\}$ step. The adsorbate relaxes laterally towards the step, Cu by 0.052 bohr and Co almost three times stronger by 0.142 bohr. Concerning the lateral relaxations of the substrate atoms the effects are again stronger in the case of Co adsorption: While the adatoms at the step edge have zero lateral relaxation, atoms 8 and 9 relax towards atoms 2 and 3 and the subsurface atom 6 relaxes in direction of atoms 8 and 9. The step bottom atom 4 relaxes towards the Co adatom and its lateral displacement is stronger than the one prior to adsorption, 0.045 bohr compared to 0.031 bohr, respectively. The shortest bond is between the adatom and the step bottom atom 4, it is reduced by 3.4% and 7.5% compared to d_{bulk} for Cu and Co, respectively. These bond lengths are similar to the ones of adatoms on the flat Cu(001) surface, -4.4% (Cu) and -7.9% (Co).

	Cu-adatom at a $[1\bar{1}0]$ -step			Co-adatom at a $[1\bar{1}0]$ -step		
	Δx [bohr]	Δy [bohr]	$\frac{\Delta z}{z_0}$ [%]	Δx [bohr]	Δy [bohr]	$\frac{\Delta z}{z_0}$ [%]
Atom 1	-0.053	0.0	-4.5	-0.142	0.0	-11.7
Atom 2	0.0	0.0	-3.0	0.0	0.0	-3.0
Atom 3	0.0	0.0	-3.0	0.0	0.0	-3.0
Atom 4	0.0	0.0	-1.3	0.045	0.0	-1.2
Atom 5	0.0	0.0	-1.2	0.0	0.0	-1.9
Atom 6	-0.009	0.0	0.0	-0.014	0.0	0.0
Atom 7	-0.025	0.0	0.7	-0.033	0.0	0.8
Atom 8	0.0	0.0	-3.0	0.007	0.0	-2.9
Atom 9	0.0	0.0	-3.0	0.015	0.0	-2.9

Table 6.4: Lateral relaxations Δx and Δy in bohr and relaxation of the interlayer spacing with respect to the interlayer spacing in Cu bulk z_0 in % of Cu and Co adatoms adsorbed at a close packed step along the $[110]$ -direction. The numbering of the atoms corresponds to the one in Fig. 6.4.

	Cu-adatom at a $[1\bar{1}0]$ -step		Co-adatom at a $[1\bar{1}0]$ -step	
	[bohr]	$\frac{d_{ij}-d_{\text{bulk}}}{d_{\text{bulk}}}$ [%]	[bohr]	$\frac{d_{ij}-d_{\text{bulk}}}{d_{\text{bulk}}}$ [%]
d_{12}	4.83	-1.1	4.75	-2.7
d_{14}	4.71	-3.4	4.51	-7.5
d_{15}	4.77	-2.2	4.64	-5.0
d_{34}	4.77	-2.2	4.77	-2.3

Table 6.5: Bond lengths and deviations from the bond length in Cu bulk d_{bulk} in % of Cu and Co adatoms adsorbed at a close packed step along the $[110]$ -direction. The numbering of the atoms corresponds to the one in Fig. 6.4.

6.4 Diffusion of Co and Cu adatoms along steps

As mentioned at the beginning of this Chapter the adatom diffusion along steps determines the roughness of the steps and the shapes of islands. Diffusion along the $[110]/\{111\}$ steps on a fcc (001) surface proceeds by hopping, *i.e.* the adatom moves from the fivefold coordinated adsorption site over a fourfold coordinated bridge site into the next adsorption site.

6.4.1 Diffusion barriers

The DFT-GGA-barrier for adatom diffusion along a $[110]/\{111\}$ step on the Cu(001) surface is 0.40 eV for Cu, 0.72 eV for a nonmagnetic Co adatom. Both values are

lower than the ones for hopping diffusion on the flat Cu(001) surface, *e.g.* by 0.09 eV for Cu and by 0.20 eV for Co. The lower diffusion barrier at a step can be explained by the smaller variation of the coordination between transition and initial state which is four and five at the step compared to two and four on the flat surface.

The smaller change in the coordination between transition and initial state is also the reason why spin-polarization does not lead to such a strong reduction of the barrier as in the case of terrace diffusion for Co. The diffusion barrier of a spin-polarized Co adatom along a $[110]/\{111\}$ step is 0.55 eV, *i.e.* 0.17 eV lower than the nonmagnetic one and only 0.06 eV lower than the barrier for terrace diffusion of a spin-polarized Co adatom, 0.61 eV. The magnetic moment in the initial and bridge site at the step is $1.81 \mu_B$ and $1.88 \mu_B$, respectively.

The lower energy barrier indicates that Cu islands should be compact in the case of Cu selfdiffusion: adatoms reaching a step will certainly be able to diffuse along the step which means that steps should be in local equilibrium, therefore straight steps are expected. In case of Co deposition, however, the situation is more complicated, the diffusion along the step will be quicker than the one on the flat surface but the barrier is still 0.15 eV higher than the corresponding diffusion barrier of Cu. Therefore a certain roughening of the Cu steps is expected after Co deposition. STM images indeed show straight step bunches along the $[1\bar{1}0]$ -direction for the clean surface and roughened steps after deposition of 0.13 ML of Co at 370 K [143].

The barriers Yu and Scheffler [31] obtained with DFT-GGA for Ag selfdiffusion via hopping on the flat Ag(001) surface and along a step are 0.45 eV and 0.27 eV, respectively. The diffusion barrier along the step was calculated for a (115)-surface which is vicinal to the (100)-surface. In an EAM calculation Tian and Rahman [135] used also a vicinal surface, (117) and determined the diffusion barrier of Cu on the flat terrace and along the step to be 0.49 eV and 0.26 eV, respectively. Similar values were obtained in another EAM study by Liu [28], 0.45 eV and 0.27 eV, respectively. While the agreement between the present DFT-GGA results and the EAM calculations is very good for the Cu diffusion barrier on the flat terrace, the DFT-GGA barrier is 0.13 eV higher than the EAM value. It turns out that not the transition state but the adsorption energy at the initial state is the source of this difference. As mentioned in the previous Section, E_{ad} from EAM [28] is 3.23 eV while the DFT-GGA result is 3.40 eV. On the other hand, using the parameters from the least squares fit to $E_{ad}^I = C^I + A^I \sqrt{N} + B^I N$, a value of 3.32 eV is obtained which lies between the EAM and DFT-result. The slightly higher DFT-GGA adsorption energy may be attributed to a size effect: due to the high numerical cost the DFT-calculations were performed in a (4×2)

unit cell, whereas the EAM calculations were performed on a vicinal surface with comparably broad terraces. While a possible step-step interaction cancels out when subtracting the adsorption energies of the transition and initial state, a non-vanishing interaction of the adatom with the step in the next cell might play a bigger role for the initial state than the transition state thus influencing the diffusion barrier. An indication that supports this assumption is the fact that the adatom relaxes laterally much stronger towards the step it is attached to at the bridge site than at the adsorption site, thus the distance to the step edge of the next cell is smaller for the latter.

6.4.2 Structural properties

The transition state for diffusion along the $[110]/\{111\}$ step was determined by moving the adatom along the step to the bridge site and then relaxing the x (perpendicular to the step edge) and z -component of the adatom as well as both the lateral and vertical components of the step and surface atoms.

The lateral and vertical displacements of the atoms at the transition state of hopping diffusion of Co and Cu along the $[110]/\{111\}$ step are given in Table 6.6 and a top and side view of the adsorbate systems together with the displacements of the individual atoms are shown in Fig. 6.5. The Cu adatom is situated 3.80 bohr above the terrace which is close to the value at the bridge site on the flat

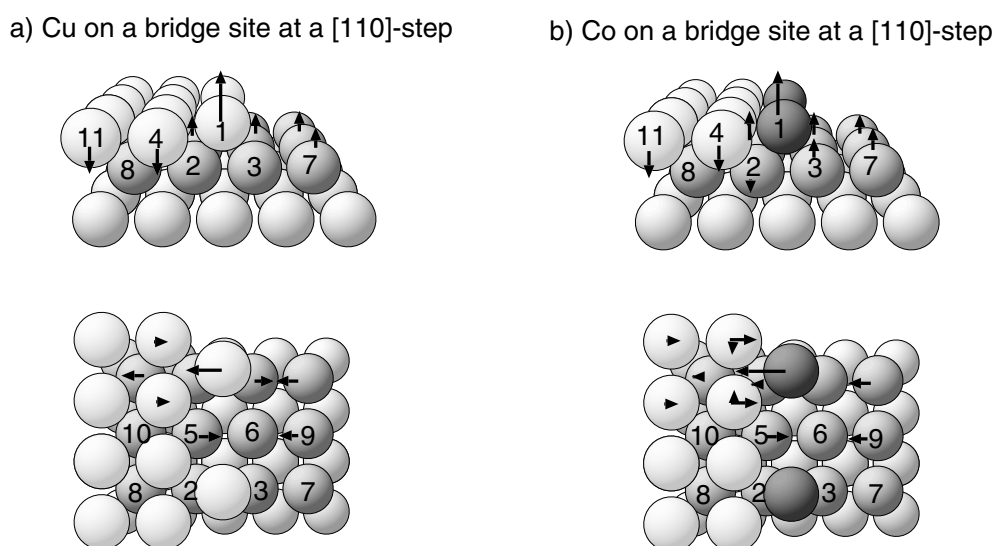


Figure 6.5: Side and top view of a Cu (a) and Co (b) adatom at a bridge site at a $[1\bar{1}0]$ -step. The arrows indicate the displacements of the atoms with respect to the unrelaxed geometry. The exact values of the displacements are given in Table 6.6.

Cu(001) surface, 3.78 bohr. The Co adatom lies slightly lower, 3.74 bohr, while the corresponding value at the flat surface is 3.67 bohr. The most pronounced effect is the relaxation of the adatom towards the step edge by 0.153 bohr and 0.243 bohr for Cu and Co, respectively. We note that the lateral displacement of the adatom at the adsorption site at the step is in the same direction, but approximately three times smaller for Cu and two times smaller for Co. The bond length between the adatom and the step atom 4 is 9.2% and 5.8% longer than d_{bulk} for Cu and Co, respectively. While in the initial state of hopping diffusion along the $[110]/\{111\}$ step the step bottom atom 2 relaxes slightly outwards it now takes the ideal position z_0 for Cu or even relaxes slightly inwards by 0.9% for Co thus allowing the adatom in the bridge site to shift laterally towards the step. The shortest bond is the one between the adatom and the step bottom atom 2 and its length is reduced compared to d_{bulk} by 9.1% and 10.5% for Cu and Co, respectively.

	Cu on a bridge site at a $[\bar{1}\bar{1}0]$ -step			Cu on a bridge site at a $[\bar{1}\bar{1}0]$ -step		
	Δx [bohr]	Δy [bohr]	$\frac{\Delta z}{z_0}$ [%]	Δx [bohr]	Δy [bohr]	$\frac{\Delta z}{z_0}$ [%]
Atom 1	-0.153	0.0	10.0	-0.243	0.0	8.3
Atom 2	0.0	0.0	0.0	-0.007	0.0	-0.9
Atom 3	0.033	0.0	0.0	0.0	0.0	0.6
Atom 4	0.005	0.004	-2.8	0.088	0.006	-2.0
Atom 5	0.037	0.0	-1.2	0.0	0.0	3.8
Atom 6	0.0	0.0	2.0	0.053	0.0	0.0
Atom 7	-0.041	0.0	1.5	-0.038	0.0	1.3
Atom 8	-0.023	0.0	0.0	0.010	0.0	0.0
Atom 9	-0.036	0.0	1.7	-0.018	0.0	0.9
Atom 10	0.0	0.0	0.0	0.0	0.0	0.0
Atom 11	0.0	0.0	-3.0	0.012	0.0	-3.0

Table 6.6: Lateral relaxations Δx and Δy in bohr and relaxation of the interlayer spacing with respect to the interlayer spacing in Cu bulk z_0 in % of Cu and Co adatoms adsorbed on a bridge site at a close packed step along the $[110]$ -direction. The numbering of the atoms corresponds to the one in Fig. 6.5.

6.5 Onset temperature for diffusion

The calculated DFT-GGA diffusion barriers are used in the next Chapter as input parameters for a kinetic Monte Carlo (KMC) simulation to describe homo- and heteroepitaxial growth. However, a qualitative estimation of the growth mode can be obtained already from the relative positioning of the different processes with

	Cu on a bridge site at a $[1\bar{1}0]$ -step		Co on a bridge site at a $[1\bar{1}0]$ -step	
	[bohr]	$\frac{d_{ij}-d_{\text{bulk}}}{d_{\text{bulk}}} [\%]$	[bohr]	$\frac{d_{ij}-d_{\text{bulk}}}{d_{\text{bulk}}} [\%]$
d_{12}	4.43	-9.1	4.37	-10.5
d_{13}	4.62	-5.4	4.58	-6.1
d_{14}	5.33	9.2	5.16	5.8

Table 6.7: Bond lengths and deviations from the bond length in Cu bulk d_{bulk} in % of Cu and Co adatoms of Cu and Co adatoms adsorbed on a bridge site at a close packed step along the $[110]$ -direction. The numbering of the atoms corresponds to the one in Fig. 6.5.

respect to the barrier height and the onset temperature. The onset temperature T_i is defined as the temperature at which the process i is activated. It is typically assumed that this is the case when process i takes place at least once per second, *i.e.* at a rate $\Gamma = 1 \text{ s}^{-1}$. T_i can be determined from equation Eq. 5.1:

$$T_i = \frac{E_d^i}{k_B \ln(\Gamma_0/\Gamma)} \quad (6.1)$$

Typically the same value for Γ_0 is used for all microscopic processes. However, Boisvert and Lewis [111] recently found from a molecular dynamics embedded atom method (MD-EAM) simulation that the prefactors Γ_0 for the hopping and exchange process of Cu on the flat Cu(001) surface differ by a factor of 20, $\Gamma_0^h = 2 \times 10^{13} \text{ s}^{-1}$ and $\Gamma_0^{ex} = 4.37 \times 10^{14} \text{ s}^{-1}$.¹ Therefore, these values are used in the following for the estimation of the activation temperature both for Co and Cu. The diffusion barriers and the corresponding activation temperatures are displayed in Table 6.8.

	Process	E_{ad} [eV]	T [K]
Cu	hopping along $[110]$ -step	0.40	152
	hopping on flat Cu(001)	0.49	186
	exchange on flat Cu(001)	1.02	352
Co	hopping along $[110]$ -step	0.55	208
	hopping on flat Cu(001)	0.61	231
	exchange on flat Cu(001)	1.00	344

Table 6.8: Barriers and the corresponding onset temperatures for different microscopic processes of Cu and Co adatoms (spin-polarized) on the flat and stepped Cu(001)-surface.

For homoepitaxial growth of Cu(001) terrace diffusion is activated well below room temperature. Adatoms attached at steps should be able to diffuse along

¹In agreement with this finding Liu *et al.* [145] obtained with EAM a much higher pre-exponential factor for exchange than for hopping for other (001) metal surfaces (*e.g.* for Al and Pt).

them even before adatom diffusion on the flat terrace is being activated. Thus steps are likely to have smooth edges above 150 K. However, on the flat terrace adatoms would be immobile below 190 K and no islands are likely to form at such temperatures. Indeed, Dürr *et al.* [140] observed no compact island formation below 150 K which indicates that adatom diffusion is hindered at this temperature. Breeman and Boerma [139] determined the onset temperature of adatom diffusion from LEIS measurements to be 140 K, which is in good agreement with our result. Exchange diffusion does not play an important role for Cu selfdiffusion because it is activated at very high temperatures at which the rate for adatom diffusion via hopping is already $1.9 \times 10^7 \text{ s}^{-1}$.

For the heteroepitaxial growth of Co on Cu(001) terrace diffusion starts at higher temperatures than for Cu, namely above 230 K. At room temperature and for a low deposition rate adatom mobility would be high enough to form small compact islands. The exchange process of Co is activated at approximately 350 K. Thus, below this temperature no intermixing is expected and island nucleation will very much resemble the homoepitaxial case, with the only difference that the adatoms are less mobile than in the homoepitaxial case. However, annealing above 400 K may change substantially the picture. At that temperature a substantial amount of Co will exchange. The kicked out Cu atoms would diffuse at a much higher rate on the terrace than the Co atoms until they reach an already existing Cu island or form new islands which are pinned at an incorporated Co atom. Surely, in order to get a detailed picture of heteroepitaxial growth a large number of additional processes needs to be studied. However, even on the basis of the processes presented in this study some important features of the initial growth mode can be identified.

Chapter 7

Kinetic Monte Carlo simulations of growth

In this Chapter after a short review on the most important methods used to study growth phenomena the main features of the KMC method are discussed. Some issues on its implementation in the computer code in particular with respect to the description of heteroepitaxial growth are addressed in Section 7.1. In Section 7.2 island morphologies and scaling properties for the submonolayer growth of Cu on Cu(001) obtained from DFT-KMC simulations are studied and compared to previous simulations based on EAM barriers. Additionally, results for some simple models describing the dependence of the diffusion barrier on the local environment are discussed, *e.g.* “hit & stick”- and bond-cutting models. In Section 7.3 the initial growth of Co on Cu(001) is studied. Island morphologies are compared to the homoepitaxial case (Cu on Cu(001)) and deviations from the predictions of standard nucleation theory are discussed. The results are summarized in Section 7.4.

7.1 General remarks on growth simulations

7.1.1 Comparison between MD, rate equations, and MC

Different approaches have been used in the past to model the time evolution of a surface. In molecular dynamics (MD) the motion of the particles is described by Newton’s equation of motion:

$$m_i \ddot{\mathbf{R}}_i = -\nabla_i V(\{\mathbf{R}_i\}), \quad \text{where } \{\mathbf{R}_i\}, (i = 1, \dots, N). \quad (7.1)$$

For a given interatomic potential $V(\{\mathbf{R}_i\})$ this approach represents an exact treatment of the time evolution of the system. The motion of single particles on the

surface can be treated exactly by Newton's equation of motion. However, the size of the system as well as the short time scales¹ represent a limitation for this approach. Thus the main field of application of MD is in determining possible processes, probable paths, diffusion barriers and prefactors.

Another approach is the phenomenological description of growth with rate equations as introduced by Venables [33]. The rate equations give the time evolution of the adatom and island density.

$$\frac{dn_1}{dt} = F - \frac{n_1}{\tau_a} - \frac{d(n_x w_x)}{dt} \quad (7.2)$$

$$\frac{dn_x}{dt} = U_i - U_c - U_m. \quad (7.3)$$

The concentration of monomers n_1 increases due to deposition with a rate F . However, adatoms are lost due to desorption $\frac{n_1}{\tau_a}$ or captured by islands $\frac{d(n_x w_x)}{dt}$. Under the assumption that all islands below a critical size i are unstable and their concentration is in equilibrium, the density of stable islands n_x is augmented due to formation of new stable nuclei U_i but decreases due to coalescence of stable nuclei U_c or island migration U_m . U_i corresponds to the nucleation rate J which is proportional to the product of the diffusion constant D , the density of adatoms n_1 , and of stable islands n_x . Neglecting long jumps the diffusion constant is given by:

$$D = D_0 e^{-\frac{E_d}{k_B T}} \quad \text{with} \quad D_0 = \frac{1}{4} \Gamma_0 l^2. \quad (7.4)$$

Thus the diffusion constant differs from the diffusion rate Γ defined in Eq. 5.1 by a factor of $\frac{1}{4}l^2$, where l is the length of the diffusion step. At not too high temperatures when the desorption rate is negligible (regime of complete nucleation [33]) a simple relation holds for the saturation island density: $n_x \propto (F/D)^p$. For nucleation of two dimensional islands $p = i/(i + 2)$. Thus nucleation theory provides a relation between island density, deposition rate, and temperature which is often used to extract information from experimental data: *e.g.* determine the critical island size i from the deposition rate dependence of the island density at constant temperature or the diffusion barrier from the dependence of the island density on temperature at a constant rate (Arrhenius plot). However, the rate equations express the time evolution of the *average* adatom and island density. As a *mean-field* approach it assumes that the adatom density takes a constant value immediately outside the islands while in reality there is a "depletion zone" around the islands. These features are the reason why island size

¹Typical time scales for MD simulations are of the order of a picosecond while the time scales of growth phenomena are of the order of microseconds (formation of small islands) to seconds (formation of mesoscopic and macroscopic structures).

distributions obtained from rate equations are not correct. As recently shown in a DFT-KMC-study [37], for systems where medium-range interactions are important (*e.g.* on strained surfaces) island densities predicted from nucleation theory where only short range interactions are considered can differ by as much as an order of magnitude.

On the other hand in the framework of statistical mechanics not the exact motion of a particle is relevant: motion is treated as random, while the probability as a functional of the energy of a particular configuration of the system is exact. A method that bridges the gap between MD and rate equations and makes a description of large systems on long time scales possible, taking into account the microscopic information about the relevant processes, is the *kinetic Monte Carlo* method. The latter is based on several geometric and dynamic assumptions which will be sketched in the following. For further details we refer the reader to the review article of Levi and Kotrla [146] and references therein.

7.1.2 Geometric and dynamic assumptions of the MC method

Growth simulations are based on *discrete* models, *i.e.* particles can occupy discrete positions on a lattice. Each site can be occupied or vacant. Regions of high concentration correspond to the solid and regions of low concentration correspond to “the vapor”. An obvious choice for the lattice in this so-called *lattice gas* model is a lattice corresponding to the symmetry of the studied material. However, often a square lattice is taken as is the case for the initial stages of homoepitaxial growth of Cu on Cu(001) which will be described in Section 7.2. On the other hand, in the case of heteroepitaxial growth of Co on Cu(001), growth simulations need to be performed on a fcc-lattice in order to account correctly for the chemical composition of the substrate and of the first layer which is altered due to the exchange processes. Details on the implementation of a fcc lattice will be presented in Section 7.3. A further approximation to the lattice gas model is that processes inside the gas phase are neglected and additional atoms are added to the system according to growth rules (deposition rate). Such a model is justified for ballistic deposition as in molecular beam epitaxy (MBE). Additionally the so-called solid-on-solid (SOS) approximation is used for which the formation of vacancies and overhangs is avoided, *i.e.* each adatom sits on another atom.

In the Monte Carlo method dynamics on a short time scale like the vibrations of an adatom at an adsorption site are neglected (thermodynamic MC) or considered implicitly (kinetic MC). It is assumed that motion takes place instantaneously and events are independent (Markovian).

7.1.3 Thermodynamic versus kinetic Monte Carlo

The Monte Carlo method can be regarded as a method for solving the *Master equation* which gives the time evolution of the probability $P(\mathcal{C}, t)$ of a certain configuration \mathcal{C} from the configurational space $\mathcal{S} = \{\mathcal{C}\}$

$$\frac{dP(\mathcal{C}, t)}{dt} = - \sum_{\mathcal{C}'} W(\mathcal{C} \rightarrow \mathcal{C}') P(\mathcal{C}, t) + \sum_{\mathcal{C}'} W(\mathcal{C}' \rightarrow \mathcal{C}) P(\mathcal{C}', t), \quad (7.5)$$

where $W(\mathcal{C} \rightarrow \mathcal{C}')$ describes the transition probabilities connecting two states. The condition of *detailed balance* ensures that the systems converges towards equilibrium:

$$W(\mathcal{C} \rightarrow \mathcal{C}') P(\mathcal{C}, t) = W(\mathcal{C}' \rightarrow \mathcal{C}) P(\mathcal{C}', t). \quad (7.6)$$

It means that in thermal equilibrium the rates of opposite processes, *e.g.* the formation and decay of clusters are equal. Depending on the form chosen for the transition probability one distinguishes between *thermodynamic* and *kinetic* Monte Carlo. A frequently used form of the former class is *e.g.* the one defined by Metropolis *et al.* [147]:

$$W(\mathcal{C} \rightarrow \mathcal{C}') = \begin{cases} e^{-\frac{\Delta E}{k_B T}} & \text{if } \Delta E = E_{\mathcal{C}'} - E_{\mathcal{C}} \geq 0 \\ 1 & \text{if } \Delta E < 0. \end{cases} \quad (7.7)$$

In this formulation a transition between two configurations takes place with certainty if the energy of the final configuration \mathcal{C}' is lower than the one of the initial configuration \mathcal{C} or with a probability $e^{-\frac{\Delta E}{k_B T}}$ in the opposite case. The Metropolis algorithm converges towards the thermodynamic equilibrium configuration but the sequence of configurations does not correspond to the dynamic behavior of the system.

The idea to combine the lattice gas model with an interatomic potential in order to describe the stochastic evolution of a many-body system was proposed by Voter [148] and further developed by Khang and Weinberg [149] as well as Fichthorn and Weinberg [150]. The basic concept of the *kinetic* Monte Carlo (KMC) method is that the different processes (*e.g.* deposition, diffusion, desorption) are described by rates $\Gamma^j = \Gamma_0^j e^{-\frac{E_d}{k_B T}}$. If N different processes (events) are possible in a configuration \mathcal{C} then the total rate is given by $Q(\mathcal{C}) = \sum_{j=1}^N \Gamma^j m^j$ where m^j is the multiplicity of a particular process (*e.g.* for deposition it is equal to the number of vacant sites on the lattice). The transition probability can be written as

$$W(\mathcal{C} \rightarrow \mathcal{C}') = \sum_{j=1}^N \Gamma^j V^j(\mathcal{C} \rightarrow \mathcal{C}'), \quad (7.8)$$

where $V^j(\mathcal{C} \rightarrow \mathcal{C}')$ is a stochastic matrix element which shows whether the transition $\mathcal{C} \rightarrow \mathcal{C}'$ is possible through event j . As discussed in the previous Chapter the diffusion barrier E_d can be obtained within transition state theory (TST) as the difference between a metastable (saddle point) and a stable (adsorption site) configuration while the information on the vibrational frequencies in the initial and transition state is contained in the prefactor Γ_0 . Two aspects have to be mentioned here: in order to make the task feasible one often has to select a finite number of processes for the model. Typically, the processes assumed to be relevant for the studied phenomena are considered. However, often KMC-simulations include only several basic processes like deposition, diffusion, and desorption or combine different atomistic processes with similar barriers into classes. The second problem concerns how the rates are determined. Usually they are guessed or effective parameters are used obtained by fitting to experimental quantities or using semiempirical methods. However, there is no unambiguous correspondence between such parameters and the microscopic processes, *e.g.* different sets of parameters can reproduce the experimental results. Only recently it has become feasible to extract highly accurate diffusion barriers from DFT-calculations. Such parameters were used successfully to investigate island forms and orientation for the homoepitaxial growth of Al on Al(111) [34, 36] and recently for the growth of compound semiconductors (GaAs) [38]. Our aim is to study the initial growth of Co on Cu(001) using DFT-GGA barriers as input parameters to a KMC simulation.

7.1.4 Implementation - the N -fold method

In conventional KMC simulations first a particular type of event is selected then a random number is generated which is compared to the probability of the selected event. The chosen event does not take place unless its probability is larger than the selected random number. This model results in a large number of unsuccessful events especially for low probability processes.

The implementation used in the present study is based on the general method of Fichthorn and Weinberg [150] and is similar to the so called N -fold method which was initially formulated for the Ising model [151] and later used in KMC [152]. Here, in contrast to the standard implementation of KMC events are selected with a probability proportional to their physical rate. Thus the problem of choosing unsuccessful events is avoided.

A schematic representation of the k . simulation step is shown in Fig. 7.1. A random number is generated in the interval defined by the sum of the rates of the different processes Γ^J times their multiplicity m^j . The type of event, i , is selected

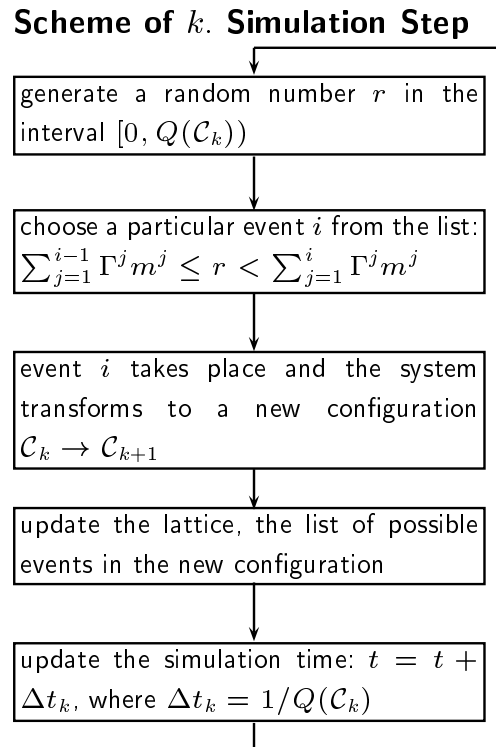


Figure 7.1: Schematic representation of the k . simulation step describing the transition of the system from configuration \mathcal{C}_k to configuration \mathcal{C}_{k+1} .

in whose interval the random number r falls. With a second random number a particular realization of this event is selected from the list which has m^i entries. The system transforms from configuration \mathcal{C}_k to configuration \mathcal{C}_{k+1} . In the new configuration \mathcal{C}_{k+1} the list of possible events as well as their multiplicities have to be updated. However, because an event affects only a small part of the lattice only the immediate environment is considered. A proportionality between real time and the time of the simulation is established by assuming that the time the system spends in the configuration \mathcal{C}_k before an event i takes place is inversely proportional to the total transition rate $Q(\mathcal{C}_k)$ [150, 153]. In case of a constant deposition flux, the flux can be used also as a measure of time.

7.2 Homoepitaxy: Cu on Cu(001)

The KMC-code was first applied for the homoepitaxial growth of Cu on Cu(001). Here the exchange process is practically a motion in $[100]$ -direction while for hop-

ping diffusion the adatom moves between adjacent sites in $[110]$ - or $[1\bar{1}0]$ -direction. Therefore growth can be modeled on a square lattice. A simulation cell of 128×128 was used. Some results were checked for a bigger cell, 256×256 , to ensure that relevant quantities are independent of the system size. The atoms are deposited randomly on the lattice. The DFT-GGA barriers for hopping and exchange diffusion, 0.49 eV and 1.02, respectively, are used as well as the prefactors obtained from an EAM-MD-study [111], $\Gamma_0^h = 2 \times 10^{13} \text{ s}^{-1}$ and $\Gamma_0^{ex} = 4.37 \times 10^{14} \text{ s}^{-1}$. An adatom diffuses towards a step, *i.e.* from an initial coordination² $N_i = 0$ to a final coordination $N_f = 1$, with the same barrier as for terrace diffusion. In order to study the effect of edge diffusion on island morphology we have included also the diffusion barrier along a step which is lower than the one on the terrace, 0.40 eV. Reaching an island corner the adatom can turn around the corner via exchange with a barrier of 0.7 eV. An adatom can also break from a dimer or diffuse from ledge to terrace with a diffusion barrier of 0.86 eV [28]. However, for the temperature range studied here this process, as well as exchange on the terrace did not play a role. Diffusion of adatoms that have at least two neighbors is neglected. In fact the barrier for an adatom to move away from a twofold coordinated site, *e.g.* from kink to terrace, is very high, 0.87 eV, as found from EAM-calculations [28] and thus the process should not be relevant for the temperature range studied here.

7.2.1 Island morphology

Figure 7.2 contains pictures of the island morphology for three different temperatures after deposition of 0.1 ML Cu on Cu(001) at a rate $F = 0.01 \text{ ML/s}$. At 170 K

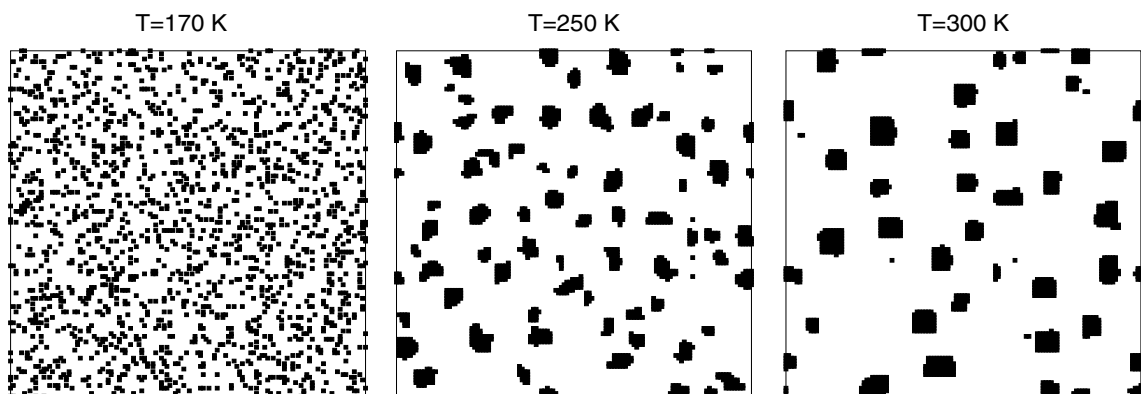


Figure 7.2: Snapshots of homoepitaxial growth of 0.1 ML Cu on Cu(001) at different temperatures and a deposition flux of 0.01ML/s.

the adatom mobility is very low therefore, after deposition of 0.1 ML of Cu, the

²Here, coordination number refers only to the number of nearest neighbors in the first layer.

adatom density is high and there are also a few islands containing only several atoms. At 250 K deposited adatoms are already quite mobile. Small compact islands form with a preferential orientation of the edges along the $[110]$ - and $[1\bar{1}0]$ -direction but also a noticeable amount of kinks. The island morphology is in good agreement with the results from a recent KMC simulation for the growth of Cu on Cu(001) based on barriers obtained with EAM [154]. At room temperature larger compact islands form with square or rectangular shape and edges along the $[110]$ - and $[1\bar{1}0]$ -direction. Both the mean size of the islands and the mean island separation grows with temperature as a result of the higher diffusion rate.

7.2.2 Adatom and island density, scaling properties

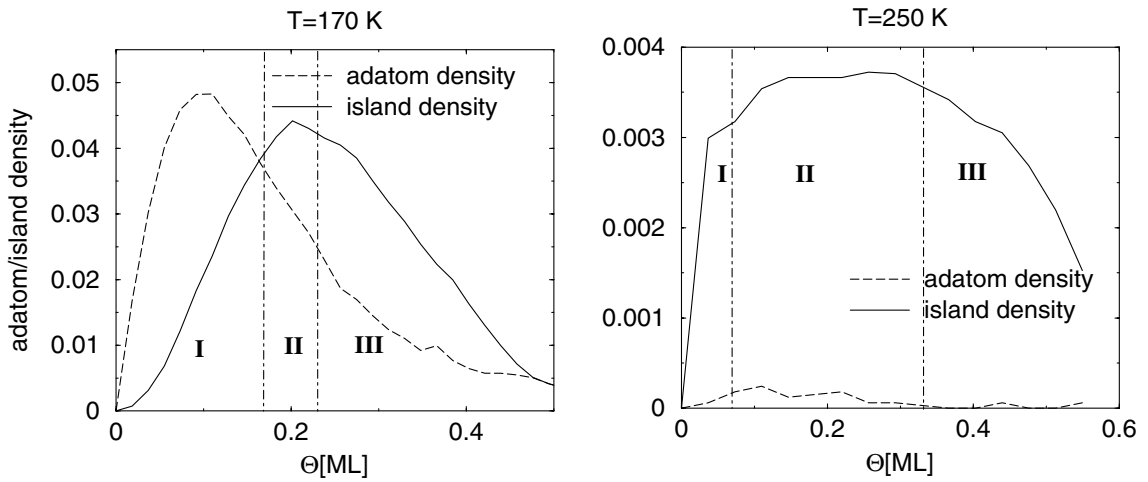


Figure 7.3: The adatom and island density during growth of Cu on Cu(001) as a function of coverage for two different temperatures: 170 K (left panel) and 250 K (right panel).

The evolution of island and adatom density with growing coverage is presented in Fig. 7.3. The typical behavior known from standard nucleation theory is observed for $T = 170$ K: In the *nucleation* regime the adatom density increases due to the incoming flux. Yet with growing coverage there is a higher probability that adatoms meet and form islands, therefore at a certain point the adatom density starts to decrease. The number of adatoms that meet and form stable nuclei increases linearly until their concentration becomes equal to the concentration of adatoms. From this point on the probability of arriving atoms to attach to already existing islands becomes comparable to the probability to meet another adatom and form a new nucleus. The *nucleation* regime is followed by the so called *steady state* regime where the island density saturates and practically all new adatoms are captured by already existing islands. At a coverage close to 0.3 ML island

density starts to decrease due to island coalescence. We note that at this low temperature because of the high island density the island separation is small and islands start to touch already at very low coverages. For deposition at higher temperatures, *e.g.* 250 K, due to the higher diffusion rate adatoms meet almost immediately other adatoms to form stable nuclei or attach to existing islands, thus the adatom density is very low for all coverages. We note that the region of saturated island density is much larger than for the lower temperature and island coalescence starts above 0.4 ML.

In the *steady state* regime rate equations show that the island density depends on the ratio of the diffusion and deposition rate as $n_x \propto (F/D)^p$ where the critical exponent $p = i/(i+2)$ depends on the size i of the critical nucleus. Typically when the diffusion barrier is determined from experimentally obtained island densities it is assumed that dimers are already stable, *i.e.* $i = 1$. However, EAM results [28, 154, 155] show that small clusters (dimers, trimers) have a similar diffusion barrier as monomers on Cu(001). Therefore, small cluster mobility might influence the scaling properties of the island density. In our study clusters have some mobility, *i.e.* adatoms are allowed to diffuse along island edges and around corners, thus, the center of mass of the island can change. We find that this island mobility does not influence the size of the critical nucleus: for the temperature range studied here $p = 0.314 \pm 0.02$ which essentially corresponds to $i = 1$. A similar result was obtained for the critical exponent by Breeman *et al.* [155] from a EAM-KMC study, $p = 0.35 \pm 0.03$.

The agreement between our simulation and previous KMC simulations based on EAM calculations in island morphology, island density and scaling behavior is surprising. We note that Biham *et al.* [154] considered the occupation of nearest and next nearest neighbor sites in the initial configuration and calculated the barriers for 128 different processes, while Breeman *et al.* [155] took into account both the environment in the initial and final state with 1024 barriers on the whole. The task to obtain such a large number of barriers from DFT-calculations is however not feasible. On the other hand both Biham *et al.* [154] and Breeman *et al.* [155, 156] observed that most of the barriers can be combined into “energy bands” with similar barrier height. A closer analysis showed [156] that these energy bands correspond to several important processes like diffusion along a step, adatom diffusion on a terrace, breaking or formation of a dimer. This offers an explanation why our simulation though containing only several diffusion processes is able to reproduce the main features of the homoepitaxial growth of Cu on Cu(001).

7.2.3 Other models for adatom-adatom interaction

We have also studied several other models to describe the dependence of the diffusion barrier on the local environment and will discuss their properties in the following.

“Hit and stick”-model

The simplest way to account for interatomic interactions is the so called “hit & stick”-mechanism or diffusion limited aggregation (DLA). As the title says, adatoms diffuse on the surface until they meet another adatom or island where they stick irreversibly. This model leads to fractal islands with branches in random directions. Snapshots of the initial growth of 0.1 ML Cu on Cu(001) for three

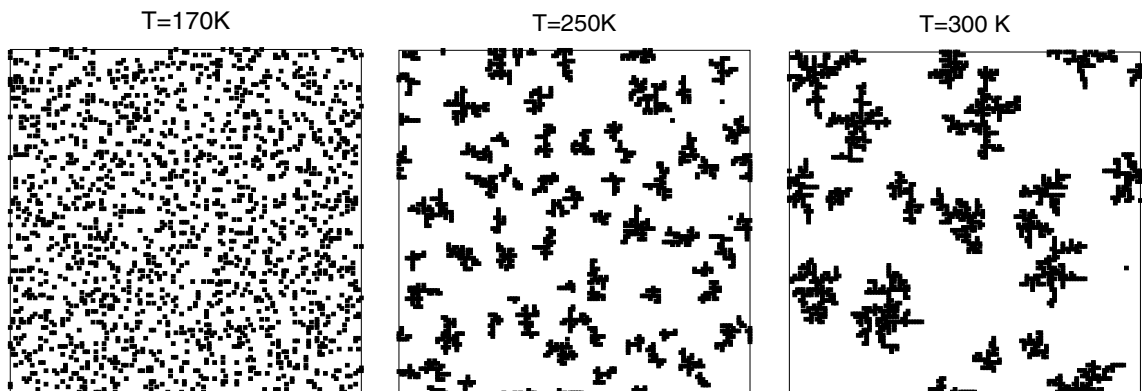


Figure 7.4: Snapshots of homoepitaxial growth of 0.1 ML Cu on Cu(001) at different temperatures and a deposition flux of 0.01 ML/s in the “hit & stick”-mechanism.

different temperatures at a deposition rate of 0.01 ML/s are shown in Fig. 7.4. Several features are correctly reproduced like the fact that island size and the mean island separation grows with temperature. The three growth regimes discussed above, namely *nucleation*, *saturation* and *coalescence*, can be recognized in Fig. 7.7 where the adatom and island density is plotted as a function of coverage. Although some quantities of growth like the adatom and island density are described satisfactorily within the “hit & stick”-model, it fails to give the proper island shape observed from experiment. The main reason is that diffusion along island edges is suppressed while on square lattices this process has a lower barrier than adatom diffusion on the terrace and therefore compact nearly square islands evolve.

Coordination number models

A model frequently used in the literature assumes that the diffusion barrier depends linearly on the number of nearest neighbors in the initial state N_i . Thus the diffusion barrier $E_d = E_d^0 - N_i E_b$ is enhanced by $N_i E_b$ compared to the diffusion barrier of a single adatom on the surface. In contrast to conventional Monte Carlo simulations where for E_d^0 an arbitrary offset value is taken, we use here the barriers from the DFT-GGA calculation. For the parameter E_b a value of -0.1 eV was chosen which describes an attractive interaction between the adatoms and is slightly lower than the value we obtain from DFT-GGA calculations for one half of the binding energy of a Cu dimer on the surface. The results obtained with this

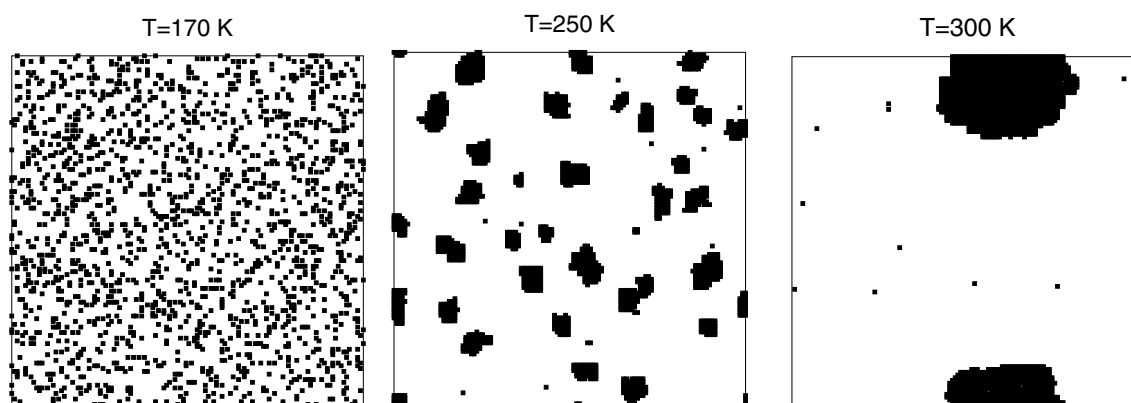


Figure 7.5: Snapshots of homoepitaxial growth of 0.1 ML Cu on Cu(001) at different temperatures and a deposition flux of 0.01 ML/s. The diffusion barrier for hopping and exchange depends on the coordination in the initial state, $E_d = E_d^0 - N_i E_b$, with $E_b = -0.1$ eV.

approach for 0.1 ML Cu on Cu(001) at three different temperatures are shown in Fig. 7.5. This “bond-cutting” model leads to compact islands especially for higher temperatures. Island edges are not always smooth but a preferential orientation along $[110]$ - and $[1\bar{1}0]$ -direction is observed. The roughness of the islands is mainly due to the fact that this model does not properly describe *e.g.* diffusion along a step: here the coordination of surface adatoms in the initial state is one and thus the barrier is enhanced while DFT-results show that it is 0.1 eV lower than the barrier for terrace diffusion.

An improvement to the model presented above is achieved by considering not only the local environment in the initial state but also the one in the final state. In this case the adsorption energy in the initial state depends on the coordination in the initial state, N_i while the adsorption energy in the transition state depends on the coordination both in the initial and final state, N_i and N_f :

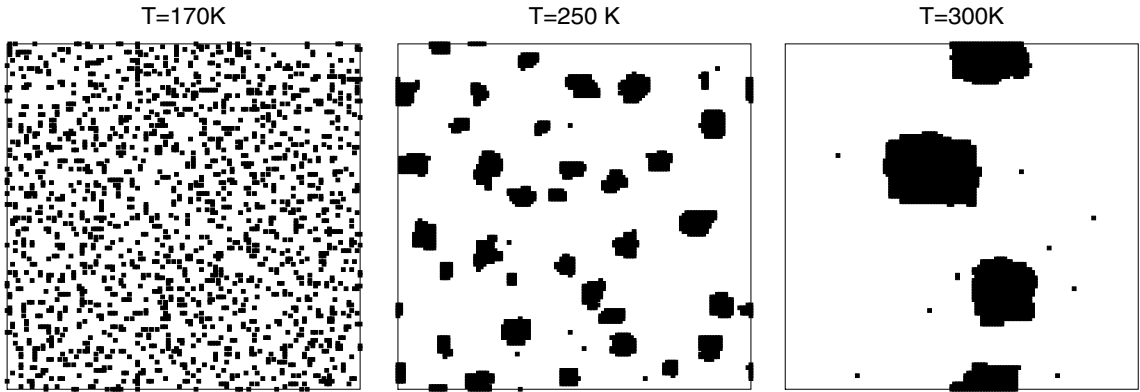


Figure 7.6: Snapshots of homoepitaxial growth of 0.1 ML Cu on Cu(001) at different temperatures and a deposition flux of 0.01ML/s. The diffusion barrier for hopping and exchange depends on the coordination in the initial and final state, $E_d = E_d^0 + \frac{N_f - N_i}{2} E_b$, with $E_b = -0.2$ eV.

$E_{TS} = E_{TS}^0 + \frac{N_f + N_i}{2} E_b$. Thus the diffusion barrier is $E_d = E_d^0 + \frac{N_f - N_i}{2} E_b$. A binding term of -0.2 eV was used in order to have correspondence to the previous model. If both diffusion via hopping and exchange are considered altogether 17 barriers are implemented in the KMC-simulation. We note that in this case $N_i = N_f = 1$ and therefore the diffusion barrier is equal to the the barrier for terrace diffusion.

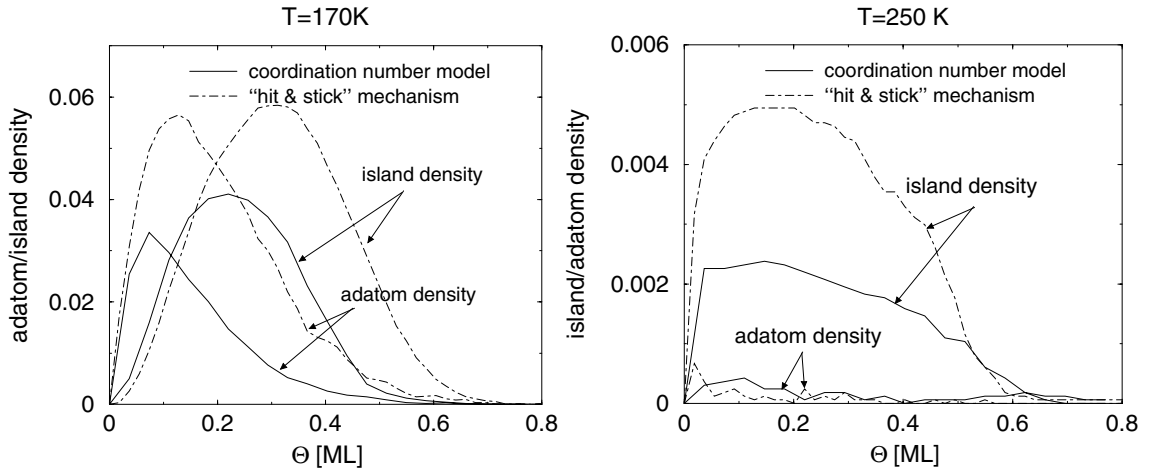


Figure 7.7: The adatom and island density during growth of Cu on Cu(001) as a function of coverage for two different temperatures: 170 K left panel and 250 K right panel. In the coordination number model (solid line) the diffusion barrier for hopping and exchange depends on the coordination in the initial and final state, $E_d = E_d^0 + \frac{N_f - N_i}{2} E_b$, with $E_b = -0.2$ eV. As a comparison the results from a “hit & stick”-model are plotted with a dashed-dotted line.

Snapshots for 0.1 ML Cu on Cu(001) at the same temperature as in the previous cases are displayed in Fig. 7.6. The dependence of the island and adatom density for two different temperatures is plotted in Fig. 7.7. Qualitatively, the coordination number and the “hit & stick”-model give a similar result for the island and adatom density. However, the number of adatoms and islands is higher for the “hit & stick”-model due to the fact that diffusion of already attached atoms is prohibited.

Although the coordination number models presented above are able to reproduce the experimental findings of compact islands for the homoepitaxy of Cu(001), the main deficiency remains, *i.e.* diffusion along the step is still not properly accounted for.

7.3 Heteroepitaxy: Co on Cu(001)

While in the homoepitaxial case initial growth can be simulated on a square lattice and both diffusion mechanisms, hopping and exchange, can be properly accounted for, the situation is more complex in the heteroepitaxial case. An exchange event changes the chemical composition of the substrate and first layer: a Co atom is built in the substrate layer and the kicked out Cu adatom can diffuse further on the surface. Therefore, for a heteroepitaxial system like Co on Cu(001) where exchange events play an important role, the initial growth cannot be simulated on a square lattice. In order to provide a realistic description of the surface morphology and chemical composition both of the substrate and first layer and of relevant processes like exchange of Co atoms and *pinning* at substitutional Co a fcc lattice was implemented. In contrast to the square lattice where every site can be occupied now both in the substrate and first layer only every second site can be occupied:

- substrate layer: all sites (i, j) with $i + j = 2n + 1$ can be occupied. In the initial configuration all sites are occupied by Cu atoms.
- first layer: all sites (i, j) with $i + j = 2n$ can be occupied.

Thus the lattice is rotated by 45° compared to the square lattice used in the previous Section, as will be observed in the snapshots from the simulations.

“Hit and stick”-model

First it was ensured that both the square and fcc lattice give the same results with respect to island shapes and island and adatom density as a function of

coverage in the homoepitaxial case of Cu on Cu(001). In a second step the heteroepitaxial growth of Co on Cu(001) was tested in a “hit & stick”-model where only the barriers for hopping and exchange of Co and Cu adatoms were included. For temperatures above 350 K when exchange diffusion for Co is activated some important features of growth for this system can be observed even in this simple model: due to the high rate of hopping events for Cu the centers of the fractal islands are predominantly built by Cu while Co that has not yet exchanged agglomerates at the edges of the branches.

Coordination number model

The adatom interaction is described in a “bond-cutting” model with a linear dependence on the local environment in the initial state. This model distinguishes between Cu-Cu, Co-Cu, and Co-Co bonds which scale according to the strength of the interaction obtained from binding energies of Cu-Cu, Cu-Co, and Co-Co dimers: $E_{\text{Cu-Cu}} = -0.1$ eV, $E_{\text{Cu-Co}} = -0.15$ eV, and $E_{\text{Co-Co}} = -0.2$ eV. Pinning at substitutional Co atoms is described in the following way: for Cu atoms that are nearest neighbors to a substitutional Co the barrier for exchange or hopping is enhanced by $E_{\text{Cu-Co}} = -0.15$ eV. DFT-calculations show that Co adatoms are bound much stronger at substitutional Co, the adsorption energy is enhanced by 0.49 eV compared to the one on the clean Cu(001) surface. This implies that the barrier to diffuse away from a substitutional Co is substantially enhanced making the Co adatom practically immobile at such an adsorption site. Therefore, hopping diffusion away from a nucleation center is not considered in the simulation. However, Co adatoms are able to exchange in the vicinity of an incorporated Co atom. Preliminary results show that the exchange barrier in this case is comparable to the one on the clean Cu(001) surface. For hopping of Co adatoms the DFT-GGA barrier from a spin-polarized calculation is used which is 0.61 eV, *i.e.* 0.31 eV lower compared to the one from a nonmagnetic calculation 0.92 eV.

7.3.1 Island morphologies in the homo- and heteroepitaxial case

Snapshots of the first layer islands from KMC-simulations for the homo- (0.2 ML Cu on Cu(001)) and heteroepitaxial case (0.2 ML Co on Cu(001)) are plotted in Figs. 7.8 and 7.9, respectively. Different temperature ranges were selected due to the fact that diffusion barriers for Cu are much lower than for Co. Similar to the simulations on a square lattice for Cu on Cu(001) large rectangular islands are formed at room temperature with preferential orientation of the edges along the $[110]$ - and $[\bar{1}10]$ -direction.

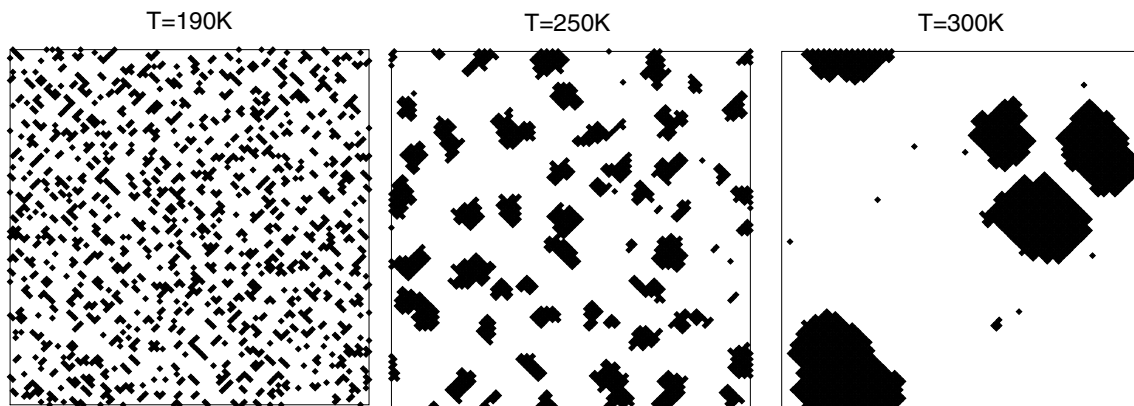


Figure 7.8: Snapshots of homoepitaxial growth of 0.2 ML Cu on Cu(001) at different temperatures and a deposition flux of 0.1ML/s. The diffusion barrier for hopping and exchange depends on the coordination in the initial state, $E_d = E_d^0 - NE_{\text{Cu-Cu}}$, with $E_{\text{Cu-Cu}} = -0.1$ eV.

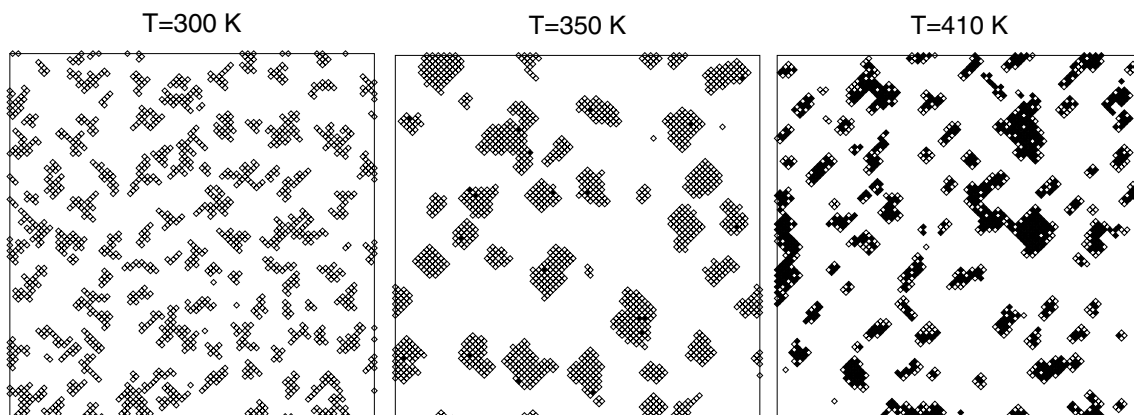


Figure 7.9: Snapshots of heteroepitaxial growth of 0.2 ML Co on Cu(001) at different temperatures and a deposition flux of 0.1ML/s. Co and Cu adatoms in the first layer are presented by empty and filled squares, respectively. The diffusion barrier for hopping and exchange of Co and Cu adatoms depends on the coordination in the initial state, $E_d^i = E_d^{0,i} - N_{\text{Cu}}E_{i-\text{Cu}} - N_{\text{Co}}E_{i-\text{Co}}$, where $i = \{\text{Cu}, \text{Co}\}$ with $E_{\text{Cu-Cu}} = -0.1$ eV, $E_{\text{Cu-Co}} = -0.15$ eV, and $E_{\text{Co-Co}} = -0.2$ eV.

For Co on Cu(001) at room temperature a high density of small islands which consist of several Co atoms is observed. At 350 K the rate of hopping diffusion is substantial and larger compact islands are formed. These islands show a preferential orientation along the $[110]$ - and $[1\bar{1}0]$ -direction. On the other hand, the rate for exchange diffusion is still comparatively low at this temperature: only several Co atoms have exchanged. The Cu adatoms expelled from the substrate layer

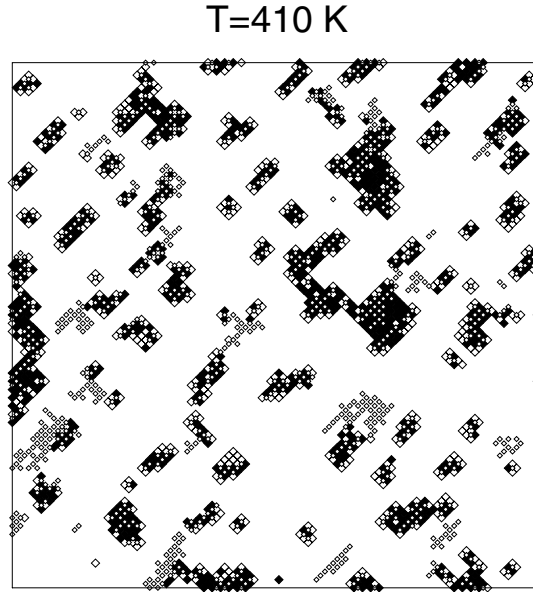


Figure 7.10: Growth of 0.2 ML Co on Cu(001) at 410 K and a deposition flux of 0.1ML/s. Co and Cu adatoms in the first layer are presented by empty and filled squares, respectively. Additionally the Co atoms in the substrate layer are shown as small empty squares. The diffusion barrier for hopping and exchange of Co and Cu adatoms depends on the coordination in the initial state, $E_d^i = E_d^{0,i} - N_{Cu}E_{i-Cu} - N_{Co}E_{i-Co}$, where $i = \{Cu, Co\}$ with $E_{Cu-Cu} = -0.1$ eV, $E_{Cu-Co} = -0.15$ eV, and $E_{Co-Co} = -0.2$ eV. The side length of the image corresponds to 460 Å.

(marked as black squares) are incorporated in the compact islands. The island morphology obtained at 350 K bears strong resemblance to the STM image taken at room temperature for a slightly lower coverage of 0.12 ML shown in Fig. 4.1. This implies that the islands in the STM images in Figs. 4.1 and 4.11a) consist mainly of Co and the contrast (dark indentations) in the first layer islands might be due to incorporated single Cu atoms.

However, at 410 K the picture changes dramatically. Here exchange processes play already an important role, almost 70% of the Co atoms have exchanged. Thus there is a substantial amount of substrate material in the first layer. The rate for hopping diffusion of these Cu adatoms is very high and consequently they diffuse quickly on the surface and form larger islands that are decorated at the edges by Co. Also there is a number of small islands where the percentage of Co is higher than in the larger islands. Thus the effect of bimodality, *i.e.* the formation of two different kinds of islands with respect to chemical composition and size observed in experiment (see Figs. 4.11b) and 4.14), is reproduced in the KMC simulation. On the other hand island shapes especially of the larger islands

are not described satisfactorily in the bond-cutting model. In order to achieve improvement additional barriers from DFT-calculations should be implemented instead.

The simulation result gives also the possibility to analyze the chemical composition of the substrate layer even in the regions covered by islands which is not accessible to experimental techniques. In Fig. 7.10 we have plotted additional to the islands in the first layer obtained at 410 K the substitutionally incorporated Co atoms as small empty squares. Practically all the islands are “pinned” at substitutional Co. Co inclusions under large islands are relatively compact and are capped mainly by Cu which builds the centers of these islands. Small mainly Co islands (*e.g.* tetramers) are “pinned” at single substitutional Co atoms. There are also several compact inclusions outside the islands.

7.3.2 Island Densities in the homo- and heteroepitaxial case

Figure 7.11 contains the island densities as a function of temperature for the homoepitaxial case (0.2 ML Cu on Cu(001)) and the heteroepitaxial case (0.2 ML Co on Cu(001)). For the homoepitaxial growth of Cu on Cu(001) we observe the temperature dependence known from standard nucleation theory, *i.e.* the island density decreases monotonically with growing temperature. An unexpected and complex behavior is observed however in the heteroepitaxial case. Initially, between 300 and 350 K, *i.e.* the region where Co diffusion via hopping prevails,

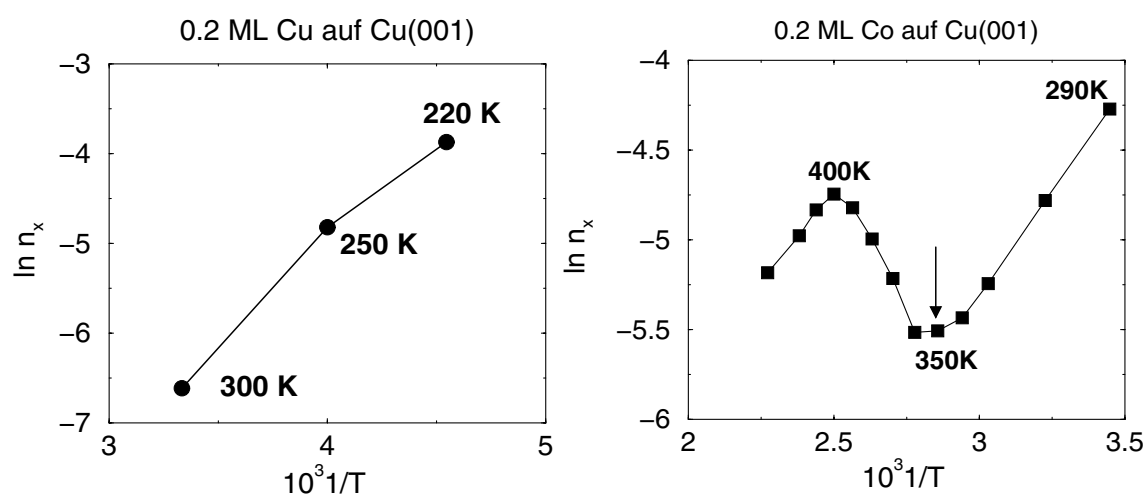


Figure 7.11: Scaling behavior of island density as a function of temperature for the homoepitaxial case 0.2 ML Cu on Cu(001) (left viewgraph) and the heteroepitaxial case 0.2 ML Co on Cu(001) (right viewgraph).

the island density decreases. However, at 350 K it exhibits a minimum and this minimum can be directly related to the activation temperature of the exchange process, which was estimated to be around 350 K (cf. Section 6.5). After the exchange process sets in, the island density starts to increase due to pinning at substitutional Co. A second crossover takes place at approximately 400 K where the exchange rate of Co is substantial and the diffusion of Cu adatoms generated on the surface starts to dominate. This results in a saturation and an eventual decrease of n_x . Actually, the island density obtained from STM images indicated already some of these features, *e.g.* an increase of n_x with temperature: $n_x = 1.64 \cdot 10^{-3}$ and $n_x = 2.23 \cdot 10^{-3}$ islands/surface unit cell at 295 K and 415 K, respectively (see Section 4.6 and [17]). However, in order to detect the theoretically predicted behavior, a systematic study of island density as a function of temperature would be necessary.

The influence of exchange processes on the scaling properties of the island density have been addressed in several studies in the literature [39, 40, 113, 157, 158]. Chambliss *et al.* [39] proposed for the heteroepitaxial growth of Fe on Cu(001), which shows a very similar behavior to Co on Cu(001), that already *monomers* embedded in the substrate layer constitute stable nuclei. Using a mean-field rate equations approach and assuming $i = 0$ Chambliss *et al.* [39] argue that island density depends only on coverage but does not depend on (F/D) . Later Amar and Family [157, 158] simulated the growth of Fe on Cu(001) by assuming that besides hopping adatoms can spontaneously freeze and additional adatoms that reach an embedded island are immediately incorporated in it. With this model they obtained a very weak dependence of the island density on (F/D) . The fact that the island density as a function of temperature possesses a minimum was first observed by Meyer and Behm [40] which used a simple model where between two deposition events adatoms perform h_0 hops, h_0 being the hopping rate and could also exchange. However, we point out that in these studies no explicit information on the activation barrier height for the different processes was used. Also, none of these models considered the effect of the substrate adatoms generated by the exchange processes on the surface morphology which is, as shown in our simulations, decisive to obtain the characteristics of *bimodal* growth.

7.4 Summary

KMC-simulations of the initial growth of Co and Cu on Cu(001) are presented in this Chapter. The N -fold algorithm [150–152] was employed and a fcc lattice is

implemented to describe heteroepitaxial growth. The microscopic processes are described by rates using the diffusion barriers obtained from DFT-GGA calculations. The main findings are:

In the homoepitaxial case growth of Cu on Cu(001) proceeds mainly via hopping and for the temperature range up to room temperature exchange does not play a significant role. At room temperatures rectangular islands form with edges along the $[110]$ - and $[1\bar{1}0]$ -direction. The simulations for Cu on Cu(001) yield the scaling behavior of island density expected from nucleation theory: $i = 1$. A good agreement to previous results [154–156] is obtained.

Results for the homo- and heteroepitaxial growth obtained from a bond cutting model are compared. For Cu on Cu(001) this model shows a good qualitative agreement to the simulation discussed above.

KMC simulations for the initial growth of Co on Cu(001) were used to check the predictions from density-functional theory and clarify experimental observations [17]. Two growth regimes are identified: in the low temperature regime ($T \leq 350$ K) hopping of Co adatoms leads to small compact islands with a rectangular form and edges along the $[110]$ - and $[1\bar{1}0]$ -direction. This implies that the islands in the STM images in Figs. 4.1 and 4.11a) at $T = 295$ K consist mainly of Co and the dark indentations in the first layer islands might be due to incorporated single Cu atoms.

The activation of exchange processes causes a drastic change of the surface morphology: Co atoms are incorporated in the substrate layer and act as pinning centers especially for Co adatoms on the surface. The Cu adatoms created by the exchange processes diffuse at a high rate and build large islands which are decorated predominantly at the edges by Co. Besides the large islands there is a number of small islands that contain mainly Co. These observations are in agreement with the STM results at 415 K shown in Fig. 4.11b) and 4.14.

In contrast to the homoepitaxial case where island density is monotonically decreasing with growing temperature in the heteroepitaxial case of Co on Cu(001) island density exhibits a minimum at the temperature where exchange is activated and increases again at higher temperatures. This behavior turns out to be common for heteroepitaxial systems where exchange processes are relevant [40] and is also expected *e.g.* for Fe/Cu(001) and Ni/Cu(001).

Although there is a good qualitative agreement between the island morphology obtained from the simulation and from STM, island shapes are not yet satisfactorily reproduced. Here it will be important to go beyond the “bond-cutting” scheme and implement a realistic description of the dependence of the barrier on the local environment based on DFT calculations.

Chapter 8

Summary and Outlook

The scope of this work comprises DFT-calculations with the FP-LAPW method on the stability of different Co/Cu-heterostructures in thermodynamic equilibrium and establishes a relation between the energetic trends and the structural, magnetic and electronic properties.

The second part of this work renders an important contribution towards a qualitative and quantitative understanding of the early stages of heteroepitaxial growth of metals in the presence of intermixing. The results are based on *ab initio* kinetic Monte Carlo simulations, *i.e.* KMC with rates of the atomistic processes calculated by density-functional theory.

The energetic stability, electronic, structural and magnetic properties of different configurations of Co on Cu(001) for a total coverage between 0 and 2 ML was studied in the first part of the thesis. The systems include a single Co adlayer, a Co bilayer film, a $c(2 \times 2)$ two-monolayers thick ordered surface alloy, as well as sandwich structures with a substrate capping layer. We find an unusually strong relaxation between the Co layers in a bilayer Co film on Cu(001) which is attributed to the strong *d-d* hybridization and is confirmed by the broadening of the *d* band of Co in the bilayer film as compared to the single adlayer. Due to the *d-d* hybridization a bilayer Co-island is more stable than a Co monolayer which explains experimental observations. Under thermodynamic equilibrium conditions DFT-calculations predict the formation of bilayer Co islands covered by a capping layer of copper. This structure reflects the tendency of Co to maximize its coordination and in particular the number of Co-Co bonds. Magnetism counteracts this trend, however the relative stability between different structures is the same for the nonmagnetic and ferromagnetic case.

For submonolayer coverages we find that the *substitutional* adsorption is strongly favored compared to on-surface adsorption in a fourfold hollow site. Moreover, the tendency towards intermixing is coverage dependent and especially

for $\theta \leq 0.2$ ML it represents an alternative to the formation of compact Co islands. Ferromagnetic Co adatoms adsorbed in a fourfold hollow or substitutional site induce a small spin-polarization in the substrate with an oscillatory character: nearest Cu neighbors couple ferromagnetically while next nearest neighbors couple antiferromagnetically. This polarization indicates that the magnetic coupling of the adatoms is mediated by the substrate.

Due to the substitutional adsorption we have an unusual situation on the surface: besides the substitutionally incorporated Co atoms there are Co as well as Cu adatoms on the surface. DFT-calculations show that Co atoms embedded in the substrate layer act as *nucleation centers* both for Cu and Co adatoms on the surface, the effect being almost two times stronger for Co than for Cu.

Further the adatom diffusion of both species (Co and Cu) on flat regions and along steps on the Cu(001) surface was investigated. For Cu the barrier for diffusion via hopping between adsorption sites is 0.49 eV in good agreement with previous DFT-results [111] and experimental values. The barrier for exchange is two times higher. Spin-polarized Co adatoms have a lower mobility on the surface: the barrier for hopping is 0.61 eV, while the barrier for exchange is 1.0 eV. Spin-polarization reduces significantly the barrier for processes where the variation of coordination number between the initial and transition state is substantial, *e.g.* for hopping from 0.92 eV (nonmagnetic case) to 0.61 eV (spin-polarized case). Diffusion barriers along [110]-steps on the Cu(001) surface are lower than the barriers for terrace diffusion by hopping, 0.40 eV and 0.55 eV for Cu and Co, respectively. The result can be explained by the smaller variation of the coordination between initial and transition state (five and four) as opposed to terrace diffusion (four and two).

An *ab initio* kinetic Monte Carlo code for the heteroepitaxial growth was implemented: the simulations are performed on a fcc lattice thus enabling a proper description of the exchange process (incorporation of Co in the substrate layer and generation of an on-surface Cu adatom) and pinning at substitutional Co. The DFT-GGA barriers were used to calculate the rates for the microscopic processes. Interactions with other adatoms on the surface are described in a bond-cutting model which takes into account the different strength of the bonds between different chemical species. The surface morphology and scaling behavior of the island density as a function of temperature was studied for the homoepitaxial case (0.2 ML Cu on Cu(001)) and heteroepitaxial case (0.2 ML Co on Cu(001)).

In the homoepitaxial case mass transport proceeds mainly by hopping, exchange does not play a significant role. At room temperature rectangular islands form with edges along the [110]- and $[1\bar{1}0]$ -direction.

For the initial growth of Co on Cu(001) two different growth regimes are iden-

tified:

- for $T \leq 350$ K growth proceeds mainly by hopping. Compact islands are formed with edges along the $[110]$ - and $[\bar{1}\bar{1}0]$ -direction. In this regime heteroepitaxial growth resembles the homoepitaxial case, however adatom mobility is lower. Occasional exchange processes take place and the Cu atoms ejected from the substrate layer are incorporated in the first layer islands.
- The activation of the exchange process leads to a dramatic change in surface morphology: At $T = 415$ K a substantial amount of the Co atoms are incorporated in the substrate layer. The interplay of high diffusion rate of Cu adatoms generated on the surface by the exchange processes and the pinning at substitutional Co gives rise to a *bimodal* growth mode. It is characterized by a large number of small Co islands and large islands containing mainly Cu and decorated by Co at the edges.

In the heteroepitaxial case we find severe deviations from the predictions of standard nucleation theory: A monotonic decrease of island density with growing temperature is typical for the homoepitaxial case. Instead, for Co on Cu(001), island density exhibits a minimum around 350 K and increases again at higher temperatures. This minimum can be directly correlated to the activation of atomic exchange.

The results from the KMC simulations based on information from DFT-calculations corroborate experimental findings [13, 17] and provide understanding for the driving mechanisms in the initial growth of this system. Moreover, we believe that the mechanisms identified for Co on Cu(001) should be common to a broader class of materials, *e.g.* other $3d$ metals grown on a noble metal substrate. As experiments show, a similar behavior is expected for Fe/Cu(001) [39], Fe/Au(001) [131] and Ni/Cu(001) [41].

We note that by far not *all* relevant microscopic processes could be investigated in the scope of this work due to the high computational cost. However a fundamental understanding for the structures evolving under thermal equilibrium conditions as well as the basic adsorption and diffusion mechanisms controlled by kinetics could be achieved.

An important issue for our future work would be to improve, based on DFT-calculations, the description of the adatom-adatom interactions in the KMC simulation beyond the “bond-cutting” model. Additional barriers, *e.g.* for diffusion of a Co atom across a step edge of a Co- or Cu-island can possibly explain the microscopic origin of bilayer growth. Also it would be desirable to extend the KMC code to describe multilayer growth. Another interesting prospect is to combine

the *ab initio* KMC-results for the surface morphology with a model describing the magnetic coupling between islands on the basis of KMC-simulations [160] in view of studying multi-domain ordering as a function of growth conditions.

Bibliography

- [1] A. Clarke, G. Jennigs, R. F. Willis, P. J. Rous, and J. B. Pendry, *Surf. Sci.* **187**, 327 (1987).
- [2] P. Grünberg, R. Schreiber, Y. Pang, M. B. Brodsky, and H. Sowers, *Phys. Rev. Lett.* **57**, 2442 (1986).
- [3] S. S. P. Parkin, N. More, and K. P. Roche, *Phys. Rev. Lett.* **64**, 2304 (1990).
- [4] S. S. P. Parkin, *Phys. Rev. Lett.* **67**, 3598 (1991).
- [5] M. Baibich *et al.*, *Phys. Rev. Lett.* **61**, 2472 (1988).
- [6] G. Binasch, P. Grünberg, F. Saurenbach, and W. Zinn, *Phys. Rev. B* **39**, 4828 (1989).
- [7] J. Belleson and E. Grochowski, *The era of giant magnetoresistive heads*, <http://ssdweb01.storage.ibm.com/hardsoft/diskdrdl/technolo/gmr/gmr.htm>.
- [8] M. Dax, *Semicond. Int.* **20**, 84 (1997).
- [9] *Motorola demonstrates revolutionary memory technology; MRAM targeted for future*, <http://www.motorola.com/>
- [10] G. A. Prinz, *Science* **282**, 1660 (1998).
- [11] F. J. Himpsel, J. E. Ortega, G. J. Mankey, and R. F. Willis, *Adv. Phys.* **47**, 511 (1998).
- [12] H. Li and B. P. Tonner, *Surf. Sci.* **237**, 141 (1990).
- [13] J. Fassbender, R. Allenspach, and U. Dürig, *Surf. Sci.* **383**, L 742 (1997).
- [14] P. Hegeman, *Morphology of thin Co-films on the (001) surfaces of Cu, Si and Ge*, PhD thesis, Universiteit Twente, 1998.
- [15] A. K. Schmid, A. Atlan, H. Itoh, B. Heinrich, T. Ichinokawa, and J. Kirschner, *Phys. Rev. B* **48**, 2855 (1993).

- [16] F. Nouvertné, U. May, A. Rampe, M. Gruyters, U. Korte, R. Berndt, and G. Güntherodt, *Surf. Sci.* **436**, L653 (1999).
- [17] F. Nouvertné, U. May, M. Bamming, A. Rampe, U. Korte, G. Güntherodt, R. Pentcheva and M. Scheffler, *Phys. Rev. B*, **60**, 14382 (1999).
- [18] E. Bauer, *Z. Kristallogr.* **110**, 372 (1958).
- [19] J. Vrijmoeth, H. A. van der Vegt, J. A. Meyer, E. Vlieg, and R. J. Behm, *Phys. Rev. Lett.* **72**, 3843 (1994).
- [20] K. Bromann, H. Brune, H. Röder, and K. Kern, *Phys. Rev. Lett.* **75**, 677 (1995).
- [21] S. Glasstone, K. J. Laidler, H. Eyring, *The Theory of Rate Processes*, McGraw-Hill, New York, 1941.
- [22] T. T. Tsong, *Atom-probe field ion microscopy*, Cambridge Univ. Press, Cambridge, (1990).
- [23] G. L. Kellogg, *Phys. Rev. Lett.* **64**, 3143 (1990).
- [24] T. T. Tsong and C. Chen, in *The Chemical Physics of Solid Surfaces*, Eds. D. A. King, D. P. Woodruff, Vol. 8, Elsevier Science, Amsterdam, (1997).
- [25] G. Ehrlich, *Surf. Sci.* **246**, 1 (1990); *ibid* **299/300**, 628 (1994); *ibid* **331/335**, 865 (1994).
- [26] H. Brune, *Surf. Sci. Reports* **31**, 121 (1998).
- [27] L. Hansen, P. Stoltze, K. W. Jacobsen, and J. K. Nørskov, *Phys. Rev. B* **44**, 6523 (1991).
- [28] C.-L. Liu, *Surf. Sci.* **316**, 294 (1994).
- [29] P. J. Feibelman, *Phys. Rev. Lett.* **65**, 729 (1990).
- [30] R. Stumpf and M. Scheffler, *Phys. Rev. B* **53**, 4958 (1996).
- [31] B. D. Yu and M. Scheffler, *Phys. Rev. B* **55**, 13916 (1997).
- [32] B. D. Yu and M. Scheffler, *Phys. Rev. B* **56**, R15569 (1997).
- [33] J. A. Venables in *The Chemical Physics of Solid Surfaces*, Vol.8, D. A. King and D. P. Woodruff, eds. (Elsevier Science, Amsterdam, 1997); J.A. Venables, G.D. Spiller, and M. Hanbucken, *Rep. Prog. Phys.* **47**, 399 (1984).

- [34] P. Ruggerone, C. Ratsch, and M. Scheffler, in *The Chemical Physics of Solid Surfaces*, Eds. D. A. King, D. P. Woodruff, Vol. 8, Elsevier Science, Amsterdam, (1997).
- [35] C. Ratsch, P. Ruggerone, and M. Scheffler, in *Morphological Organization in Epitaxial Growth and Removal*, Eds. Z. Zhang, M. G. Lagally. World Scientific, Vol. 14, Singapore, 3-29 (1998).
- [36] S. Ovesson, A. Bogicevic, and B. I. Lundqvist, *Phys. Rev. Lett.* **79**, 2506 (1997).
- [37] K. A. Fichthorn and M. Scheffler, *Phys. Rev. Lett.* **84**, 5371(2000).
- [38] P. Kratzer and M. Scheffler, in preparation.
- [39] D. D. Chambliss and K. E. Johnson, *Phys. Rev. B* **50**, 5012 (1994).
- [40] J. A. Meyer and R. J. Behm, *Surf. Sci.* **322**, L275 (1995).
- [41] J. Lindner, P. Pouloupoulos, F. Wilhelm, M. Farle and K. Baberscke, *Phys. Rev. B.* **62**, 10431 (2000).
- [42] D. J. Singh, *Planewaves, Pseudopotentials and the LAPW method* (Kluwer Academic Publishers, Boston, 1994).
- [43] P. Hohenberg und W. Kohn, *Phys. Rev.* **136**, B884 (1964).
- [44] W. Kohn und L. J. Sham, *Phys. Rev.* **140**, A1133 (1965).
- [45] R. G. Parr and W. Yang, *Density-Functional Theory of Atoms and Molecules*, Oxford University Press, Oxford,(1989).
- [46] R. O. Jones and O. Gunnarsson, *Rev. Mod. Phys.* **61**,689 (1989).
- [47] L. Hedin and B. I. Lundqvist, *J. Phys. C.* **4**, 2064 (1971).
- [48] U. von Barth and L. Hedin, *J. Phys. C.* **5**, 1629 (1972).
- [49] V. L. Moruzzi, J. F. Janak and A. R. Williams, *Calculated Electronic Properties of Metals* (Pergamon, New York, 1978).
- [50] D. M. Ceperley and B. J. Alder, *Phys. Rev. Lett.* **45**,566 (1980).
- [51] S. H. Vosko, L. Wilk and N. Nusair, *Can. J. Phys.* **58**, 1200 (1980).
- [52] J. P. Perdew and A. Zunger, *Phys. Rev. B* **23**, 5048 (1981).
- [53] J. P. Perdew and Y. Wang, *Phys. Rev. B* **45**, 13244 (1992).

- [54] J. P. Perdew, S. Burke, and M. Ernzerhof, Phys. Rev. Lett. **77**, 3865, (1996).
- [55] O. K. Andersen, Phys. Rev. B **12**, 3060 (1975).
- [56] H. L. Skriver, *The LMTO-Method*, Springer-Verlag, New York, (1983).
- [57] J. Koringa, Physica **13**, 392 (1947); W. Kohn and N. Rostoker, Phys. Rev. **94**, A 1111 (1954).
- [58] S. Y. Savrasov, Phys. Rev. B **54**, 16470 (1996).
- [59] M. Methfessel, M. van Schilfgaarge, and R. A. Casali, *A Full-Potential LMTO method based on smooth Hankel functions*, <http://ihp02.ihp-ffo.de/msm/>.
- [60] J. C. Slater, Phys. Rev. **51**, 846 (1937).
- [61] J. C. Slater, Phys. Rev. **81**, 385 (1951).
- [62] T. L. Loucks, *Augmented Plane Wave Method* (Benjamin, New York, 1967).
- [63] H. Bross, Phys. Kondens. Mater. **3**, 119 (1964); Z. Phys. B **3**, 233 (1990).
- [64] P. Marcus, Int. J. Quantum. Chem. Suppl. **1**, 567 (1967).
- [65] D. R. Hamann, Phys. Rev. Lett. **42**, 662 (1979).
- [66] E. Wimmer, H. Krakauer, M. Weinert and A. J. Freeman, Phys. Rev. B **24**, 864 (1981).
- [67] M. Weinert, E. Wimmer and A. J. Freeman, Phys. Rev. B **26**, 4571 (1982).
- [68] H. Krakauer, M. Posternak, A. J. Freeman, Phys. Rev. B **19**, 1706 (1979).
- [69] H. Krakauer, M. Posternak, A. J. Freeman and D. D. Koelling, Phys. Rev. B **21**, 1706 (1980).
- [70] M. Weinert, J. Math. Phys. **22**, 2433 (1981).
- [71] P. Blaha, K. Schwarz and J. Luitz, WIEN97, A Full Potential Linearized Augmented Plane Wave Package for Calculating Crystal Properties, (Karlheinz Schwarz, Techn. Univ. Wien, Vienna 1999). ISBN 3-9501031-0-4 Updated version of P. Blaha, K. Schwarz, P. Sorantin, and S. B. Trickey, Comp.Phys.Commun.59, 399, 1990.
- [72] M. Weinert and J. W. Davenport, Phys. Rev. B **45**, 13709 (1992).
- [73] J. Neugebauer and M. Scheffler, Phys. Rev. B **46**, 16067 (1992).

- [74] M. M. Valiev and G. W. Fernando, Phys. Rev B **52**, 10697 (1995).
- [75] F. Wagner, T. Laloyaux, and M. Scheffler, Phys. Rev. B **57**, 2102 (1998).
- [76] M. Petersen, F. Wagner, L. Hufnagel, M. Scheffler, P. Blaha and K. Schwarz, Comp. Phys. Commun. **126**, 294 (2000).
- [77] C. G. Broyden, Math. comput. **21**, 368 (1966).
- [78] B. Kohler, S. Wilke, M. Scheffler, R. Kouba and C. Ambrosch-Draxl, Comp. Phys. Commun. **94**, 31 (1996).
- [79] R. Dohmen, J. Pichlmeier, M. Petersen, F. Wagner, and M. Scheffler, submitted to Computing in Science & Engineering (2000).
- [80] P. Bruno, Phys. Rev. B **52**, 411 (1995).
- [81] P. Bruno and C. Chappert, Phys. Rev. Lett. **67**, 1602 (1991).
- [82] P. Alippi, P. M. Marcus, and M. Scheffler, Phys. Rev. Lett. **78**, 3892 (1997).
- [83] R. Pentcheva and S. Blügel, Jülich Reports **3364** (1997).
- [84] J. R. Cerda, P. L. de Andres, A. Cebollada, R. Miranda, E. Navas, P. Schuster, C. M. Schneider, and J. Kirschner, J. Phys.: Cond. Matt **5**, 2055 (1993).
- [85] J. Shen, J. Giergel, A. K. Schmid, and J. Kirschner, Surf. Sci. **328**, 32 (1995).
- [86] U. Bovensiepen, P. Pouloupoulos, W. Platow, M. Farle, and K. Baberschke, J. Magn. Magn. Mat. **192**, L386 (1999).
- [87] R. Wu and A. J. Freeman, J. Appl. Phys. **79**, 6500 (1996).
- [88] S. Blügel, *Habilitationsschrift*, RWTH Aachen, (1995).
- [89] O. Erikson, A. M. Boring, R. C. Albers, G. W. Fernando, and B. R. Cooper, Phys. Rev. B **45**, 2868 (1992).
- [90] M. Ø. Pedersen, I. A. Bönicke, E. Lægsgaard, I. Stensgaard, A. Ruban, J. K. Nørskov, and F. Besenbacher, Surf. Sci. **387**, 86, (1997).
- [91] The area of a (1×1) -structure is 6.30 \AA^2 .
- [92] H. J. Monkhorst and J. D. Pack, Phys. Rev. B **18**, 45897 (1978).
- [93] Q. T. Jiang, P. Fenter, and T. Gustafsson, Phys. Rev. B **44**, 5773 (1991).
- [94] H. L. Davis and J. R. Noonan, Surf. Sci. **126**, 245 (1983).

- [95] P. O. Gartland, S. Berge, and B. J. Slagsvold, Phys. Rev. Lett. **28**, 738 (1973).
- [96] G. A. Haas and R. E. Thomas, J. Appl. Phys. **48**, 86 (1977).
- [97] G. G. Tibbets, J. M. Burkstrand, and J. C. Tracy, Phys. Rev. B **15**, 3652 (1977).
- [98] A. Saúl and M. Weissmann, Phys. Rev. B **60**, 4982 (1999).
- [99] The calculations for bilayer $c(2 \times 2)$ -alloy were performed with the same cutoff parameters as for the (1×1) -structures (see Section 3.2 and 15 k_{\parallel} -points in the irreducible wedge of the Brillouin-zone).
- [100] B. Poelsema, private communication.
- [101] For fct cobalt with $a_{\parallel} = a_{\text{Cu}}$ we obtained the following distances in z -direction: $a_z^{\text{NM}} = 3.23 \text{ \AA}$ and $a_z^{\text{FM}} = 3.31 \text{ \AA}$.
- [102] We note here that the formation energy of Co(001) was also calculated with respect to fct cobalt bulk in order to separate the elastic from the electronic effects.
- [103] M. Methfessel, D. Henning, and M. Scheffler, Appl. Phys. A **55**, 442 (1992).
- [104] The fact that the equilibrium lattice constant of a free-standing Co monolayer is noticeably smaller than the lattice constant of Co (or Cu) bulk reflects that the low coordination of atoms in the free-standing monolayer leads to a stronger bonding between the cobalt atoms and thus shorter bond lengths. This result follows Pauling's description of the relation between coordination, bond strength, and bond length.
- [105] M. Farle *et al.*, priv. communication.
- [106] P. Srivastava, F. Wilhelm, A. Ney, M. Farle, H. Wende, N. Haack, G. Ceballos, and K. Baberschke, Phys. Rev. B **58**, 5701 (1998).
- [107] W. Clemens, T. Kachel, O. Rader, E. Vescovo, S. Blügel, C. Carbone, and W. Eberhardt, Solid State Commun. **81**, 739 (1992).
- [108] M. Methfessel, D. Henning, and M. Scheffler, Appl. Phys. A **55**, 442 (1992).
- [109] D. Spanjaard and Desjonquères in *Interaction of Atoms and Molecules with Solid Surfaces*, ed. by V. Bortolani (Plenum, New York, 1990).
- [110] A. K. Schmid, and J. Kirschner, Ultramicroscopy **4-44**, 483 (1992).

- [111] G. Boisvert and L. J. Lewis, Phys. Rev. B **56**, 7643 (1997).
- [112] R. Pentcheva and M. Scheffler, submitted to Phys. Rev. B.
- [113] A. Zangwill and E. Kaxiras, Surf. Sci. **326**, L483 (1995).
- [114] M. Hansen, *Constitution of binary alloys* (McGraw-Hill, New York 1958).
- [115] A. Schmalz *et al.*, Phys. Rev. Lett. **67**, 2163 (1991); C. Stampfl and M. Scheffler, Surf. Rev. Lett. **2**, 317 (1995).
- [116] M. Wuttig, Y. Gauthier, and S. Blügel, Phys. Rev. Lett. **70**, 3619 (1993) .
- [117] A. Davies, J. Strosio, D.T. Pierce, and R.J. Celotta, Phys. Rev. Lett. **76**, 4175 (1996).
- [118] B. Nonas, K. Wildberger, R. Zeller, and P. H. Dederichs, Phys. Rev. Lett. **80**, 4574 (1998).
- [119] S. Blügel, Appl. Phys. A **63**, 595, (1996).
- [120] P. H. T. Philipsen and E. J. Baerends, Phys. Rev. B **54**, 5326 (1996).
- [121] The adsorption of a Cu adatom at a kink site does not alter the structure on the surface, i.e. the kink is only moved by one atom further. Thus, adsorption of a Cu adatom at a kink site equals adding an additional bulk Cu atom to the system.
- [122] N. A. Levanov, V. S. Stepanyuk, W. Hergert, D. I. Bazhanov, P. H. Dederichs, A. Katsnelson, and C. Massobrio, Phys. Rev. B **61**, 2230 (2000).
- [123] J. Hölzl and F. K. Schulte, in *Springer tracts in Modern Physics* **85**, Springer, Berlin (1979).
- [124] M. Scheffler and C. Stampfl, Theory of Adsorption on Metal Substrates. in *Handbook of surface Science, Vol. 2: Electronic Structure*, Eds. K. Horn and M. Scheffler (Elsevier, Amsterdam, 1999). Phys. Rev. B **46**, 4816 (1992).
- [125] J. Fassbender, U. May, B. Schimmer, R. M. Jungblut, B. Hillerbrands, and G. Güntherodt, Phys. Rev. Lett. **75**, 4476 (1995).
- [126] P. Lang, V. S. Stepanyuk, K. Wildberger, R. Zeller, and P. H. Dederichs, Sol. St. Commun **92**, 755 (1994).
- [127] The assumption that diffusion barriers roughly scale with the energy of the initial state is plausible and has some justification. However, we point out, that a systematic investigation is necessary to prove this aspect.

- [128] $E_{\text{Cu}}^0 = -3275.548$ Ry, $E_{\text{Co}}^0 = -2760.381$ Ry. From a least squares fit to various DFT-LDA results we obtained: $A_{\text{Cu}} = -0.105$ Ry, $A_{\text{Co}} = -0.090$ Ry, $B_{\text{Cu}} = 0.003$ Ry, $B_{\text{Co}} = -0.012$ Ry.
- [129] R. Pentcheva and M. Scheffler, Phys. Rev. B **61**, 2211 (2000).
- [130] B. Hammer, L. B. Hansen, and J. K. Nørskov, Phys. Rev. B **59**, 7413 (1999).
- [131] O. S. Hernán, A. L. Vásquez da Parga, J. M. Gallego, and R. Miranda, Surf. Sci. **415**, 106 (1998).
- [132] C. Ratsch and M. Scheffler, Phys. Rev. B **58**, 13163 (1998).
- [133] G. L. Kellogg and P. J. Feibelman, Phys. Rev. Lett. **64**, 3143 (1990).
- [134] C. Chen and T. T. Tsong, Phys. Rev. Lett. **64**, 3147 (1990).
- [135] Z.-J. Tian and T. S. Rahman, Phys. Rev. B **47**, 9751 (1993).
- [136] L. S. Perkins and A. E. DePristo, Surf. Sci. **294**, 67 (1993), *ibid.***325**, 169 (1995).
- [137] J. J. de Miguel, A. Sánchez, A. Cebollada, J. M. Gallego, J. Ferrón, and S. Ferrer, Surf. Sci. **189/190**, 1062 (1987).
- [138] H.-J. Ernst, F. Farbre, and J. Lapujoulade, Phys. Rev. B **46**, R1929 (1992).
- [139] M. Breeman and D. O. Boerma, Surf. Sci. **269/270**, 224 (1992).
- [140] H. Dürr, J. F. Wendelken, and J.-K. Zuo, Surf. Sci. **328**, L527 (1995).
- [141] J. B. Hannon, C. Klünker, M. Giesen, H. Ibach, N. C. Bartelt, and J. C. Hamilton, Phys. Rev. Lett. **79**, 2506 (1997).
- [142] K. W. Jacobsen, J. K. Nørskov, and M. J. Puska, Phys. Rev. B **35**, 7423 (1987).
- [143] F. Nouvertné, *Das epitaktische Wachstum von Co/Cu(001)*, PhD Thesis, RWTH Aachen, (1998).
- [144] I. J. Robertson, V. Heine, and M. C. Payne, Phys. Rev. Lett. **70**, 1944 (1993); *ibid.* **72**, 2302 (1994.)
- [145] C.-L. Liu, J. M. Cohen, J. B. Adams, and A. F. Voter, Surf. Sci. **253**, 334 (1991).
- [146] A. C. Levi and M. Kotrla, J. Phys.: Cond. Matt **9**, 299 (1997).

- [147] N. C. Metropolis, A. W. Rosenbluth, M. N. Rosenbluth, A. N. Teller, and E. Teller, *J. Chem. Phys.* **21**, 1087 (1953).
- [148] A. Voter, *Phys. Rev. B* **34**, 6819 (1986).
- [149] H. C. Khang and W. H. Weinberg, *J. Chem. Phys.* **90**, 2824 (1989).
- [150] K. A. Fichthorn and W. H. Weinberg, *J. Chem. Phys.* **95**, 1090 (1991).
- [151] A. B. Bortz, M. H. Kalos, and J. L. Lebowitz, *J. Comp.. Phys.* **17**, 10 (1975).
- [152] S. Clarke, M. Wilby, and D. Vvedensky, *Surf. Sci.* **255**,91 (1991).
- [153] M. Kotrla and A. C. Levi, *J. Stat. Phys.***64**, 579, (1991).
- [154] O. Biham, I. Furman, M. Karimi, G. Vidali, R. Kennett, and H. Zeng, *Surf. Sci.* **400**, 29 (1998).
- [155] M. Breeman, G. T. Barkema, M. H. Langelaar, and D. O. Boerma, *Thin Solid Films* **272**, 195 (1996).
- [156] M. Breeman, G. T. Barkema, and D. O. Boerma, *Surf. Sci.* **303**, 25 (1994).
- [157] J. G. Amar and F. Family, *Phys. Rev. Lett.* **74**, 2066 (1995).
- [158] J. G. Amar and F. Family, *Thin Solid Films* **272**, 208 (1996).
- [159] M. H. Langelaar, *Growth and atomic structure of iron-silver layers*, PhD Thesis, Rijksuniversiteit Groningen, Holland, (1998).
- [160] P. J. Jensen, R. Brinzanik, and K. H. Bennemann, private communication.

Danksagung

Mein erster Dank gilt Prof. Dr. Matthias Scheffler für die spannende Themenstellung, sein stetes Interesse und die Unterstützung meiner Arbeit. Die Anregungen zu verschiedenen Projekten und den Freiraum, den er mir gegeben hat, das Thema selbst zu gestalten, habe ich sehr geschätzt. Die zahlreichen Diskussionen mit ihm haben mein physikalisches Verständnis bereichert.

Prof. Dr. K.-H. Bennemann danke ich für die freundliche Übernahme des Erstgutachtens.

Prof. Dr. Kristen Fichthorn danke ich für die Erstversion des KMC-Programms, die sie mir zur Verfügung gestellt hat und das als Ausgangspunkt für die Implementierung der verschiedenen Wachstumsmodellen gedient hat. Ihr Interesse sowie ihre positive und unkomplizierte Art haben die Zusammenarbeit sehr angenehm gemacht.

Der wissenschaftliche Austausch mit anderen Gruppen an der FU im Rahmen vom SFB290 hat viel zum Erfolg dieser Arbeit beigetragen. An dieser Stelle möchte ich mich bei Prof. Dr. Klaus Baberschke und seiner Gruppe, insbesondere bei Prof. Dr. Michael Farle und Fabrice Wilhelm bedanken für viele freundschaftlichen Diskussionen nicht nur über Physik.

Prof. Dr. G. Güntherodt, Dr. Frank Nouvertné und Ulli May danke ich für die gute und stimulierende Zusammenarbeit zwischen Theorie und Experiment.

Meinen Kollegen gilt mein herzlicher Dank für die gute Atmosphäre und die spannende Zeit, die wir in und ausserhalb des Instituts verbracht haben. Hier möchte ich insbesondere Tosja und Sönke erwähnen, mit denen ich ein Zimmer geteilt habe. Trotz einiger kleineren Turbulenzen war dies eine schöne Zeit und sie wird mir in guter Erinnerung bleiben.

Dr. Peter Kratzer danke ich für zahlreiche Diskussionen u.a. über die Monte Carlo Methoden. Ihm und Dr. Tosja Zywietz danke ich für die Durchsicht des Manuskripts.

Gaby Tysper danke ich für ihre Hilfsbereitschaft in organisatorischen Fragen und auch für die Diskussionen über den Berliner und seine Besonderheiten.

Desweiteren möchte ich mich bei meinen Freunden bedanken, die mich auf direktem oder elektronischem Wege während meiner Doktorarbeit begleitet haben, insbesondere bei Dr. Karsten Wildberger, Dirk Weiss, Dr. Jörn Barth und bei

Stefanie Leuenberger, mit der ich nicht nur alle Sportarten von Jazz Dance bis Tai Chi ausprobiert habe.

Denen, die mir trotz räumlicher Entfernung sehr nahe standen, meiner Mutter, meiner Schwester und meinem Mann Michael, danke ich für die liebevolle Unterstützung und ihre Geduld. Meinen Eltern bin ich dankbar, daß sie das Interesse an die Wissenschaft in mir geweckt und unterstützt haben.

Lebenslauf

Persönliche Daten

Name: Rossitza Vladimirova Pentcheva
geboren am: 15.11.1970 in Sofia, Bulgarien
Staatsangehörigkeit: bulgarisch

Schulbildung

09/1977-06/1980 Grundschule Sofia
09/1980-07/1988 Polytechnische Mittel- und Oberschule(ESPU)
in Sofia; Abschluß: Abitur

Studium

09/1988-02/1991 Studium der Physik
an der Sofijski Universität
03/1991-02/1992 Studiums der deutschen Sprache
an der Universität zu Köln als DAAD-Stipendiatin
04/1992-05/1995 Hauptstudium der Physik an der Universität zu Köln
Schwerpunkt: Theoretische Festkörperphysik
07/1995-10/1996 Diplomarbeit am Institut für Festkörperphysik
des Forschungszentrums Jülich
bei Dr. S. Blügel und Prof. Dr. Eberhardt
Thema: "Ab-initio Rechnungen zum
Zusammenhang zwischen Magnetismus und Struktur
ultradünner magnetischer Filme"
10/1997 DAAD-Preis für ausländische Studierende
der Universität zu Köln
01/1997-07/2000 Promotion am Fritz-Haber-Institut
der Max-Planck-Gesellschaft in Berlin
bei Prof. Dr. M. Scheffler

Kurzfassung

Die vorliegende Arbeit umfasst Dichtefunktionaltheorie-Rechnungen (DFT) mit der *full-potential augmented plane waves* (FP-LAPW) Methode zur Stabilität verschiedener Co/Cu-Heterostrukturen im thermodynamischen Gleichgewicht. Sie stellt eine Verbindung her zwischen der Energetik und den strukturellen, magnetischen und elektronischen Eigenschaften.

Der zweite Teil der Arbeit leistet einen Beitrag zum qualitativen und quantitativen Verständnis der Anfangsphase des Wachstums in heteroepitaktischen metallischen Systemen, bei denen Austauschprozesse eine Rolle spielen. Hierzu wurden *ab initio* kinetische Monte Carlo (KMC) Simulationen durchgeführt, d.h. daß die Raten der mikroskopischen Prozesse mit DFT berechnet wurden.

Im ersten Teil der Arbeit wurden die Stabilität und die strukturellen, elektronischen und magnetischen Eigenschaften von verschiedenen Konfigurationen von Co auf Cu(001) für Bedeckungen zwischen 0 und 2 Monolagen (ML) untersucht. Die Systeme umfassen jeweils eine einzelne Co Monolage, eine Co-Doppellage, eine 2ML-dicke $c(2 \times 2)$ -geordnete Oberflächenlegierung sowie Sandwich-Strukturen, die mit einer Substratschicht bedeckt sind. Bei 2ML Co/Cu(001) finden wir eine starke Relaxation des Interlagenabstandes zwischen den beiden Co-Lagen. Dieser Effekt ist auf die starke d - d -Hybridisierung zurückzuführen, was durch die deutliche Verbreiterung des d -Bandes von Kobalt in dem Doppellagenfilm im Vergleich zu der einzelnen Co-Monolage bestätigt wird. Aufgrund der d - d -Hybridisierung ist eine Co-Doppellage energetisch stabiler als die einzelne Monolage, was das experimentell beobachtete Wachstum von zweilagigen Inseln erklärt. Im thermodynamischen Gleichgewicht sagen DFT-Rechnungen die Bildung einer $p(1 \times 1)$ -Sandwich-Struktur voraus, die aus einer Co-Doppellage und einer Cu-Deckschicht besteht. Diese Struktur spiegelt die Tendenz von Co wider, seine Koordination und insbesondere die Anzahl der Co-Co-Bindungen zu maximieren. Es zeigt sich, daß der Magnetismus keine qualitative Änderung dieser Trends herbeiführt.

Für Submonolagenbedeckungen zeigt sich, daß die substitutionelle Adsorption, verglichen mit der normalen Adsorption auf einem vierfach koordinierten Platz, stark energetisch bevorzugt wird. Darüber hinaus ist die Tendenz zum Durchmischen in der Oberflächenschicht bedeckungsabhängig. Insbesondere für $\theta \leq 0.2$ ML stellt die substitutionelle Adsorption eine Alternative zur Bildung von kompakten Co-Inseln dar. Spinpolarisierte Co-Adatome auf einem vierfach koordinierten oder substitutionellen Platz induzieren eine schwache Spinpolarisation im Substrat mit einem oszillatorischen Charakter: Nächste Cu-Nachbarn

koppeln ferromagnetisch, übernächste antiferromagnetisch. Diese Polarisation zeigt, daß die magnetische Kopplung zwischen den Co-Adatomen durch Substrat vermittelt wird.

Aufgrund der substitutionellen Adsorption entsteht eine ungewöhnliche Situation auf der Oberfläche: Neben den substitutionell eingebauten Co-Atomen gibt es sowohl Co- als auch Cu-Adatome auf der Oberfläche. DFT-Rechnungen zeigen, daß die substitutionellen Co-Atome als *Nukleationszentren* sowohl für Co- als auch für Cu-Adatome wirken, wobei der Effekt deutlich stärker für Co ist.

Des Weiteren wurde die Adatomdiffusion von beiden Atomsorten (Co und Cu) auf der Terrasse und entlang von Stufen auf der Cu(001)-Oberfläche untersucht. Für Cu beträgt die Diffusionsbarriere durch Hüpfen zwischen Adsorptionsplätzen über einen Brückenplatz 0.49 eV. Dieses Ergebnis steht in guter Übereinstimmung mit früheren DFT-Rechnungen [111] und experimentellen Werten. Die Energiebarriere für den atomaren Austausch ist zweimal höher. Spinpolarisierte Co-Adatome haben eine niedrigere Mobilität auf der Oberfläche: Die Barriere für Hüpfen ist 0.61 eV, während die Barriere für Austausch 1.0 eV ist. Die Spinpolarisation reduziert deutlich die Höhe der Barriere für Prozesse, in denen sich die Koordinationszahl des Co-Atoms zwischen Anfangs- und Übergangszustand stark ändert. Zum Beispiel verringert sich die Barriere für Hüpfdiffusion von 0.92 eV (nichtmagnetisch) auf 0.61 eV (spinpolarisiert). Die Diffusionsbarrieren entlang der [110]-Stufe auf der Cu(001)-Oberfläche sind niedriger als auf der Terrasse: für Cu bzw. Co betragen sie 0.40 eV und 0.55 eV. Dieses Ergebnis kann mit der kleineren Änderung der Koordinationszahl zwischen Anfangs- und Übergangszustand entlang der Stufe von fünf auf vier erklärt werden, während sich bei der Terrassendiffusion die Koordinationszahl von vier auf zwei ändert.

Im Rahmen dieser Arbeit wurde ein *ab initio* kinetisches Monte-Carlo-Programm für das heteroepitaktische Wachstum implementiert. Die Simulationen wurden auf einem fcc-Gitter durchgeführt, was erlaubt, Austauschprozesse (Einbau eines Co Atoms in die Substratschicht und die Erzeugung eines Cu-Adatoms auf der Oberfläche) und das "Pinning" an substitutionellem Co korrekt zu beschreiben. Die Raten für die mikroskopischen Prozesse wurden aus den DFT-GGA-Barrieren bestimmt. Wechselwirkungen mit anderen Adatomen auf der Oberfläche wurden in einem Koordinationszahlmodell beschrieben, das die unterschiedliche Stärke der Bindungen zwischen verschiedenen chemischen Spezies berücksichtigt. Die Oberflächenmorphologie und das Skalierungsverhalten der Inseldichte als Funktion der Temperatur für die Homoepitaxie (0.2 ML Cu auf Cu(001)) und Heteroepitaxie (0.2 ML Co auf Cu(001)) wurden verglichen.

Im homoepitaktischen Fall ist einfaches Hüpfen der dominierende Diffusionsmechanismus, während Austauschprozesse keine bedeutende Rolle für den un-

tersuchten Temperaturbereich spielen. Bei Raumtemperatur entstehen rechteckige Inseln, deren Kanten entlang der $[110]$ - und $[1\bar{1}0]$ -Richtung verlaufen.

Für das heteroepitaktische Wachstum von Co auf Cu(001) wurden zwei Wachstumsbereiche identifiziert:

- Für $T \leq 350$ K findet der Materialtransport hauptsächlich durch Hüpfen statt. Es entstehen kompakte Inseln mit Kanten entlang der $[110]$ - und $[1\bar{1}0]$ -Richtung. In diesem Bereich ähnelt das heteroepitaktische Wachstum dem homoepitaktischen Fall, wobei die Adatommobilität niedriger ist. Gelegentlich tauschen Co-Atome mit Substratatomen aus, wobei die letzteren in Inseln der ersten Lage eingebaut werden.
- Die Aktivierung des Austauschprozesses führt zu einer dramatischen Veränderung der Oberflächenmorphologie. Bei $T = 410$ K wird ein wesentlicher Teil der Co-Atome in die Substratlage eingebaut. Das Zusammenspiel zwischen der hohen Diffusionsrate der Cu-Adatome, die durch die Austauschprozesse auf der Oberfläche erzeugt werden, und der verstärkten Nukleation an substitutionell eingebauten Co-Atomen führt zu einem *bimodalen* Wachstumsmodus. Charakteristisch für diesen Wachstumsmodus sind große Co-dekorierte Cu-Inseln sowie eine hohe Dichte an kleineren Co-Inseln.

In der Homoepitaxie ist ein monotoner Abfall der Inseldichte mit wachsender Temperatur typisch. Im heteroepitaktischen Fall finden wir starke Abweichungen von den Vorhersagen der allgemein verwendeten Nukleationstheorie: Für Co auf Cu(001) weist die Inseldichte als Funktion der Temperatur ein Minimum um 350 K auf und nimmt für höhere Temperaturen wieder zu. Dieses Minimum kann direkt mit der Aktivierung des Austauschprozesses korreliert werden.

Die Ergebnisse aus den *ab initio* KMC-Simulationen untermauern experimentelle Beobachtungen [13, 17] und liefern eine Erklärung für die wesentlichen Mechanismen während der Anfangsphase des Wachstums des Systems. Darüber hinaus lassen sich die Erkenntnisse auf eine breitere Klasse von Materialien übertragen, z.B. auf das Wachstum von anderen *3d*-Metallen auf einem Edelmetallsubstrat. Wie experimentelle Ergebnisse zeigen, erwartet man in der Tat ein ähnliches Verhalten für Fe/Cu(001) [39], Fe/Au(001) [131] und Ni/Cu(001) [41].

Aufgrund des hohen numerischen Aufwands konnten im Rahmen dieser Arbeit nicht alle relevanten mikroskopischen Prozesse untersucht werden. Trotzdem konnte ein fundamentales Verständnis sowohl für die Strukturen, die im thermodynamischen Gleichgewicht entstehen, als auch für die grundlegenden Adsorptions- und Diffusionsmechanismen entwickelt werden.

Als Ausblick seien einige Vorschläge für weitere Untersuchungen aufgeführt. Ein wichtiger Punkt wäre die Verbesserung der Beschreibung der Adatom-Adatom-Wechselwirkung in der KMC-Simulation über das Koordinationszahlmodell hinaus basierend auf zusätzlichen DFT-Rechnungen. Weitere Diffusionsbarrieren, z.B. für die Diffusion eines Co-Adatoms über die Stufenkante einer Co- oder Cu-Insel könnte zum Verständnis der mikroskopischen Ursachen des Doppellagenwachstums beitragen. Wünschenswert wäre auch die Erweiterung des KMC-Programms auf die Beschreibung des Multilagenwachstums. Im Hinblick darauf, wie die magnetische Fernordnung und magnetische Domänen während des Filmwachstums entstehen, wäre es interessant, die Oberflächenmorphologie, die wir aus der *ab initio* KMC-Simulation erhalten, mit einer Beschreibung der magnetischen Kopplung zwischen den Co-Inseln z.B. in einem KMC-Modell [160] zu kombinieren.